Piezoelectric power transducers and its interfacing circuitry on energy harvesting and structural damping applications

Yu-Yin Chen

ENSC-(n° d'ordre)

THESE DE DOCTORAT
DE L'ECOLE NORMALE SUPERIEURE DE CACHAN

Présentée par

Monsieur Yu-Yin Chen

pour obtenir le grade de

DOCTEUR DE L'ECOLE NORMALE SUPERIEURE DE CACHAN

Domaine :
ELECTRONIQUE –ELECTROTECHNIQUE-AUTOMATIQUE

Sujet de la thèse :

Piezoelectric power transducers and its' interfacing circuitry on energy harvesting and structural damping applications

Thèse présentée et soutenue à Taipei le 28 janvier 2013 devant le jury composé de :

Wei-Hsin Liao	Professeur-CUHK, Hong Kong	Rapporteur
Yves Bernard	Professeur à l'université Paris Sud	Rapporteur
Chern-Lin CHEN	Professeur-NTU, Taiwan	Examinateur
Yi-Chung Shu	Professeur-NTU, Taiwan	Examinateur
Faa-Jeng Lin	Professeur-NCU, Taiwan	Examinateur
Ming-Whei Feng	Vice President and General Director-III, Taiwan	Examinateur
Chih-yi Lin	Senior Manager-DELTA, Taiwan	Examinateur
Chih-Kung LEE	Professeur-NTU, Taiwan	Directeur de thèse
Wen-Jong WU	Professeur-NTU, Taiwan	Co-directeur
Dejan VASIC	Maître de conférences HDR U. Cergy-Pontoise	Directeur de thèse
François COSTA	Professeur-ENS Cachan, France	Co-directeur

Laboratoire Système et Application des Technologies de l'Information et de l'Energie
ENS CACHAN/CNRS/UMR 8029
61, avenue du Président Wilson, 94235 CACHAN CEDEX (France)

國立臺灣大學工學院應用力學研究所

博士論文

Graduate Institute of Applied Mechanics
College of Engineering
National Taiwan University
Doctoral Dissertation

壓電功率轉換器及介面電路在能量擷取及結構減震上的應用

Piezoelectric power transducers and its' interfacing circuitry on energy harvesting and structural damping applications

陳昱因

Yu-Yin Chen

指導教授：李世光 博士、吳文中 博士

François Costa 博士、Dejan Vasic 博士

Advisor: Chih-Kung Lee, Ph.D., Wen-Jong Wu, Ph.D.

François Costa, Ph.D., Dejan Vasic, Ph.D.

中華民國 101 年 10 月

Oct, 2012

中文摘要

現今，能源成為了相當重要的議題，從環境當中獲取能源更是受到高度重視。此論文主軸圍繞在透過各種設計來改進壓電能量擷取裝置，希望可與低耗能裝置與無線監測網路結合，來延長裝置電池壽命與直接提供能量為最終目標。機械結構具有高品質因子，當壓電能量擷取裝置操作在遠離共振頻時，輸出功率會快速下降，本論文提出可調變共振頻率的技術，成功的將共振頻率的頻寬延展，獲取更多的能量，此技術也成功的與無線監測網路結合，發射出無線訊號。為了將可用頻寬延展，本論文提出結合非線性雙穩態懸臂樑結構與切換式介面電路的架構，透過永久磁鐵的設計，使懸臂樑成為非線性系統，成功提升在非共振頻時的輸出功率，透過零速度偵測的技術，使切換式電路成功的使用在非線性振動系統當中，由工作週期的討論顯示出兩種技術結合的成果。在低耦合系統中，同步切換為相當成功之介面電路，不同於以往峰值偵測的方式，本論文提出零速度偵測與三片壓電分流的架構，成功完成自供電同步切換壓電能量擷取系統。當系統為非低耦合時，同步切換技術可應用在系統減震上，最大優點為犧牲少部分減震能力完成自供電減震系統，自供電減震系統的限制與成果透過理論分析、時域與頻率域的結果被成功驗證，整體系統如同回授控制般，當結構振動高於限制時，自供電減震系統將會啟動，並成功的抑制結構振動。

關鍵字： 壓電能量擷取，自供電，零切換偵測，同步切換，結構減震

Abstract

Nowadays with the world oil price soaring, the energy issue is becoming a significant topic and the possibility of harvesting ambient energy receiving much attention. In this dissertation, the main topic surrounds improving the piezoelectric energy harvesting device in several aspects and the final objective is to integrate it with low power consumption device, for example a wireless sensor network (WSN) node to extend the battery lifetime and further supply the energy to device directly. Based on the high mechanical quality factor of the structure, the output power of the piezoelectric energy harvesting device will decrease rapidly when the exciting frequency is out of the resonant frequency range. The tunable resonant frequency technique is proposed to broaden the resonant frequency range and increase the output power effectively. Then this technique is successfully combined with a WSN module to transmit the RF signal. To broaden resonant frequency another method is proposed, based on a bistable vibrating cantilever beam and a switching-type interface circuit (SSHI). It's a new and interesting concept to combine these two techniques. The magnets are used to make mechanical behavior non-linear and increase the output power at non-resonance. The SSHI technique through zero-velocity detection can work well when system is driven in non-linear system. The experimental and simulation results through work-cycles discussion show good performance of combining these two techniques.

In the interface circuit design, synchronized switching harvesting on an inductor (SSHI) have been verified a successful technique to increase output power in low-coupling system. In order to make use of the SSHI technique in the real application, the velocity control self-powered SSHI (V-SSHI) system is proposed. Unlike the conventional peak detector technique, the zero-velocity detection is used to make the switching time more accurate. The energy flow is separated into three paths to construct the V-SSHI and the experimental results show good performance.

When the system is not low-coupled, the SSHI technique will damp vibration. This technique is called SSDI (synchronized switching damping on an inductor). Based on the self-powered technique and zero-velocity detection used in the V-SSHI, these techniques are further applied in structural damping to construct a self-powered SSDI (SP-SSDI). The major advantage is that it is only necessary to sacrifice a small amount of damping performance to make the system fully self-powered. The theoretical analysis and experiment results of time domain comparison and frequency response testing show the limit and performance of the SP-SSDI technique. The SP-SSDI system is a like a feedback loop system and when the displacement is over the limit the SP-SSDI will effectively damp the vibration.

Keywords: piezoelectric energy harvesting, self-powered, zero-velocity detection, synchronized switching, structural damping.

Résumé

Aujourd'hui, avec l'envolée mondiale du prix du pétrole, la question énergétique est devenue un sujet d'importance et la possibilité d'exploiter l'énergie ambiante connait un regain d'attention. Ainsi dans cette thèse, nous nous intéressons aux dispositifs de récupération d'énergie piézoélectrique de vibration dont l'objectif final est de réaliser un réseau de capteurs sans fil (WSN) autonome de faible consommation d'énergie. L'idée est dans un premier temps de prolonger la durée de vie de la batterie, puis dans un second temps de rendre le capteur totalement autonome d'un point de vu énergétique. Les dispositifs actuels étant basés sur la vibration d'une poutre (résonateur mécanique), ils ne sont efficaces qu'à la résonance, avec une faible bande-passante. Ainsi dans ce travail, nous avons tout d'abord proposé une technique de décalage de la fréquence de résonance à l'aide de capacités commutées, cette technique réalise un ajustement de la fréquence de résonance en fonction de la fréquence de la source d'excitation et ainsi permet une augmentation de la puissance de sortie. Cette technique a été implémentée avec succès sur un module de capteur WSN avec transmission d'un signal RF. Toujours dans l'objectif d'agrandir la bande-passante, un résonateur hybride (piézoélectrique/magnétique) bistable associé à une interface électrique (SSHI) a été proposé. Ce nouveau et intéressant concept de combiner le résonateur hybride avec une interface à commutation de la tension piézoélectrique a montré, à l'aide de résultats

expérimentaux et de simulation, que la puissance est augmentée sur une large bande passante. De plus, afin de rendre le système totalement autonome et de commander les interrupteurs de l'interface électrique aux instants optimaux, une technique de détection du passage par zéro de la vitesse de vibration a été proposée. Les résultats montrent de bonnes performances de cette méthode sur toutes les interfaces et résonateurs. Contrairement à la méthode classique de détection de la tension crête, la détection du passage par zéro de la vitesse est plus précise.

La récupération d'énergie piézoélectrique engendrant un amortissement de la source vibrante, il est possible d'utiliser les mêmes interfaces électriques pour réaliser l'amortissement semi-passif de vibrations de structures mécaniques. Il s'agit d'extraire le maximum d'énergie de la structure en vibration à l'aide de l'élément piézoélectrique. Ainsi, afin de rendre les interfaces électriques pour l'amortissement (SSHD) totalement autonomes, nous avons proposé d'associer la récupération d'énergie piézoélectrique à l'amortissement de structure. L'avantage majeur est qu'il est seulement nécessaire de sacrifier légèrement les performances de l'amortissement pour rendre le système totalement autonome. Les performances ainsi que les limites de cette technique ont été analysées.

Mots-clés : récupération d'énergie piézoélectrique, interface électrique, SSHI, commutation synchronisée, auto-alimentation, amortissement de structure.

CONTENTS

List of the Figures

List of the Tables

Chapter 1. Introduction

1.1 Backgrounds and Motivations

During recent decades, world oil price soars and the energy issue becomes the most important and attractive issue in the world. Many researches and projects concentrate on finding alternative energy source. The alternative energy source includes large scale power source as solar and wind energy [5-12] used to replace the conventional energy source and small scale power source as vibration, acoustic noise [1] and temperature gradient [2] used to extend the battery lifetime of the electronic device. Methods adopted to make portable devices or sensors retrieve energy from the environment are so called “Power harvesting” or “Energy harvesting.” Because recently years the size of portable devices, such as mobile phone, mp3 players, flashlight and sensor nodes become more and more smaller, and the great advancement in power consumption of portable devices [3, 4], it becomes possible to harvest energy from ambient and directly provide the portable devices to use or elongate the battery lifetime. The energy harvesting device can fully supply the power required by the sensor node in idle mode, and may have extra power to charge the battery when the sensor is in idle. Thermal gradient [5, 6], solar [7, 8], wind [9], humans activities [10-12], barometric fluctuations, ocean wave [13], etc. are the good alternative energy source and there are lots of

materials can convert these ambient energy into the electrical energy. Some of the most common materials being the typical energy generators and retrieving the ambient energy from the devices site are photovoltaic materials, piezoelectric material and electromagnetic materials. Photovoltaic cells can convert ambient light energy [14] such as sunlight to electrical energy and these devices typically are tended to located at the place exposed to sufficient light such as roof, windows of the buildings, roadway signs, sailboats, and other marine locations. Energy from mechanical vibration in some situations may also be taken effectively by using two kinds of mechanisms. They are 1) piezoelectricity that converts mechanical vibrations to electric energies [11, 15-17] and 2) electromagnetism that generates electricity by moving magnetic fields [18-20]. Wireless sensor networks (WSN) can be used to monitor the health of the structures, environment, wild animals, tire pressure of running car, etc. In the most of WSN applications, the device is far from the power line or the device needs be embedded into the structure to monitor. So, it is hard to use power line to transmit energy to device and battery is the only conventional solution. However, there are lots of disadvantages with using batteries. The major problem is the life time, a WSN node can only be operated using 3V battery for 1~2 years. The batteries cannot be a permanent energy supply for WSN. For embedded applications, it is hard and even impossible to replace batteries

very often. A WSN with self-powered supply system can be operated for longer life time, even can be operated without replacing the battery. Harvesting the ambient energy close to the sensor nodes of a WSN node is the most likely and suitable solution to extend the life of WSN [21-25]. The efforts of most research are working on harvesting energy from ambient mechanical vibrations with piezoelectric materials because of its high energy density per unit volume, high electormechanical coupling, and no external voltage source requirement. These research also try to combine power harvesting devices with wireless sensor network [21, 22, 26]. Roundy presented that the energy density of the piezoelectric material is around 35.4 (mJ/cm^3) and is higher than electromagnetic material (24.8 mJ/cm^3) and electrostatic (4 mJ/cm^3) [22]. And comparing with the different energy source, the power density of the piezoelectric material is around 250 (uW/cm3) and is also higher than other materials when exciting from vibration [26]. Paradiso and Feldmeier [27] in 2001 design a self-powered wireless RF transmission device. From their design, when push the piezoelectric button, the devices can transmit a digital ID code wirelessly without any battery or any other power sources. However, this design needs someone to push the piezoelectric button to generate the energy for transmitting to RF signal, it cannot work automatically. Since 2002, numerous studies have been published on the topic of energy harvesting. Tang et

al. (2010) and Khaligh et al. (2010) have made a long synthesis and developed a state of the art for vibration piezoelectric energy harvesting. This demonstrates the interest of researchers for this topic.

Figure 1-1 shows the WTI (West Texas Intermediate) crude oil price (US dollars per barrel) from 1997 to 2012 and the crude oil price soars around from 2000. Figure 1-2 shows the paper record count of energy harvesting including all kinds of energy source and using different materials and Figure 1-3 shows only the paper record count of piezoelectric energy harvesting. Comparing with Figure 1-1, Figure 1-2 and Figure 1-3, the time of the crude oil pricing soaring agrees with the time of energy harvesting technique growing vigorously. Before 2000, the paper count of energy harvesting almost keeps the same. After 2000, the paper counts of energy harvesting have bloomed around 5 times, especially using piezoelectric materials in energy harvesting. In 2000, there is an only one energy harvesting paper using piezoelectric material, however in 2011, there are 253 papers. As Figure 1-3 shown, using piezoelectric material to be the energy harvesting device is highly focused over the past 10 years and from the Figure 1-4, using the piezoelectric materials to be the energy harvesting device is around 8.74 % of the total energy harvesting papers.

Based on this information, in this dissertation piezoelectric materials are chosen to

be the interfacing material of the energy harvester to transfer the ambient vibration energy into electrical energy to be used.

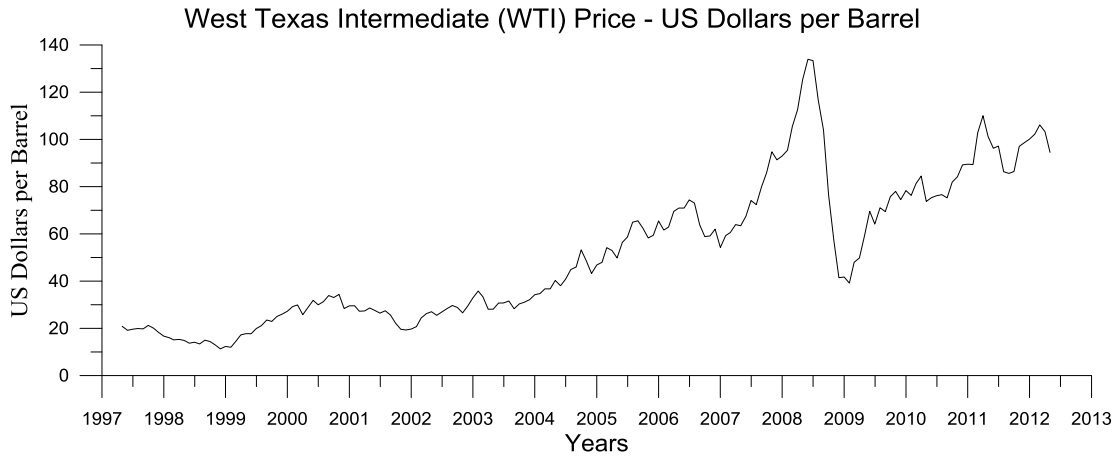

Figure 1-1. WTI crude oil price chart

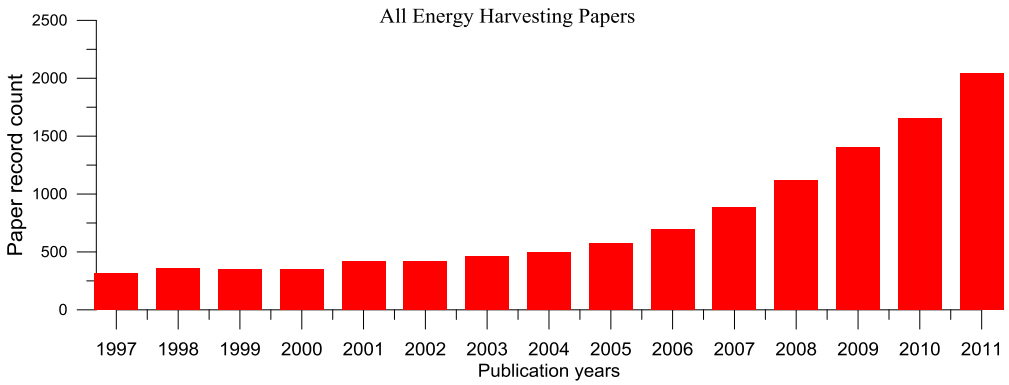

Figure 1-2. All energy harvesting paper statistics

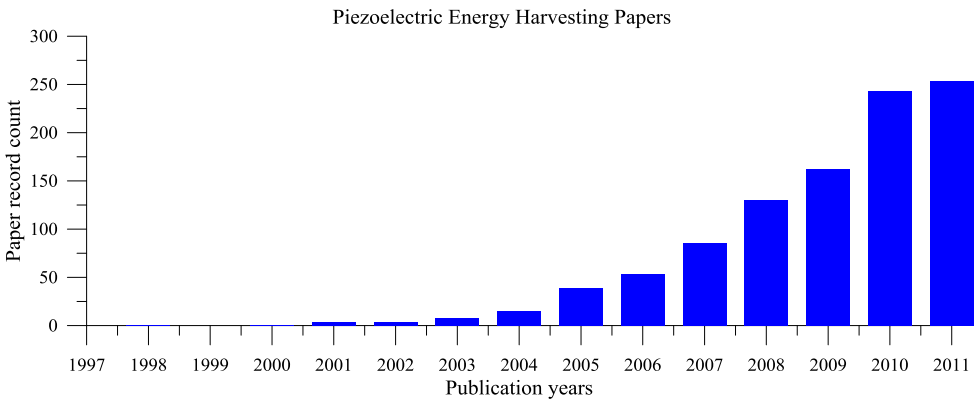

Figure 1-3. Piezoelectric energy harvesting paper statistics

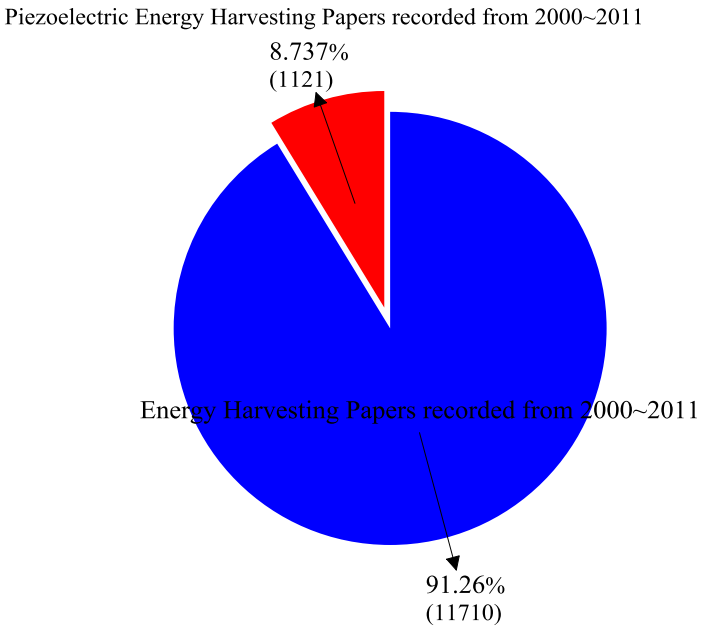

Figure 1-4. Pie chart of Energy Harvesting papers

1.2 Literatures review

The typical piezoelectric energy harvesting device can be divided into two parts as Figure 1-5. First part is the mechanical part composed of piezoelectric material and

host structure and second part is the electrical part composed of the interface circuit and storage device. The piezoelectric material and host structure are the major part to decide the electrical energy transformed from the vibration mechanical energy. The interface circuit and storage device decide the efficiency of the energy transformed from the piezoelectric material into storage such as capacitor. According to the different storage device, choosing the proper interface circuit can effectively increase the efficiency. The simplest storage device is composed of the regular capacitor and a equivalent resistor load. Based on the different parts design of piezoelectric energy harvesting device and applications, the literatures review is divided into several sub-sections as following.

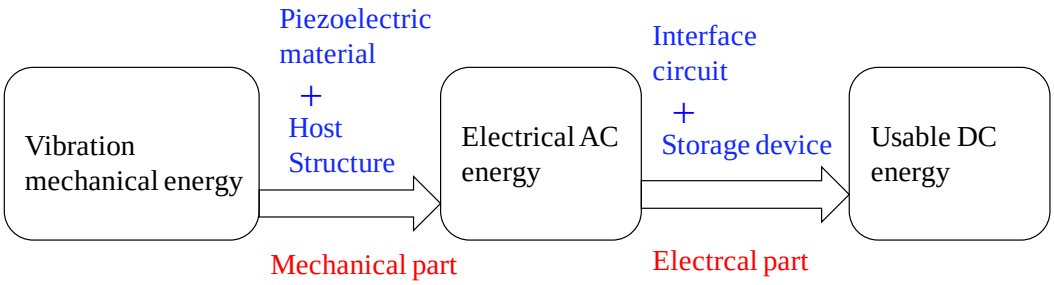

Figure 1-5. Schematic of the typical piezoelectric energy harvesting device.

1.2.1 Mechanical part: Design of the piezoelectric material and host structure

Many researchers made efforts in developing energy harvesting devices from vibrations using cantilever beam based energy harvester due to its tremendous

application potential [28-36]. The typical cantilever beam is shown as Figure 1-6. Instead of talking about one-layer piezoelectric cantilever beam energy harvester, Roundy and Wriht in 2004 [22] develop, validate and optimal the basic analytical model for a two-layers bending element type (bimorph type) piezoelectric vibration based energy harvester as Figure 1-7 and then they design a power generation circuit to drive wireless sensor networks.

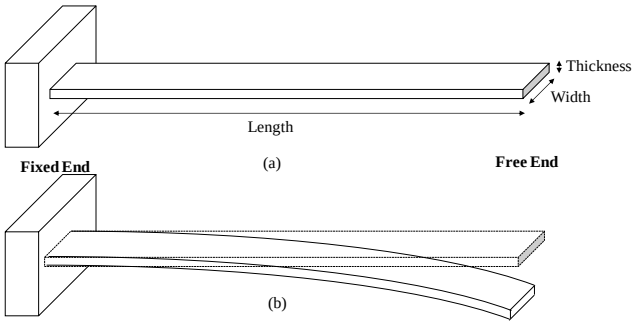

Figure 1-6. (a) Typical cantilever beam (b) Cantilever beam deflection at first mode

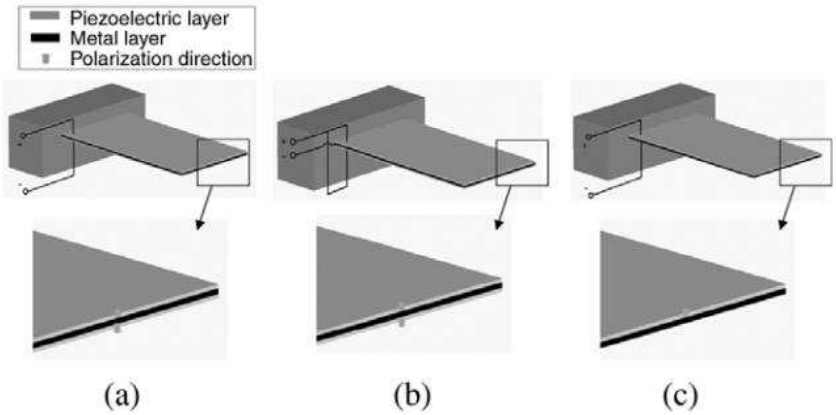

Figure 1-7. (a)Bimorph type - A series triple layer type (b)Bimorph - A parallel triple layer (c)Uunimorph type. [37]

In addition to talk about traditional 1-D cantilever beam design, such as Kim et al. [38, 39], Ericka et al. [40] use the 2-D piezoelectric membrane to harvest energy from pulsing vibration sources and establish the 2-D piezoelectric plate model as Figure 1-8. The PZT plate is bounded on the aluminum plate to become a 2-D circular piezoelectric energy harvesting device. From their results, the energy harvesting can be enhanced by patterned polarization of the piezoelectric material.

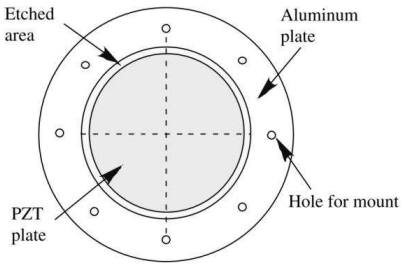

Figure 1-8. Top view of circular piezoelectric energy harvesting device. [39]

All researches about the different structure design whatever 1-D, 2-D, 1-layer or 2 layers are trying to enhance the power output of the piezoelectric energy harvester. The power output level of energy harvesting devices is very important, because if the power output is not enough to do real application, all innovative design are useless. However, the power output is not the only important issue for energy harvesting design; the power

transformation efficiency is the other important issue.

Goldfarb and Jones [41] and Umeda et al. [28, 42] talk about what the parameters of the piezoelectric materials effect the power efficiency of the power harvesting devices. The results show that high mechanical quality factor (Q_m), high electromechanical coupling coefficient (k^2), and low dielectric loss (tan δ) will increase the efficiency of the piezoelectric energy harvester. Richards et al. [43] develop an exact formula to predicts the power conversion efficiency of the piezoelectric energy harvester and establish the relation between the electromechanical coupling coefficient, quality factor and power generation efficiency for piezoelectric oscillators. From the results, the magnitudes of Q and k^2 are coupled together; it cannot be optimized and designed separately. The energy conversion efficiency is trade-off between Q and k^2.

Because the most researches is focusing on different part of energy harvesting piezoelectric based generator, and the energy output is not normalized quantity, it is hard to compare the different power harvesting devices. Roundy [31] in 2005 provide a general theory that can be applied to compare different power harvesting devices vibration-based generator and he present a general theory that can also be applied to electromagnetic, piezoelectric, magnetostrictive, and electrostatic transducer technologies. In addition to the input parameters of the vibrations, the general form

"effectiveness" is composed of system coupling coefficient, the quality factor of the device, the mass density of the generator and the degree to which the electrical load maximizes power transmission.

1.2.2 Electrical part: Design of the interface circuit and storage part

The research of the above sub-section are studying about the material and host structure part of the energy harvesting devices, and more researches are focusing on electrical circuit design. If the electrical energy is stored in a capacitor or a battery, an energy recovery system is obtained. Through the interfacing circuit design and discussion, the efficiency of energy storage of piezoelectric energy harvesting device can be increased. Lesieutre et al. [44] indicate that when the piezoelectric materials connect to the electrical load, the electrical load will absorb the energy from the piezoelectric and it will increase the damping factor for the piezoelectric system. The same condition occurs in the power harvesting application, and the storage part including DC-DC converter and the capacitor or battery is the electrical load to the piezoelectric cantilever beam and the piezoelectric energy harvesting device with a DC-DC converter is shown in Figure 1-9 [21]. Comparing with measuring the spectrum in open or in short circuit condition, the whole system will not be ideal from the

damping effect of the electric load. The electric energy issued from a piezoelectric energy harvesting device is alternating voltage (AC) across its electrodes, so the simplest interfacing circuit to use is standard DC approach (full bridge diode rectifier). From the studies [34], the efficiency of the standard DC approach is not designed optimally. There are lots of studies devoted the efforts to design and optimizing the interfacing circuits to improve the efficiency and maximizing the output power. Ottman et al. [21, 29] through the concept of impedance matching provide the adaptive control technique and design an electric circuit using ac-dc rectifier and dc-dc step-down converter to increase the harvested power around 325 %. According to Ottman's results, maximum energy harvesting can be obtained by optimal duty cycle accurately determined.

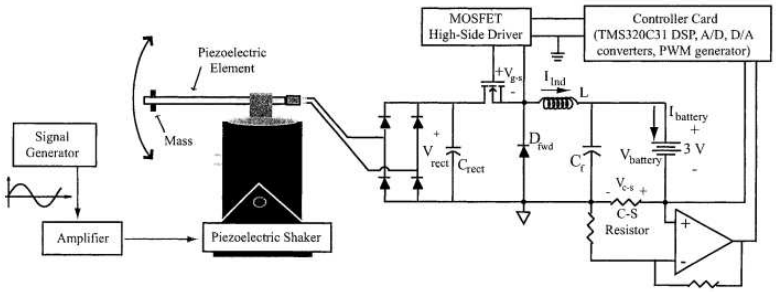

Figure 1-9. Experiment circuit setup of energy harvesting device with DC-DC converter [21].

The piezoelectric elements convert the vibration energy of the host structure into

electrical energy, and then the generated electrical energy is stored in a capacitor or a battery. Since the piezoelectric element has larger intrinsic capacitance, an impedance matching circuit is required to maximize the generated power. Although the matching electric circuit can be optimized by a passive network [32], it cannot be adaptive to the variations of environmental vibrations. The exciting frequency of environmental vibrations cannot be always at one constant value and fits to the natural frequency of the energy harvesting device. To overcome this drawback, a switching circuit [45] was proposed and popularly used in recent years. In the switching circuits, the switches are operated synchronously with the vibration of the host structure in order to optimize the power flow.

Several synchronized switching circuit topologies and corresponding switching laws were proposed. The most efficient switching techniques can be classified into two groups according to the placement between the full-wave bridge rectifier and the switches. The first group of the switching circuits places the switches before the full-wave bride rectifier, such as parallel-SSHI (Synchronized Switching Harvesting on an Inductor) as Figure 1-10(a) and series-SSHI [32, 33] as Figure 1-10(b); the second group places the switches after the full-wave bridge rectifier, such as SECE technique as Figure 1-10(c) [32]. The optimal load of the series and parallel SSHI techniques are

different. [32, 33, 36, 46-48]. The optimal load value of parallel-SSHI (around mega ohms) is higher than that of series-SSHI (around hundred ohms) [34]. In SECE technique, the power output is not as high as the SSHI technique, but the power output is independent of the load. In these techniques, the switching circuit only turns "ON" at the extreme value of the displacement or at the zero crossing of velocity to shift the phase of the voltage across the piezoelectric element. These techniques are used because the piezoelectric-generator is weakly coupled to the host structure, i.e. only a small amount of mechanical energy is taken from the structure and converted in electricity. The electrical behavior of the piezoelectric-generator with the SSHI circuit is equivalent to an operation under strong coupling conditions by increasing the output voltage [49].

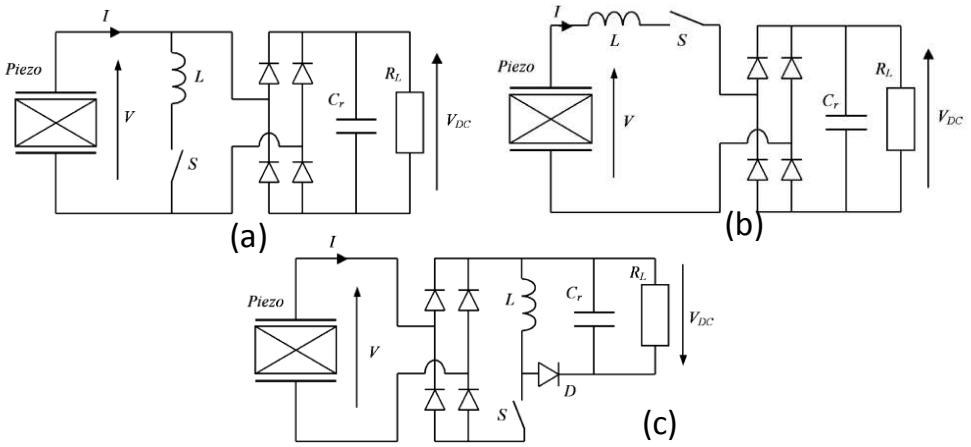

Figure 1-10. (a) Parallel-SSHI interface circuit (b) Series-SSHI interface circuit (c) Synchronized charge extraction interface circuit (SECE) [32].

Except designing the interface circuit to increase the efficiency, it is to be noted that bootstrapped cold start-up was a new concept on power harvesting as it could start the overall circuitry even when the batteries are empty. In addition, minimizing switching loss by controlling oscillator on/off duty cycle low is another major issue being examined The design of the MIT media lab team concentrates on the interface electronics. They used an integrated circuit to handle problems that the electrical signal would come across, which include issues such as how to harvest the primary signal peak with minimal loss and to provide for bootstrapped “cold” start-up [50].

1.2.3 Self-powered energy harvesting system

Successful interface circuit can effectively increase the harvested energy but most of them need the external power source to build up the system. So except focusing on the interface circuit design, there are lots researches to study and make the energy harvesting device self-powered and be combined with different applications. Elvin et.al. [51, 52] and Ng and Liao [37], they give some new applications and innovative design ideas. They use piezoelectric materials not only be a power harvesting device but also be a senor. The sensor system with power harvesting and RF transmitter is shown in Figure 1-11 and the voltage on the charging capacitor is show in Figure 1-12 [51].

According to their researches, they establish a self-powered sensor system and from theoretical and experimental analysis they show how the system works and the performance of the system. When the voltage on the capacitor is over 1.1V and the electric switch (s) will switch on and the self-powered system successfully transmits the RF.

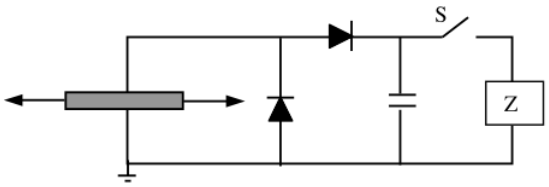

Figure 1-11. Sensor system with power harvester and RF transmitter [51].

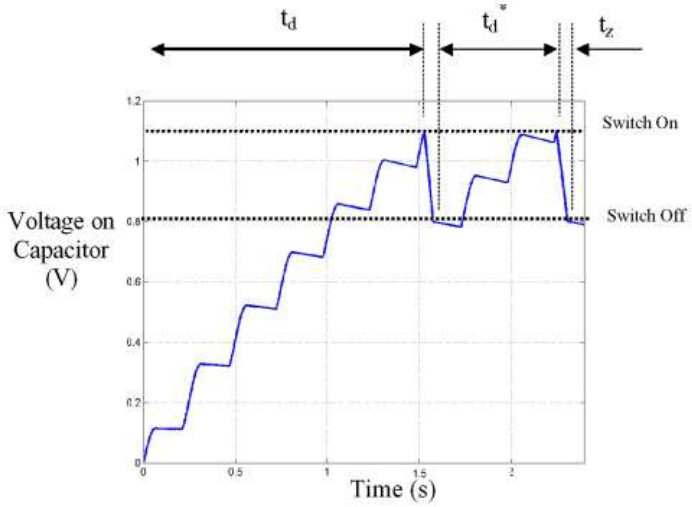

Figure 1-12. The voltage on charging capacitor [51].

The self-powered system proposed by Elvin in 2001 [51] used a simple half-bridge

to regulate the energy. However, the synchronized switching technique is much efficient. So the further complicated technique is to make the synchronized switching technique be the self-powered. Lallart in 2008 proposed a self-powered SSHI switching circuit and the circuit is shown in Figure 1-13 [53]. They build up a basic theoretical analysis and the experiment shows the circuit can be fully self-powered and used in the low voltage range. So it's proper to integrate with the MEMS generator. In the 2012, Liang [54] proposed a modified self-powered SSHI interface circuit as Figure 1-14. This circuit is improved from the Lallart's cirucit and entire system is accurately analyzed about the switching time lag and inversion factor. The conclusion also shows if the SP-SSHI outperform than standard interface circuit the excitation level must be high enough.

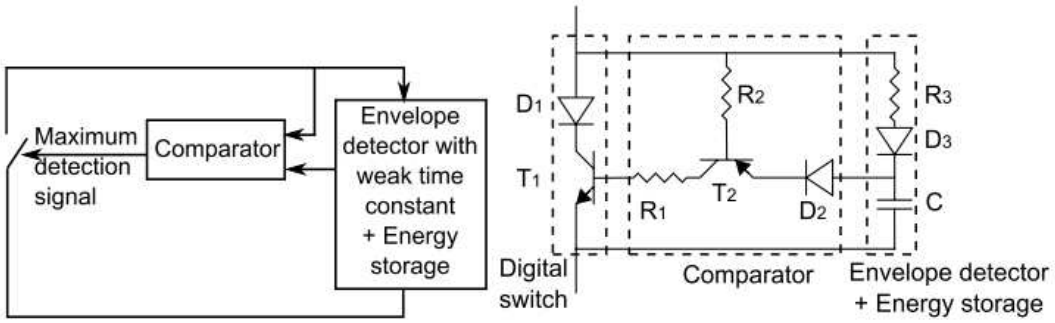

Figure 1-13. Unipolar electronic switch on maxima (a) block diagram (b) implementation [53].

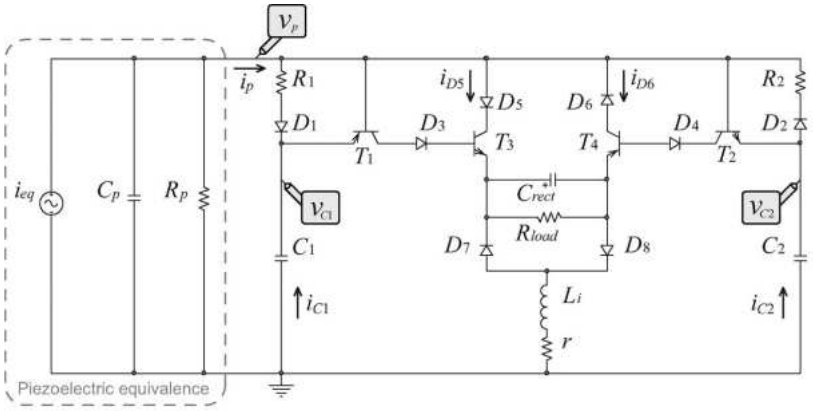

Figure 1-14. Modified self-powered SSHI interface circuit [54].

1.2.4 Nonlinear energy harvesting technique

Although the piezoelectric materials exhibit high power density, the linear piezoelectric energy harvester are efficient only when the mechanical system is excited at the resonance frequency; there is the largest strain, largest vibration displacement and the maximum output power compared to work at non-resonant frequency. However, in practice, the exciting frequency of the ambient vibration source is random and it varies within a frequency range [26]. It is impossible to excite the energy harvester at specific resonance frequency and to keep the system operating on the maximum power point. In the mechanical system, the quality factor is commonly very high. It causes that the harvester has high harvesting power only at single resonance frequency. In order to

increase the power at non-resonant frequency, designing a mechanical system to work in a wide frequency range is necessary. This design concept to enlarge the frequency bandwidth is based on applying external forces. By applying an axial force as the preload force, the resonant frequency of a piezoelectric cantilever beam is successfully tuned as Figure 1-15 [55, 56]. but these methods are active techniques and the mechanical system is still operated within the linear regime. Another method consists to make a non-linear or bistable vibration of a cantilever beam to enlarge the workable bandwidth as Figure 1-16 [57-60]. By using simple fixed magnets, this passive technique make the mechanical system improve the harvesting efficiency within non-resonant regime without any external power.

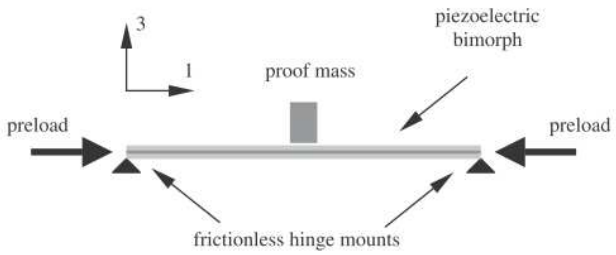

Figure 1-15. The schematic of a simply supported piezoelectric bimorph vibration energy harvester [55].

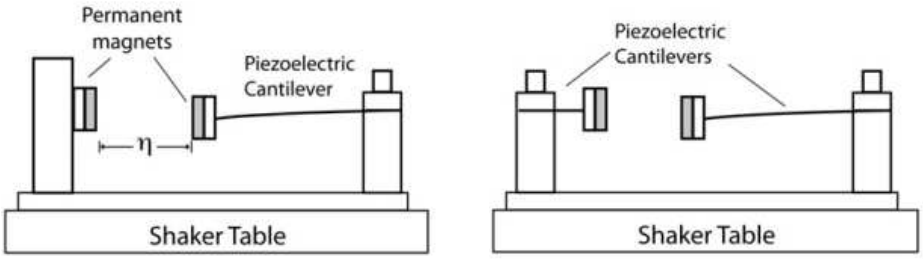

(a) (b)

Figure 1-16. (a) Setup with fixed opposing magnet (b) Setup with opposing magnetic attached to a second cantilever [57].

1.2.5 Piezoelectric energy harvesting device used in real application

When talking about the real case applications, the MIT Media Laboratory is the most famous team using the piezoelectric materials to harvest power from human being activities. The MIT Media Laboratory studied the possibility of adopting power harvesting by embedding piezoelectric devices to insole of walking shoes, which extract electricity from the foot pressure as Figure 1-17 [50, 61]. Both piezoelectric polymer such as PVDF (polyvinylidene fluoride) and piezoelectric ceramics such as PZT (lead, zirconate, titanate) were used as the energy harvesting devices. One of the main challenges lie on how to charge the battery efficiently by using the electricity retrieved. To gain maximum energy usage, the PVDF and PZT devices were designed to fit both the shoe shape and the way of walking. Flexible piezoelectric devices based on PVDF were adopted in the front of the shoes as both compressed and bending forces were

present there. On the other hand, PZT was placed in the back of shoes as the primary forces present there is compression.

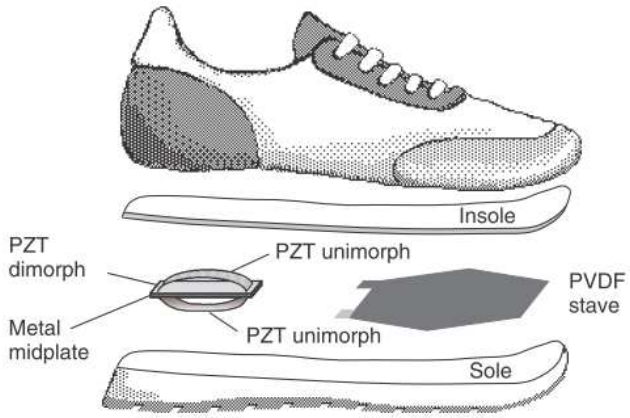

Figure 1-17. Two approaches to unobtrusive 31-mode piezoelectric energy harvesting in shoes: a PVDF stave under the ball of the boot and a PZT dimorph under the heel [50].

A few companies are commercializing power harvesting devices worldwide. For example, Ferro Solutions Energy Harvesters (FSEH) [ref] developed by Ferro is an independent power sources that generate electricity from environment vibrations to power wireless transceivers, sensors, micro-motors and actuators. The FSEH was demonstrated to have the potential to replace batteries in many situations by providing devices with a continuous, nearly endless supply of electricity. To further advance this technology, Ferro is using new magnetic materials to further extract energy from piezoelectric substances, which give off electricity in reaction to mechanical stress.

Nevertheless, they were facing with the problems that their substances were brittle and break easily. To solve this problem, Ferro sandwiched the piezoelectric material between two magnets, which provides them with an opportunity to harvest energy from a changing magnetic field. The prototype developed by Ferro looked like a clear spool just under two inches in height and in diameter. With power output in the range of 0.4 mW when the external vibrations is on the order of 20 milli-Gs in strength, which is barely enough to be felt on the surface by using a bare hand. Stronger vibrations of 100 milli-Gs were found to generate 9.3 mW, which further demonstrate the possibility offered by power harvesting technology.

1.2.6 Piezoelectric material used in structural damping

The basic theory of using piezoelectric material in energy harvesting is the same as in structural damping. All we need are using piezoelectric material to transform the mechanical energy into electrical energy. In the energy harvesting, the electrical energy is stored in a capacitor. However, if the electrical energy is dissipated by Joule effect in a resistance, the vibration of the structure will be significantly reduced and this is called structural passive damping [62]. So most techniques and interface circuits used in the energy harvesting can be used in the structural damping. There are many shunt

techniques based on the design of piezoelectric materials used for damping applications. The simplest one is the passive technique that uses a matched inductor and resistor network to the piezoelectric patch as Figure 1-18 [63, 64]. However, this technique has a major disadvantage. In low frequency applications, the optimal shunt inductor is too large for feasibly implementation. In most cases, the inductance required would be approximately one hundred henrys, which can only be implemented with active circuitry. To implement a shunt inductance with active circuitry, an external power source is needed, and the major advantage of passive damping is lost. The most effective active damping technique is to use active controllers, power amplifiers, and analog or digital processors that generate an out-of-phase signal to control the structural vibration. This technique usually provides better damping performance than passive ones [65, 66]. The advantages of the active damping techniques are good performance and a wider working frequency range, whereas the disadvantage is that the active circuits require external power. The implementation and algorithms for active techniques can be much more complex and the cost is much higher than passive damping techniques.

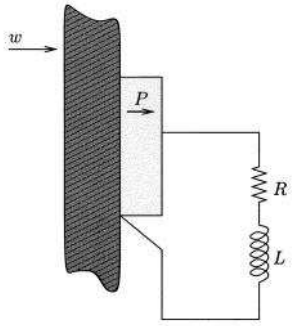

Figure 1-18. Piezoelectric transducer with an RL shunt circuit [64].

Considering the trade-offs in the cost, difficulty of implementation, power consumption required and damping performance, some switch shunting or semi-passive techniques [67-69] have proven to be effective methods. Several switching shunt circuit topologies and corresponding switching laws were proposed. The two most popular switching shunt-damping techniques are SSDI (Synchronized Switch Damping on an Inductor) as Figure 1-19(a) [70] and SSDV (Synchronized Switch Damping on a Voltage source) as Figure 1-19(b) [71-73]. Rcihard et al. first proposed the SSD (Synchronized Switch Damping) technique in 1999 as Figure 1-20 and this technique was further designed and enhanced to be the SSDI and SSDV technique. SSDI technique has attracted more attention because its offers several advantages: it does not require a very large inductor for low frequencies and its robust to the environment changes. Moreover, this technique only needs low-power to operate the switches. Thus,

this technique presents the advantages of being self-powered. The fundamental concept of SSDI technique is the same as the SSHI technique to the use the resonance between the piezoelectric clamped capacitance and a shunt inductance during a short time interval to inverse the piezoelectric voltage.

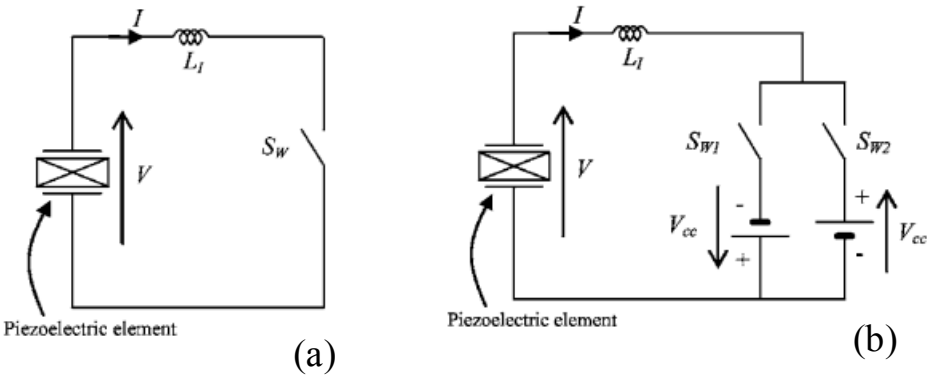

Figure 1-19. (a) SSDI electric circuit (b) SSDV electric circuit [73].

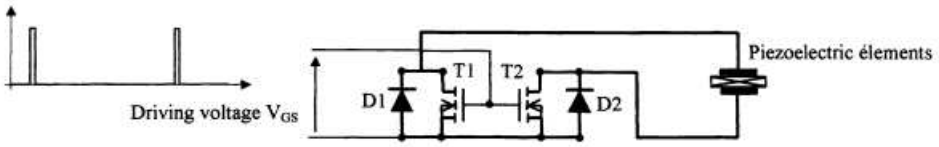

Figure 1-20. SSDS electric circuit [67].

Based on the previous numerous and great research results, in this dissertation, the further designs in interfacing circuit of the piezoelectric energy harvester are proposed.

The synchronized switching technique are proven to be the great effective technique to increase the efficiency of the piezoelectric energy harvester. In order to make this outstanding technique be used in the real application, the further design is needed. Further design in different applications will be discussed in detail in the following sections.

1.3 Framework of the dissertation and Summary

There are 7 chapters in this dissertation. The following are the summary of the each chapter.

Chapter 1 introduces this dissertation.

Chapter 2 proposes the fundamental mechanical modal, equivalent modal and the analysis of the piezoelectric cantilever beam based energy harvesting device. There are several famous and effective synchronized switching techniques which are used in this dissertation will be presented, analyzed, discussed, compared and summarized.

Chapter 3 proposed a tunable resonant frequency cantilever beam type energy harvesting to increase the power output of the piezoelectric energy harvesting device. The tunable resonant frequency technique is based on the characteristic of the piezoelectric material to shift the resonant frequency of the cantilever beam and make

the available bandwidth broaden. The average harvested power output increase almost 30% under chirping and random frequency from 72Hz to 76Hz (resonant frequency is 73.5Hz). From the experimental results, this tunable frequency system can be successfully combined with wireless sensor network to transmit the RF signal.

Chapter 4 proposed a self-powered piezoelectric energy harvesting device using the velocity control synchronized switching technique. In this chapter, the self-powered technique and velocity sensing technique are used to make the popular and effective synchronized switching technique work without any external instruments. The experimental results show better performance and lead to a gain of around 200% compared to the standard DC approach.

Chapter 5 proposed a broad bandwidth and efficient piezoelectric energy harvesting device by using the magnetic force combined with synchronized switching technique. Nonlinear magnetic force is used to broaden the available bandwidth to make piezoelectric energy harvesting device can obtain more energy on the off-resonant frequency. Combining the magnetic force with the traditional synchronized switching technique is the innovative and effective method to make a high efficient and wide-band piezoelectric energy harvesting device. The frequency response and analysis of the work-cycle show the performance of the results of combing these two techniques to

build the piezoelectric energy harvesting device.

Chapter 6 propose a self-powered semi-passive piezoelectric structural damping technique based on zero-voltage crossing detection. The drawback of the traditional semi-passive damping technique is that the system needs external instrument. In this chapter, the self-powered technique is used to make semi-passive technique damping work like passive technique without any external instruments and by using zero-voltage crossing detection to reduce the traditional shortage of the synchronized switching technique. Compared to the case in which all of the piezoelectric patches are used for structural damping and driven by an external function generator and a power supply, the efficiency of the proposed self-powered damping system is approximately 86%. Compared to the ideal switching case in which the same size of piezoelectric patch is used for SSDI damping and is driven by an external function generator and power supply, the efficiency of the proposed self-powered system is approximately 95%. The major advantage of the proposed technique is that it is only necessary to sacrifice a small amount of damping performance to make the system fully self-powered.

Chapter 7 summarizes the entire dissertation and gives a conclusion. The conclusion will point out the main innovation and contribution of this dissertation. Finally, the future work will be presented in this chapter.

Chapter 2 Review of the electric interfaces for energy harvesting and damping

This chapter presents a review of the literature about electric interface called SSHI (Synchronized Switching Harvesting on an Inductor) for the energy harvesting and structural damping applications. The basic governing equation, equivalent circuit model, waveform, optimal load and maxima output power are analyzed and discussed. A comparison of different interface trough work-cycle analyze will be done.

Since the efficiency of the electromechanical conversion of piezoelectric transducer depends of the electrical load, an electrical circuit must be introduced to optimize the conversion and to adapt the piezoelectric voltage to the storage device. The interface circuit plays a very important role to regulate the alternating current into direct current and decides the efficiency of the energy harvester [34]. In order to easily analyze and combine with the interfacing circuit, the piezoelectric beam will be study with the equivalent circuit representation. Starting from the equations of motion and the constitutive equations of the piezoelectric material, the model of the cantilever beam type piezoelectric energy harvesting device will be established. Several interface circuits and corresponding waveforms of piezoelectric terminal voltage and output power will be study. Moreover a work-cycle representation to compare the

performances of the interface circuits will be investigated.

2.1 Basic theory of piezoelectric materials

According to IEEE standard 176-1987 [74], constitutive law of piezoelectric materials can be expressed as equation (2.1). The constitutive law presents the relations between strain S, stress T, electric displacement D and electric field E of the materials. Table 2-1 shows the representations. According to the constitutive law, the behavior of the piezoelectric materials can be obtained and through the further analyzing the mechanical modal can be easily established.

$$\begin{bmatrix} T_p \\ D_i \end{bmatrix} = \begin{bmatrix} c_{pq}^{E} & -e_{kp} \\ e_{ip} & \varepsilon_{ik}^{S} \end{bmatrix} \begin{bmatrix} S_q \\ E_k \end{bmatrix} \tag{2.1}$$

Where

Table 2-1. Representations of constitutive law of piezoelectric materials

T_p	stress
S_q	strain
D_i	electric displacement
E_k	electric field respectively
c	elastic constant
ε	permittivity constant

e	piezoelectric constant

superscripts E and S represent constant

superscripts i,k=1~3, p,q=1~6 represent the coordinates index which is shown in Figure 2-1.

Considering the piezoelectric patches bound on a cantilever beam can be regarded as a simple energy harvesting device. The dimensions of piezoelectric patches, schematic of the beam and coordinate directions are shown in Figure 2-1. When the cantilever beam vibrates, for example as Figure 2-2 shows the first mode of the cantilever beam, the force acts on the piezoelectric patches can be simplified to 1-D model and regarded as a force F_P acts on the lateral surface as Figure 2-1 shows. In the cantilever beam type piezoelectric energy harvesting application, the first mode vibration is discussed because there is the largest strain. The larger strain means that more energy can be generated. On the assumption that the strain distribution is homogeneous and the 3-1 type piezoelectric patch is used and constitute equation (2.1) can be rearranged in Force, displacement, charge and voltage (electric potential) as shown in equation (2.2).

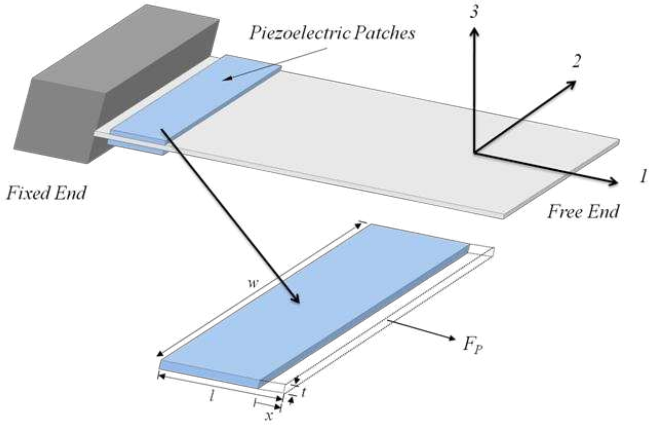

Figure 2-1. Schematic of piezoelectric harvesting cantilever beam

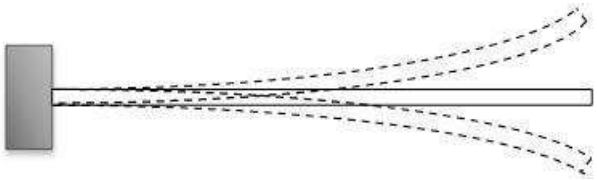

Figure 2-2. First mode vibration of the cantilever beam.

$$\begin{bmatrix} F_P \\ Q \end{bmatrix} = \begin{bmatrix} c_{11}^{E}\dfrac{w\cdot t}{l} & e_{31}w \\ e_{31}w & -\varepsilon_{33}^{S}\dfrac{w\cdot l}{t} \end{bmatrix} \begin{bmatrix} x \\ V_P \end{bmatrix} \tag{2.2}$$

where w is the width, l is the length and t is the thickness of the piezoelectric patch.

Table 2-2. Representations of the re-arranged constitutive law.

Force	$F_P = T_1 \cdot w \cdot t$
Displacement	$x = S_1 \cdot l$
Charge	$Q = D_3 \cdot w \cdot l$
Piezo terminal voltage	$V_P = -E_3 \cdot t$

In equation (2.2), the relation between force (F_P) and displacement (x) means short circuit stiffness (K_p^E), the relation between force (F_P) and piezoelectric terminal voltage (V_P) can be induced a new parameter, force-voltage coupling factor (α), and the relation between Q can V is clamped capacitance (C_0). The equation (2.2) can be rewritten as equation (2.3). The Table 2-2 & Table 2-3 give the new quantities and parameters.

Table 2-3. Representations of the governing equations.

Short circuit stiffness	$K_p^E = c_{11}^E \cdot \frac{w \cdot t}{l}$
Force-voltage coupling factor	$\alpha = e_{31} \cdot w$
Clamped capacitance	$C_0 = \varepsilon_{33}^S \cdot \frac{w \cdot l}{t}$

$$\begin{bmatrix} F_P \\ Q \end{bmatrix} = \begin{bmatrix} K_p^E & \alpha \\ \alpha & -C_0 \end{bmatrix} \begin{bmatrix} x \\ V_P \end{bmatrix} \tag{2.3}$$

To study the dynamic behavior of the piezoelectric patches, we need the relations between displacement (x) and velocity ($\dot{x}$) in mechanical part and the relations between voltage (V_P) and current (I) in electrical part. So take Laplace

transform of displacement (x) and charge (Q) into frequency domain. The governing equation of piezoelectric patches can be shown as equation (2.4).

$$\begin{cases} F_P = K_p^E x + \alpha V_P \\ I = \alpha \dot{x} - C_0 \dot{V}_P \end{cases} \tag{2.4}$$

According to the equation (2.4), the schematic model of the piezoelectric patch can be plotted as shown in Figure 2-3. The force-voltage factor (α) is the main parameter between mechanical part and electrical part. Under same force, when the force-voltage factor (α) is large, the piezoelectric patch can generate more energy. However, the above relation only exists when piezoelectric patch is under open-circuit condition. When the piezoelectric patch is connected to the load, the output voltage will be influence and then there will be a force generated in the mechanical part to induce the damping effect [44]. The damping effect will decrease the displacement of the cantilever beam and make voltage output decrease.

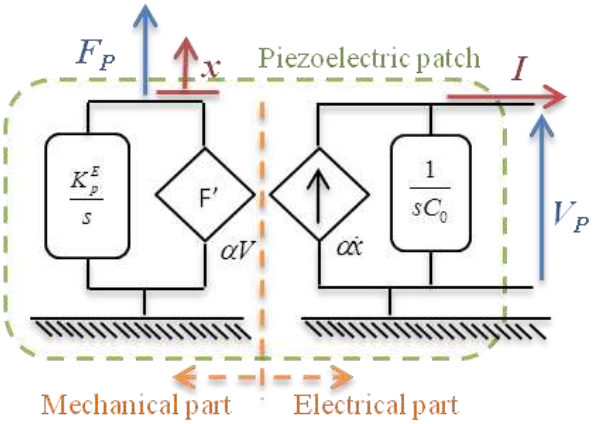

Figure 2-3. Schematic model of the piezoelectric patch

2.2 Model of piezoelectric energy harvester

The schematic of piezoelectric energy harvesting cantilever beam in Figure 2-1 can be modeled as equivalent mechanical model by mass, damper, spring and piezoelectric system as is shown in Figure 2-4.

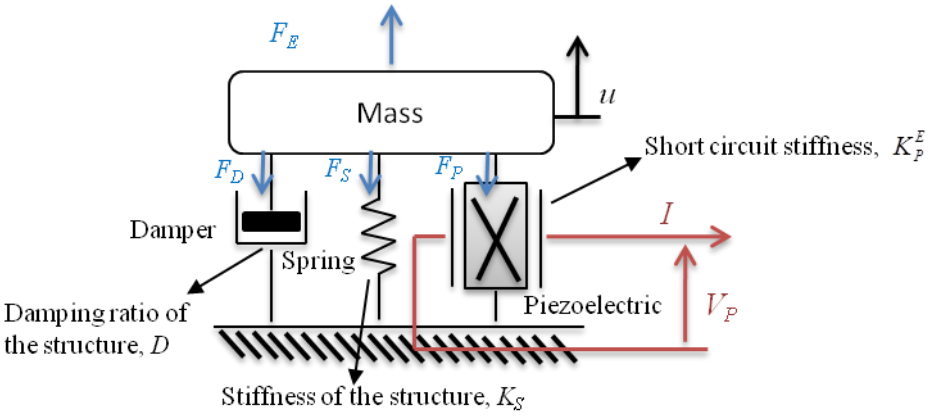

Figure 2-4. Equivalent mechanical model of piezoelectric and structure.

F_E : External driving force on the structure
F_D : Damping force from damper
F_S : Spring force from structure stiffness
F_P : Force form piezoelectric structure
x : Displacement
V_P : Voltage arcoss the piezoelectric patch
I : Current flow out from piezoelectric patch

According to Newton's laws of motion, the force equation of whole structure can be represented as equation (2.5).

$$F_E = m\ddot{x} + D\dot{x} + K^E x + \alpha V_P \tag{2.5}$$

Damping ratio of structure	D
Stiffness of structure	K_s
Equivalent stiffness of the circuit	$K^E = K_s + K_p^E$

So the governing equations of piezoelectric patch bounded on structure are shown in equation (2.6). The energy equations can be obtained by multiplying velocity ($\dot{x}$) into equation (2.6) and integrating over the time and shown in equation (2.7). The definition of energy term is shown in Table 2-4. The input energy is divided into four terms: kinetic energy, elastic energy, mechanical losses and converted energy. The

converted energy represents the sum of the energy stored in the piezoelectric capacitance and the energy delivered to the electrical load.

$$\begin{cases} m\ddot{x} + D\dot{x} + K^{E}x = F_{E} - \alpha V_{P} \\ I = \alpha \dot{x} - C_{0}\dot{V}_{P} \end{cases} \tag{2.6}$$

$$\begin{cases} \int F_{E}\dot{x}dt = \frac{1}{2}M\dot{x} + \frac{1}{2}K^{E}x^{2} + \int D\dot{x}^{2}dt + \int \alpha V_{P}\dot{x}dt \\ \int \alpha V_{P}\dot{x}dt = \frac{1}{2}C_{0}V_{P}^{2} + \int V_{P}Idt \end{cases} \tag{2.7}$$

Table 2-4. Definitions of energy terms

Input energy	$\int F_{P}\dot{x}dt$
Kinetic energy	$\frac{1}{2}M\dot{x}$
Elastic energy	$\frac{1}{2}K^{E}x^{2}$
Mechanical losses	$\int D\dot{x}^{2}dt$
Converted energy	$\int \alpha V_{P}\dot{x}dt$

2.3 Standard Interface circuit

2.3.1 Standard AC approach

The schematic diagram of piezoelectric energy harvesting device with simple resistor load is shown in Figure 2-5(a) and Figure 2-5(b) shows the waveforms including the terminal voltage of the piezoelectric patch (V_p), equivalent current generated from piezoelectric patch (I_{eq}) and displacement (x). This diagram is called standard AC approach. The equivalent circuit model of the piezoelectric energy harvester is shown in Appendix A.1. Figure 2-6 is the equivalent circuit modal of the standard AC approach and this model can be used to calculate the optimal load R and maximum power P_{max}.

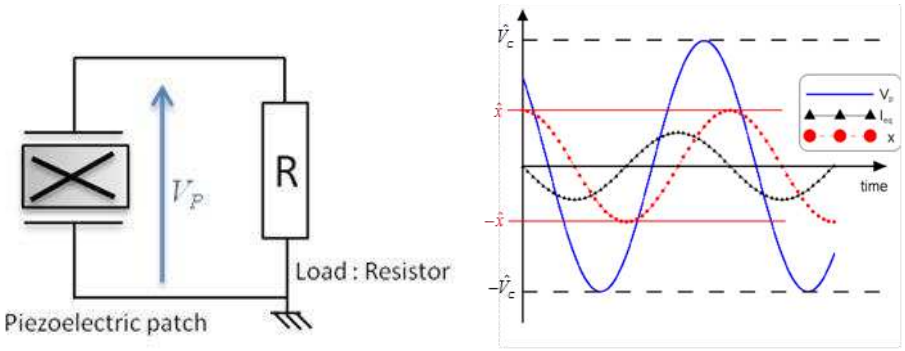

(a) (b)

Figure 2-5. (a) Schematic diagram of piezoelectric energy harvesting device with resistor load. (Standard AC approach). (b)Waveform of the standard approach.

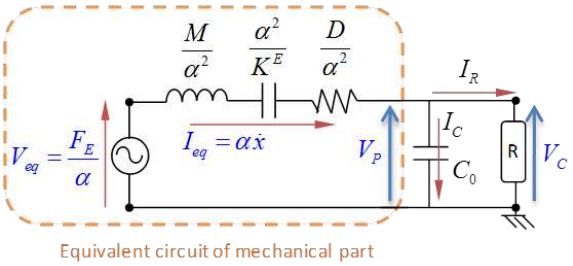

Figure 2-6. The equivalent circuit modal of standard AC approach.

The current I_R equals to equivalent current (I_{eq}) minus the current flowing in clamped capacitor (I_C). So the voltage V_C can be expressed in frequency domain as equation (2.8) shown. The relation between the external force ($\tilde{F}_E$) and displacement ($\tilde{x}$) also can be expressed in frequency domain as is shown in equation (2.9). Considering the piezoelectric energy harvesting device is driven at the resonant frequency ($\omega=\omega_n$), the force and the velocity ($\dot{x}=s\tilde{x}$) are in phase, so the equation (2.9) can be further simplified as is shown in equation (2.10).

$$\tilde{V}_C=\frac{\alpha R}{1+sC_0R}s\tilde{x} \tag{2.8}$$

s is the Laplace operator.

$$\tilde{F}_E=\left[sM+\frac{K^E}{s}+D+\frac{\alpha^2R}{1+(\omega C_0R)^2}\right]s\tilde{x} \tag{2.9}$$

$$\tilde{F}_E = \left[D + \frac{\alpha^2 R}{(\omega_n C_0 R) + 1} \right] s\tilde{x} \tag{2.10}$$

The power output from piezoelectric energy harvesting device with resistor load can be calculated using simple equation V_C^2/R. Because the waveform across the resistor is sine wave, when we calculate the output power, the voltage should be take RMS value. And because the V_C is complex, the complex conjugate should be used and the power output can be expressed as equation (2.11) shown.

$$P = \frac{V_C \cdot V_C^*}{2R} = \frac{1}{2R}\left(\frac{\alpha R s x}{1 + s C_0 R} \right)\left(\frac{-\alpha R s x}{1 - s C_0 R} \right) = \frac{\alpha^2 \omega^2 R}{1 + (\omega C_0 R)^2} \frac{\hat{x}^2}{2} \tag{2.11}$$

According to the relation between external force and displacement as equation (2.10) shown, the output power can be further expressed using external force amplitude as equation (2.12) shown. When the piezoelectric patch is low coupled to the cantilever beam, the electromechanical coefficient (k^2) is small and the force-voltage factor is close to zero ($\alpha \to 0$) and the equation (2.12) can be simplified as equation (2.13) shown.

$$P = \left(\frac{\alpha^2 R}{1+(\omega_n C_0 R)^2} \right) \frac{1}{\left(D + \frac{\alpha^2 R}{1+(\omega_n C_0 R)^2} \right)^2} \frac{\hat{F}_E^2}{2} \tag{2.12}$$

$$P = \left(\frac{\alpha^2 R}{1+(\omega_n C_0 R)^2} \right) \frac{\hat{F}_E^2}{2D^2} \tag{2.13}$$

In order to calculate the optimal resistor value R_{opt}, taking power in the partial differential equation and equals to zero, the optimal resistor load can be obtained as equation (2.14) shown. Substitute the equation (2.14) into the equation (2.13), the maxima power output of the standard AC approach can be obtained as equation (2.15) shown.

$$R_{opt} = \frac{1}{\omega_n C_0} \tag{2.14}$$

$$P_{max} = \frac{\alpha^2}{4\omega_0 C_0 D^2} \cdot \hat{F}_E^2 \tag{2.15}$$

Because the power output of the piezoelectric energy harvesting device depends on the electromechanical coefficient and mechanical quality factor of the structure, according to the definition of the electromechanical coefficient and the mechanical quality factor, a new parameter is defined as equation (2.16) shown. The

electromechanical coefficient is shown in Appendix A.2. Through the equation (2.16), the output power of the standard AC approach can be plotted as a function of the load R and the parameter k^2Q_m at resonance as Figure 2-7 shown. Q_m is the mechanical quality factor and k^2 the electromechanical coupling factor. For weakly coupled structure k^2Q_m is lower than 2 [75]. When k^2Q_m is lower than 2, the SSHI technique can effectively increase the power than the standard interface circuit.

$$k^2Q_m = \frac{\alpha^2}{DC_0}\sqrt{\frac{M}{K_p^D}} \tag{2.16}$$

where

Mechanical quality factor $\quad Q_m = \frac{\sqrt{MK}}{D}$

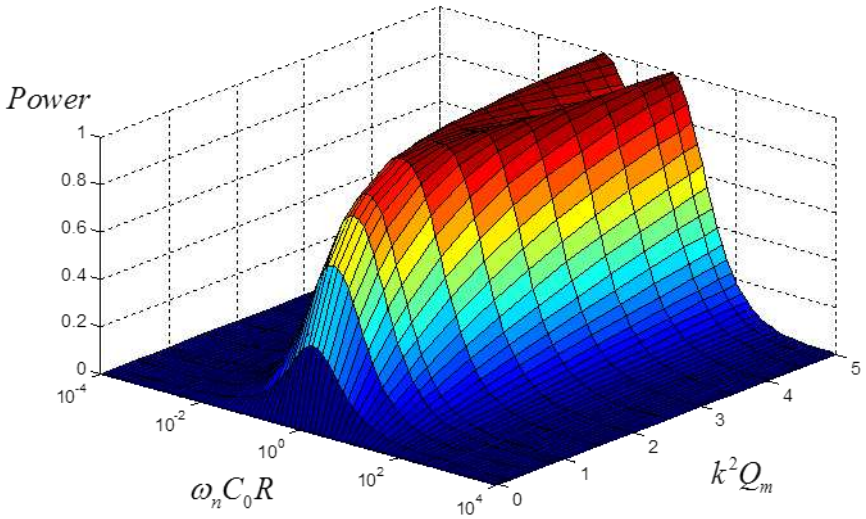

Figure 2-7. Normalized power as a function of the normalized load resistance and the electromechanical parameters.

Using work-cycle to present and compare the generating energy from the piezoelectric energy harvesting device is a good method. It's easy to show the generating energy from the plot. Figure 2-8 shows the work-cycle of the standard AC approach. The y-axis is the equivalent force (αV) and the x-axis is the displacement (x). The work-cycle area means the energy which the piezoelectric energy harvesting device can generate, so if the work-cycle is larger, it means that more energy can be obtained.

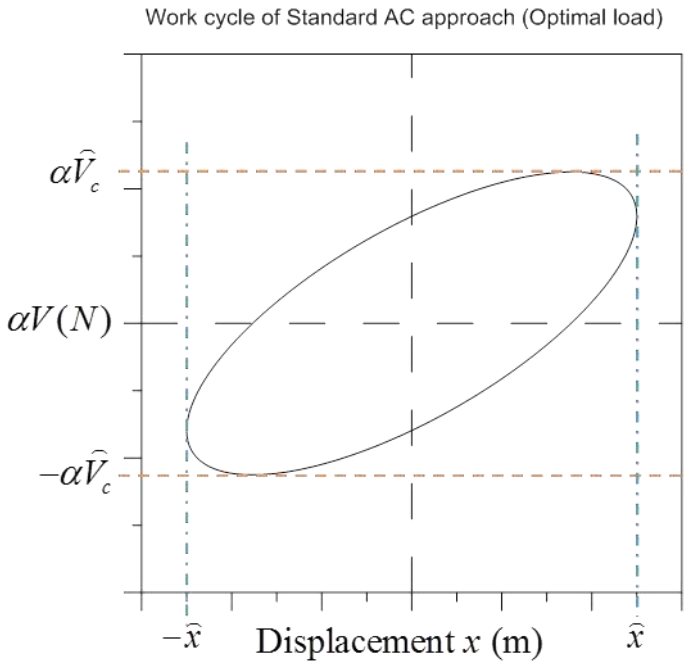

Figure 2-8. Work cycle of the standard AC approach (optimal load).

2.3.2 Standard DC approach

The schematic diagram of piezoelectric energy harvesting device with full-bridge rectifier and resistor load is shown in Figure 2-9. This is called standard DC approach. Assuming the structure is excited at resonant frequency and from the governing equation, the exciting source can be modeled as a current source model as Figure 2-10 shown. C_r is the rectifier capacitor to regulate the output voltage. Figure 2-11 shows the waveform of standard DC approach including terminal voltage across piezoelectric (V_P), current source (I_{eq}) and displacement (x).

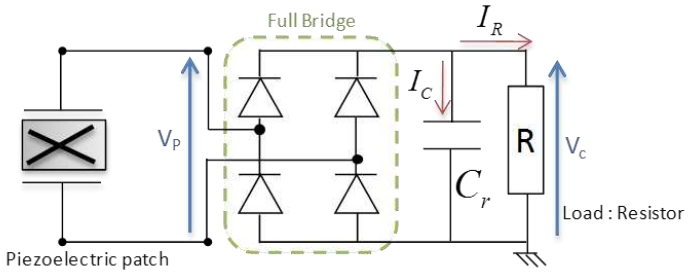

Figure 2-9. Schematic diagram of piezoelectric energy harvesting transducer with a simple resistor load. (Standard DC approach).

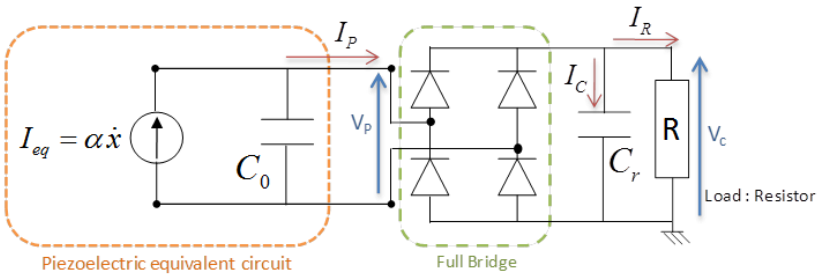

Figure 2-10. The equivalent circuit diagram of the Standard DC approach.

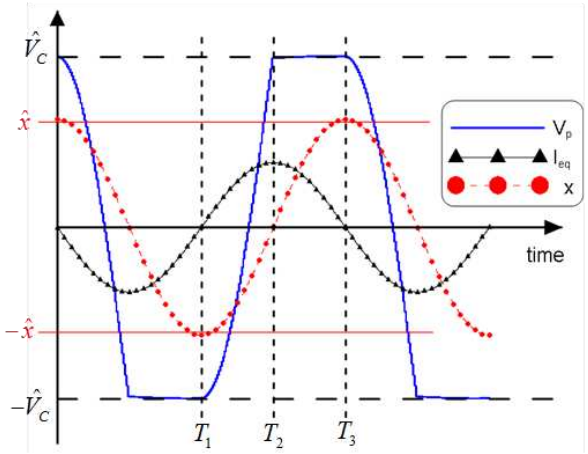

Figure 2-11. Waveform of the Standard DC approach.

The detailed time interval discussion is shown in Appendix A.3 and the output voltage $\hat{V}_C$ can be obtain as the equation (2.17) shown.

$$\hat{V}_C = \frac{2\alpha R\omega_0}{2C_0 R\omega_0 + \pi}\hat{x} \tag{2.17}$$

The output power from piezoelectric energy harvesting transducer with standard DC approach can be calculated using simple equation $\hat{V}_C^2/R$ as the equation (2.18) shown.

$$P = \frac{\hat{V}_C^2}{R} = \frac{4\alpha^2 R\omega_0^2}{\left(2C_0 R\omega_0 + \pi\right)^2}\hat{x}^2 \tag{2.18}$$

In order to calculate the optimal resistor R_{opt}, take the equation (2.18) in partial differential equation to R and equals to zero and the R_{opt} can be obtain as equation (2.19) shown.

$$R_{opt} = \frac{\pi}{2C_0\omega_0} \tag{2.19}$$

Substituting the R_{opt} into the equation (2.18), the maxima power output (P_{max}) can be obtained as equation (2.20) shown.

$$P_{max}\Big|_{R=R_{opt}} = \frac{\alpha^2\omega_0}{2\pi C_0}\hat{x}^2 \tag{2.20}$$

Substituting the optimal load (R_{opt}) into equation (8.16) and equation (8.13), the voltage $\hat{V}_C$ and time T_2 during optimal load condition can be obtain as equation (2.21) and equation (2.22) shown.

$$\hat{V}_C\Big|_{R=R_{opt}} = \frac{2\alpha\left(\frac{\pi}{2C_0\omega_0}\right)\omega_0}{2C_0\omega_0\left(\frac{\pi}{2C_0\omega_0}\right)+\pi}\hat{x} = \frac{\alpha}{2C_0}\hat{x} \tag{2.21}$$

$$T_2\Big|_{R=R_{opt}} = \frac{T_0}{4} \tag{2.22}$$

The work cycle of the standard DC approach with optimal load can be plotted as Figure 2-12. Because the full-bridge rectifier, the αV is constrained between $\alpha\hat{V}_C$ and $-\alpha\hat{V}_C$. The shape is a parallelogram.

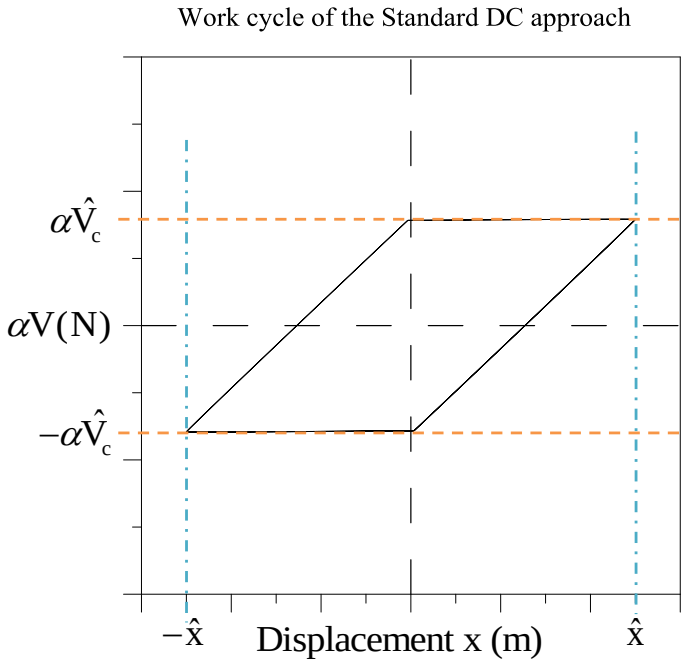

Figure 2-12. Work cycle of the Standard DC approach with optimal load

2.4 Analysis of the synchronized switching technique

In energy harvesting applications, the piezoelectric elements convert the vibration energy of the host structure into the electrical energy, and then the generated electrical energy is stored in a storage buffer. Since the piezoelectric element has large clamped capacitance, an impedance matching circuit is required to maximize the generated

power. It is known that an inductor can be added to compensate the contribution of the piezoelectric clamped capacitor [26], but it cannot be adaptive to the environmental variations and the value of the inductance is too large in a low frequency range. To overcome this drawback, switching-type interfaces were proposed and popularly used in recent years [76]. In the switching circuits, the switches are operated synchronously with the vibration of the host structure in order to optimize the power flow.

Several synchronized switching circuit topologies and corresponding switching laws were proposed. They can be classified into two groups according to the placement of the rectifier and the active switches. The first group of the switching circuits places the switches between piezoelectric element and the rectifier, such as parallel-SSHI (Synchronized Switching Harvesting on an Inductor) and series-SSHI [33, 77]. This group of techniques is used to modify the waveform of the piezoelectric voltage, i.e. the voltage across the piezoelectric element, in order to increase the collected power in the weakly coupled structure. The second group places the switches between the rectifier and the storage buffer, such as SECE technique [32]. This second group of techniques is used to modify the charging current flowing into the storage buffer in order to fasten the charging speed and to make a load adaptation.

In this dissertation, the parallel-SSHI technique and series-SSHI technique will be

used to increase the efficiency. So in the following two sub-suctions these two technique will be discussed in detail.

2.4.1 Synchronized Switch Harvesting on Inductor in parallel (parallel-SSHI)

The schematic diagram of Synchronized switching harvesting on inductor in parallel (parallel-SSHI) piezoelectric energy harvesting device with full-bridge rectifier to a simple resistor load is shown in Figure 2-13. This is called SSHI technique. Assuming the structure is excited at resonant frequency and from the governing equation, the piezoelectric energy harvesting device can be modeled as a current source parallel with a clamped capacitor and the equivalent circuit of entire system is shown as Figure 2-14. Figure 2-15 shows the waveform of SSHI-parallel including voltage across piezoelectric V_P, current source I_{eq} and displacement x.

In this technique, a bi-directional switch and an inductor L are added in parallel with the piezoelectric patch. The switch is conducted at each maximum and minimum of the displacement or at the zero crossing of the vibration velocity, in order to reverse the voltage across the piezoelectric element and put it in phase with velocity. The result is that the energy stored in the structural clamped capacitor (C_0) is extracted by the LC resonance and achieve to a minimum value, and thus the piezoelectric voltage can be

increased [78]. The harvested energy of the system with the SSHI technique is similar to that using the standard interface under the strongly coupled condition [49]. When the vibration velocity crosses zero, the switch is conducted, the inductor L and the clamped capacitor (C_0) begin to oscillate. This resonant circuit increases the magnitude and changes the polarity of the voltage across the piezoelectric capacitance sinusoidal, and thus put voltage (V_p) and velocity ($\dot{x}$) in phase, which indicates that more energy is extracted from the vibration source.

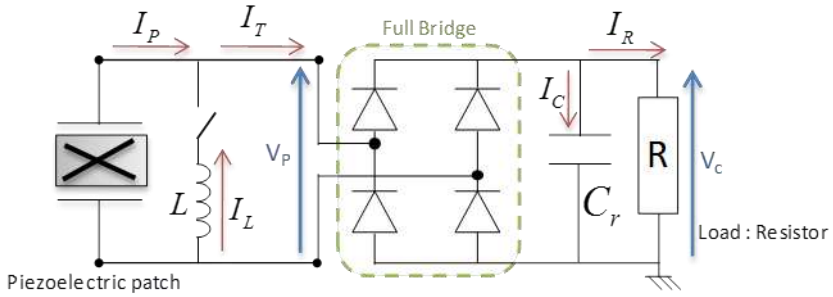

Figure 2-13. Schematic diagram of parallel-SSHI piezoelectric energy harvesting device with full bridge rectifier to a simple resistor load.

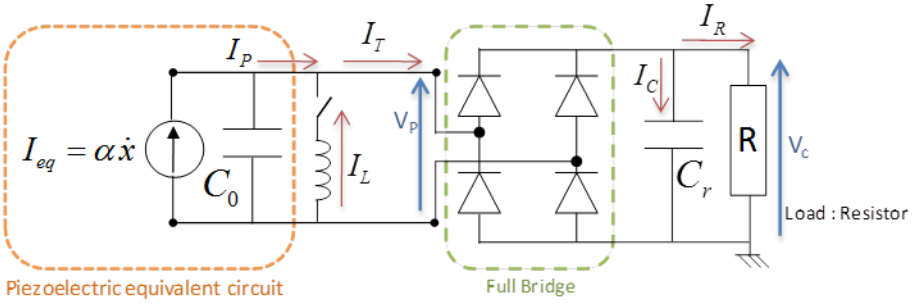

Figure 2-14. The equivalent circuit diagram of the parallel-SSHI piezoelectric energy harvesting device.

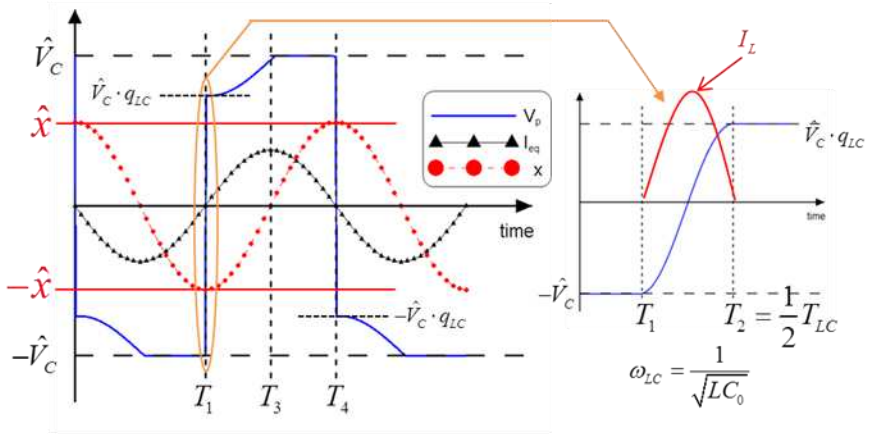

Figure 2-15. Waveform of the parallel-SSHI piezoelectric energy harvesting device.

The detailed analysis of the each time interval (From T_1 to T_4) is shown in Appendix A.4. The $\hat{V}_C$ can be obtained and the result is shown in equation (2.23).

$$\hat{V}_C = \frac{2\alpha R\omega_0}{\pi + (1 - q_{LC}) C_0 R\omega_0} \hat{x} \tag{2.23}$$

The power output from piezoelectric energy harvesting device with parallel-SSHI can be calculated using simple equation V^2/R as the equation (2.24) shown.

$$P = \frac{\hat{V}_C^2}{R} = \frac{4\alpha^2 R\omega_0^2}{\left[\pi + (1 - q_{LC}) C_0 R\omega_0\right]^2} \hat{x}^2 \tag{2.24}$$

In order to calculate the optimal resistor R_{opt}, take the equation (2.24) in partial differential equation to R and equals to zero as equation (2.25) shown and the optimal resistor (R_{opt}) can be obtain as equation (2.26) shown.

$$\frac{\partial P}{\partial R}=\frac{4\alpha^2\cdot\left[\pi+\left(1-q_{LC}\right)C_0R\omega_0\right]^2-\left(4\alpha^2R\right)\cdot 2\cdot\left(1-q_{LC}\right)C_0\omega_0\cdot\left[\pi+\left(1-q_{LC}\right)C_0R\omega_0\right]}{\left[\pi+\left(1-q_{LC}\right)C_0R\omega_0\right]^4}\omega_0^2\hat{x}^2=0 \tag{2.25}$$

$$R_{opt}=\frac{\pi}{\left(1-q_{LC}\right)C_0\omega_0} \tag{2.26}$$

Substituting the optimal resistor (R_{opt}) into the equation(2.24), the maxima power output (P_{max}) can be obtained as equation (2.27) shown.

$$P_{max}\big|_{R=R_{opt}}=\frac{\alpha^2\omega_0^2}{\pi\left(1-q_{LC}\right)C_0\omega_0}\hat{x}^2 \tag{2.27}$$

The voltage $\hat{V}_C$ and time T_3 under optimal load condition can be obtain as

equation (2.28) and equation (2.29) shown.

$$\hat{V}_C\big|_{R=R_{opt}} = \frac{2\alpha\omega_0}{\pi+\pi}\cdot\frac{\pi}{(1-eq_{LC})C_0\omega_0}\hat{x} = \frac{\alpha}{C_0(1-q_{LC})}\hat{x} \tag{2.28}$$

$$\begin{aligned} T_2\big|_{R=R_{opt}} &= \frac{1}{\omega_0}\cos^{-1}\left[\frac{C_0}{\hat{x}\alpha}(1-q_{LC})\hat{V}_C\big|_{R=R_{opt}} - 1\right] = \frac{1}{\omega_0}\cos^{-1}(0) \\ \Rightarrow T_2\big|_{R=R_{opt}} &= \frac{T_0}{4} \end{aligned} \tag{2.29}$$

The work-cycle of the parallel-SSHI with optimal load can be plotted as Figure 2-16.

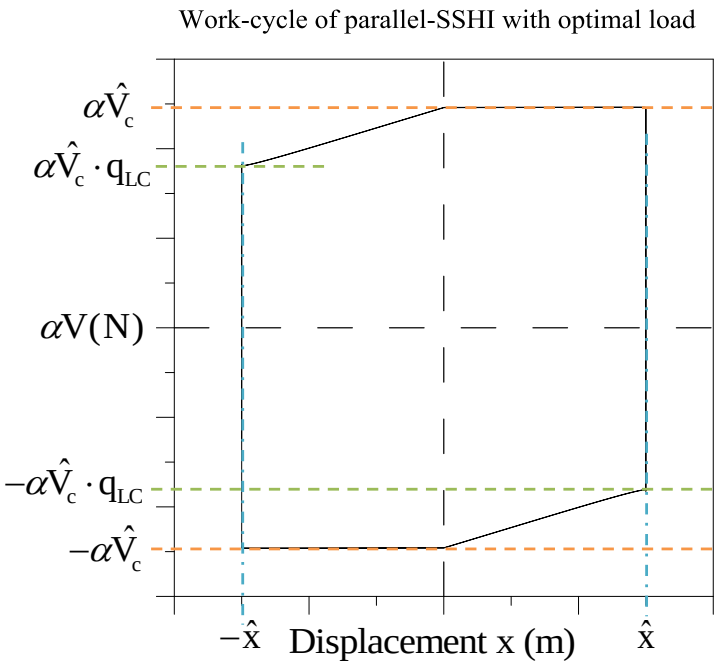

Figure 2-16. Work-cycle of the parallel-SSHI.

2.4.2 Synchronized Switch Harvesting on Inductor in Series (Series-SSHI)

The schematic diagram of synchronized switching harvesting on inductor in series (Series-SSHI) piezoelectric energy harvesting device with full-bridge rectifier to a simple resistor load is shown in Figure 2-17. the piezoelectric energy harvesting device can be modeled as a current source parallel with a clamped capacitor and the equivalent circuit of entire system is shown as Figure 2-18. Figure 2-19 shows the waveform of series-SSHI including voltage across piezoelectric V_P, voltage across load V_C, current source I_{eq} and displacement x.

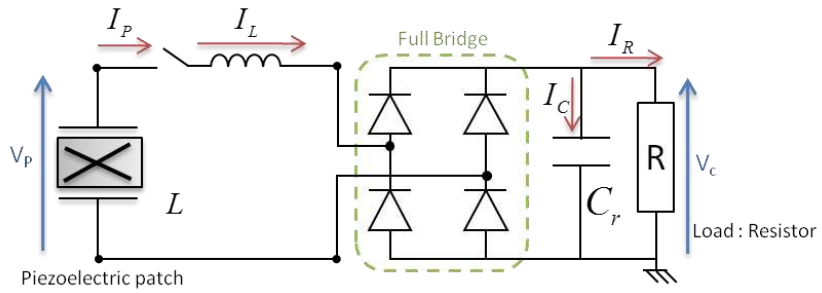

Figure 2-17. Schematic diagram of series-SSHI piezoelectric energy harvesting device with full bridge rectifier to a resistor load

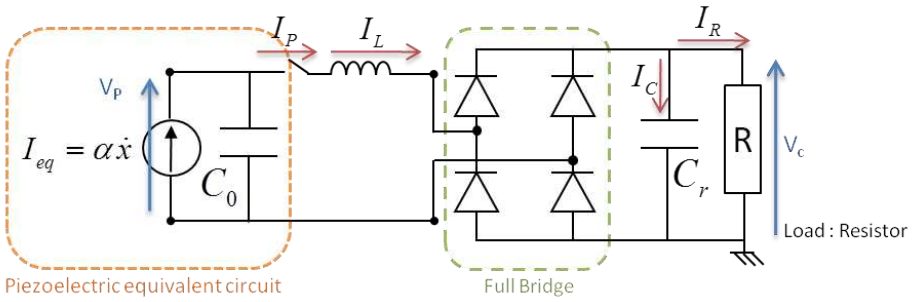

Figure 2-18. The equivalent circuit diagram of the series-SSHI piezoelectric energy harvesting device.

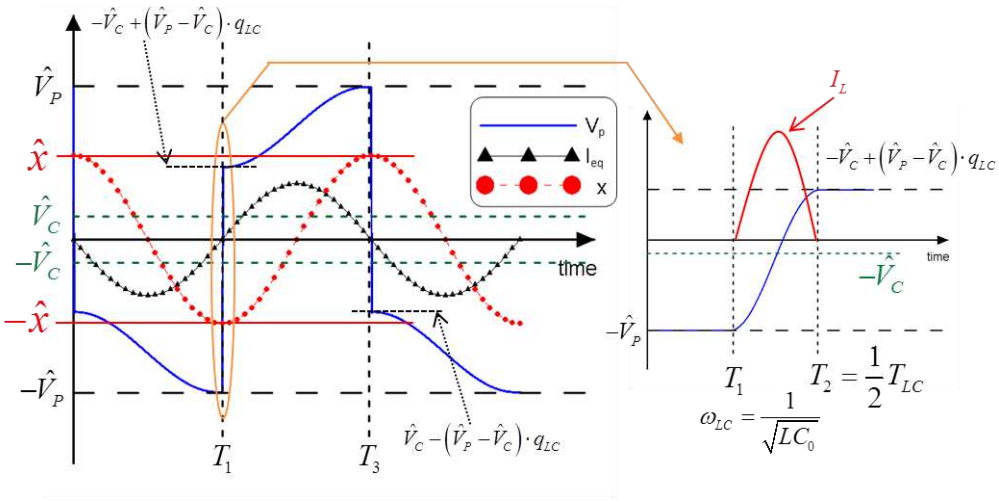

Figure 2-19. Waveform of the series-SSHI piezoelectric energy harvesting device.

The detailed analysis of the each time interval (From T_1 to T_4) is shown in Appendix A.5. The maxima V_C ($\hat{V}_C$) can be obtained and the result is shown in equation (2.30).

$$\hat{V}_C = \frac{2\alpha R(1+q_{LC})}{2R\omega_0 C_0(1+q_{LC})+\pi(1-q_{LC})}\omega_0\hat{x} \tag{2.30}$$

The power output from piezoelectric energy harvesting device with seris-SSHI can be calculated using simple equation V^2/R as the equation (2.31) shown.

$$P = \frac{\hat{V}_C^2}{R} = \frac{4\alpha^2 R\left(1+q_{LC}\right)^2}{\left[2R\omega_0 C_0\left(1+q_{LC}\right)+\pi\left(1-q_{LC}\right)\right]^2}\omega_0^2\hat{x}^2 \tag{2.31}$$

In order to calculate the optimal resistor R_{opt}, take the equation (2.31) in partial differential equation to R and equals to zero and the R_{opt} can be obtain as equation (2.32) shown.

$$R_{opt} = \frac{\pi\left(1-q_{LC}\right)}{2\omega_0 C_0\left(1+q_{LC}\right)} \tag{2.32}$$

Substituting the R_{opt} into the equation (2.31), the maxima power output (P_{max}) of series-SSHI can be obtained as equation (2.33) shown.

$$P_{max}\big|_{R=R_{opt}} = \frac{\alpha^2\left(1+q_{LC}\right)}{2\pi C_0\left(1-q_{LC}\right)}\omega_0\hat{x}^2 \tag{2.33}$$

Substituting the R_{opt} into equation (8.31), the voltage $\hat{V}_C$ under optimal load condition can be obtained as equation (2.34).

$$\begin{aligned}\hat{V}_C\big|_{R=R_{opt}} &= \frac{2\alpha R_{opt}\left(1+q_{LC}\right)}{2R_{opt}\omega_0 C_0\left(1+q_{LC}\right)+\pi\left(1-q_{LC}\right)}\omega_0\hat{x} \\ \Rightarrow \hat{V}_C\big|_{R=R_{opt}} &= \frac{\alpha}{2C_0}\hat{x}\end{aligned} \tag{2.34}$$

According to the waveform in the Figure 2-20, the work cycle can be plotted as

Figure 2-20.

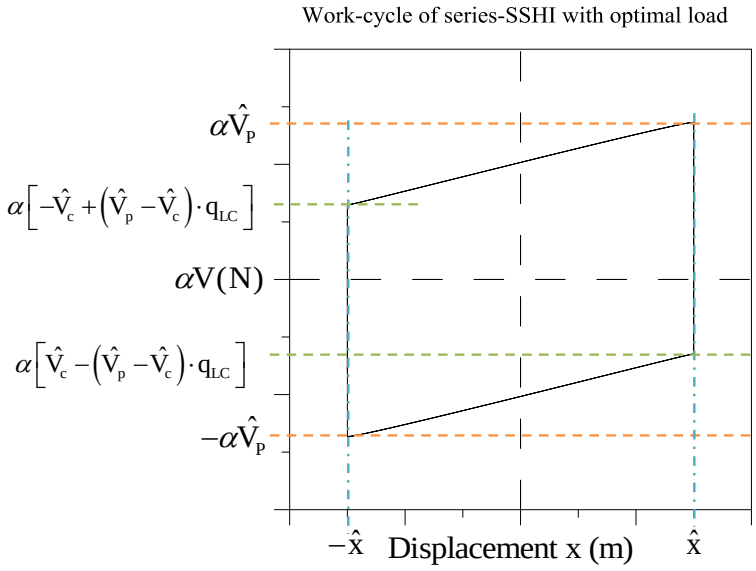

Figure 2-20. Work cycle of the series-SSHI with optimal load.

2.5 Discussion of the energy harvesting interface circuits

2.5.1 Power output discussion

The above sub-sections show the theoretical analysis of the standard interface circuits and the synchronized switching technique circuits and in this sub-section the power output of the interface circuits are compared and discussed. From the equation (2.18), equation (2.24) and equation (2.31), the power output of the standard DC approach, parallel-SSHI, and series-SSHI can be obtained by using the same displacement to make system be driven under the same excitation. The output power and the load resistor can be normalized by the maximal output power and the optimal

resistor load of the standard DC approach and the results are shown in Figure 2-21. The piezoelectric is weakly coupled to structure and k^2Q_m is 1.6×10^{-4} (much lower than 2) to plot the Figure 2-23. The standard AC approach doesn't be compared here because in the real application the AC output energy cannot be used to supply the WSN module or other portable devices. The parallel and series SSHI is plotted using three different quality factors: $Q_I = 1.5$, 2.5 and 3.5. The optimal resistor load and maxima output power of different techniques are marked in star in Figure 2-21. The following are the comparison of the power output and resistor load.

1. Resistor load comparison.

From the results, it's obviously that the optimal load of parallel-SSHI are always higher than standard DC approach. From $Q_I = 1.5$ to 3.5, the optimal load of parallel-SSHI are 3.08, 4.28 and 5.52 times than standard case. For the series-SSHI, the optimal resistor load is opposite to the parallel-SSHI. From $Q_I = 1.5$ to 3.5, the optimal load of series-SSHI are 0.48, 0.32 and 0.24 times than standard case. In the parallel-SSHI case, the higher quality factor Q_I needs higher optimal resistor load. On the contrary, in the series-SSHI, the higher quality needs lower optimal resistor load. So according to the different load, the proper synchronized switching technique can be chosen to achieve the maxima output power.

2. Output power comparison

Comparing the synchronized switching technique with standard DC approach whatever parallel-SSHI or series-SSHI, the power output is always higher and it shows the switching technique is an effective technique to increase the output power of the piezoelectric energy harvesting device. The higher quality factor Q_I can lead higher output power. From $Q_I = 1.5$ to 3.5, the maxima power output of parallel-SSHI are 3.08, 4.29 and 5.53 times than standard case. For series-SSHI the optimal load are 2.08, 3.29 and 4.52 times than standard case. Comparing the parallel-SSHI to series-SSHI, under the same quality factor Q_I, the power output of parallel-SSHI is little higher than series-SSHI. However, in the real application the quality factor Q_I is constrained and the range from 1.5 to 3.5 is the reasonable value. If the system wants to achieve very high Q_I value such as 10, it needs very expensive elements in the circuit and the cost will be very high. But it's meaningless to establish a expensive energy harvesting device.

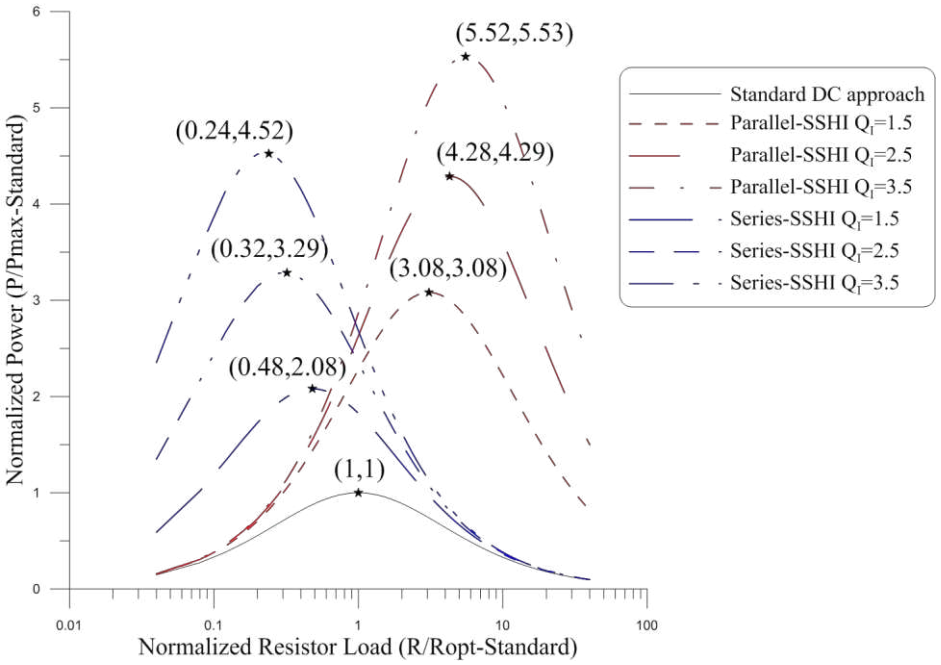

Figure 2-21. Normalized power VS Normalized Resistor Load.

2.5.2 Work-cycle discussion

According to the energy equation (2.7), the converted energy means the energy transferred from the external energy and it can be easily plotted by measuring the terminal voltage of the piezoelectric patch and multiplied the force-voltage factor (α) in y-axis and measuring the tip displacement (x) of the cantilever beam. The unit of the y-axis is Newton (N) and the x-axis is meter (M), so the enclosed area represent the transferred energy (J) and this plot is called work-cycle. Work-cycle is a simple way to show and compare the increased efficiency of the interface circuits for the energy harvesting device. When the enclosed area is larger, it means the more energy are

transferred from the vibration energy and if the external energy is the same, larger enclosed area means the higher efficiency. According to the equation (2.21), (2.23), and (2.34), we can plot the work-cycles of the standard DC approach, parallel-SSHI and series-SSHI techniques in the same plane at the optimal load as Figure 2-22 by giving the same displacement (x), force-voltage factor (α), inverting quality factor (q_{LC}) and clamped capacitor (C_0) to assume that it's the same piezoelectric patch connected to different interface circuits.

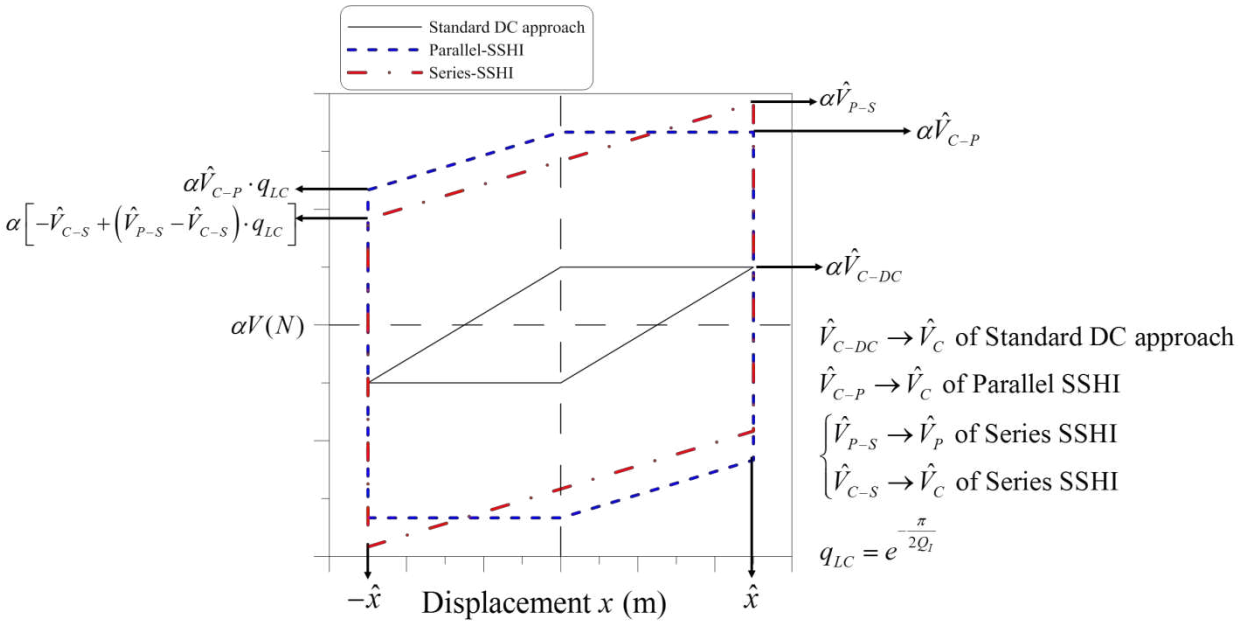

Figure 2-22. Work-cycles comparison of different interface circuits.

As the enclosed area is the transferred energy from piezoelectric patch, the

following are the discussion of each technique.

1. Standard DC approach:

The work-cycle of the standard DC approach is a parallelogram, so the area can be calculated by the equation (2.35). And substitute the equation (2.21) into the equation (2.35), the transferred energy of standard DC approach at optimal load can be obtain as equation (2.36).

$$E_{DC} = 2\alpha\hat{V}_{C-DC} \cdot 2\hat{x} = 4\alpha\hat{V}_{C-DC}\hat{x} \tag{2.35}$$

$$E_{DC} = 2\frac{\alpha^2}{C_0}\hat{x}^2 \tag{2.36}$$

2. Parallel SSHI technique:

From the Figure 2-22, the enclosed area of the parallel-SSHI can be calculated as equation (2.37). And by substituting the equation $\hat{V}_{C-P}$ into equation (2.37), the transferred energy of parallel-SSHI at the optimal load can be obtained as equation (2.38).

$$\begin{aligned} E_{\text{Parallel-SSHI}} &= 2\alpha\hat{V}_{C-P}\cdot 2\hat{x} - \left(\alpha\hat{V}_{C-P} - \alpha\hat{V}_{C-P}\cdot q_{LC}\right)\hat{x} \\ &= 4\alpha\hat{V}_{C-P}\hat{x} - \left(1-q_{LC}\right)\alpha\hat{V}_{C-P}\hat{x} \end{aligned} \tag{2.37}$$

$$E_{\text{Parallel-SSHI}} = 4\frac{\alpha^2}{C_0\left(1-q_{LC}\right)}\hat{x}^2 - \frac{\alpha^2}{C_0}\hat{x}^2 \tag{2.38}$$

3. Series-SSHI:

The enclosed area of the series-SSHI is also a parallelogram like standard DC approach, so the area can be calculated as equation (2.39). And by substitute the equation $\hat{V}_C$ into equation (2.39), the transferred energy of series-SSHI at optimal load can be obtained as (2.40).

$$\begin{aligned} E_{\text{Series-SSHI}} &= \left\{\hat{V}_{P-S} + \left[-\hat{V}_{C-S} + \left(\hat{V}_{P-S} - \hat{V}_{C-S}\right)q_{LC}\right]\right\}\cdot 2\alpha\hat{x} \\ &= 4\left[\frac{\alpha^2\hat{x}^2}{C_0} - \alpha\hat{x}\cdot\hat{V}_C\right]\frac{\left(1+q_{LC}\right)}{\left(1-q_{LC}\right)} \end{aligned} \tag{2.39}$$

$$E_{\text{Series-SSHI}} = 2\frac{\alpha^2}{C_0}\frac{\left(1+q_{LC}\right)}{\left(1-q_{LC}\right)}\hat{x}^2 \tag{2.40}$$

Using the transformed energy of the standard DC approach as the standard, the

ratio of the parallel-SSHI to standard technique is $E_{\Delta 1}$ as equation (2.41) and the ratio of the series-SSHI to standard technique is $E_{\Delta 2}$ as equation (2.42). Using different inverting quality factor (q_{LC}) the energy ratio curves can be plotted as Figure 2-23. From the plot, the energy ratio of the parallel-SSHI is always little higher than series-SSHI and when the inverting quality factor is higher, the series-SSHI is much closer to the parallel-SSHI. In the low inverting quality factor, the energy ratio is higher than 1, it shows even high electrical losses in the synchronized switching technique the efficiency is still better than standard technique.

$$E_{\Delta 1} = \frac{E_{parallel-SSHI}}{E_{DC}} = \frac{2}{(1-q_{LC})} - \frac{1}{2} \tag{2.41}$$

$$E_{\Delta 2} = \frac{E_{series-SSHI}}{E_{DC}} = \frac{(1+q_{LC})}{(1-q_{LC})} \tag{2.42}$$

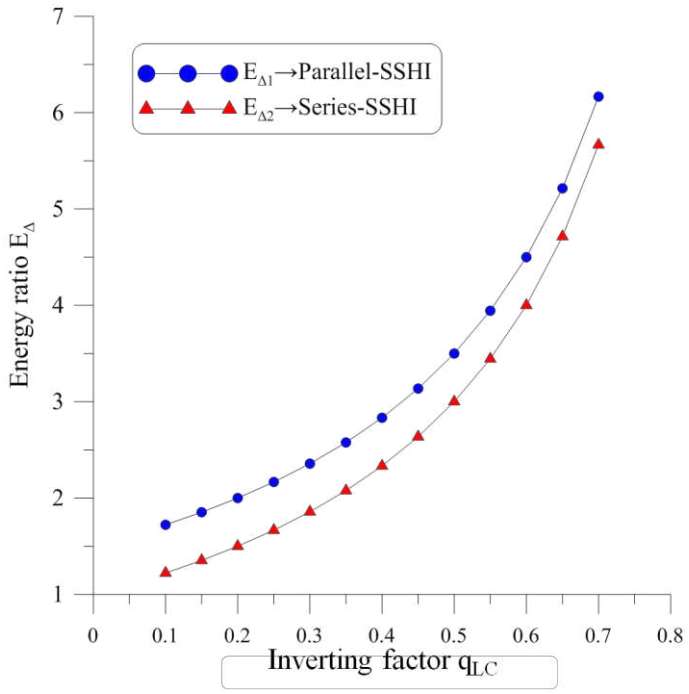

Figure 2-23. Energy ratio E_{Δ} vs. Inverting factor q_{LC}.

2.6 Theoretical analysis of interface circuits of structural damping

2.6.1 Synchronized Switching Damping on a Short circuit (SSDS)

Another application of the previous SSHI interfaces is semi-passive structural damping. In this application, the synchronized switching technique is used to extract energy from the structure in order to damp the vibration. One of these techniques is called SSDS (Synchronized Switching Damping on Short circuit). It is a semi-passive technique first presented by Richard et al. in 1999 [67]. The schematic diagram of SSDS technique using piezoelectric patch is shown in Figure 2-25. The SSDS technique is composed of a piezoelectric patch and two-way switches. The two-way switches usually

are composed of two MOSFET (metal oxide semiconductor field effect transistor). The equivalent circuit of SSDS technique is shown in Figure 2-25. The waveforms of the SSDS technique are shown in Figure 2-26. The switches turn on when the displacement x or piezoelectric terminal voltage V_p reaches to the maxima and minima value.

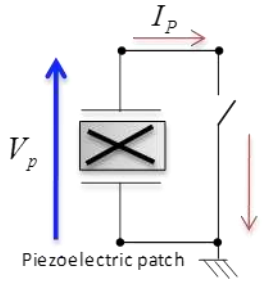

Figure 2-24 Schematic diagram of synchronized switching damping on short circuit (SSDS).

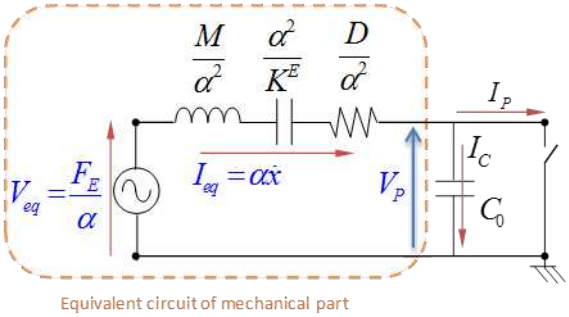

Figure 2-25. The equivalent circuit diagram of the synchronized switching damping on a short circuit (SSDS).

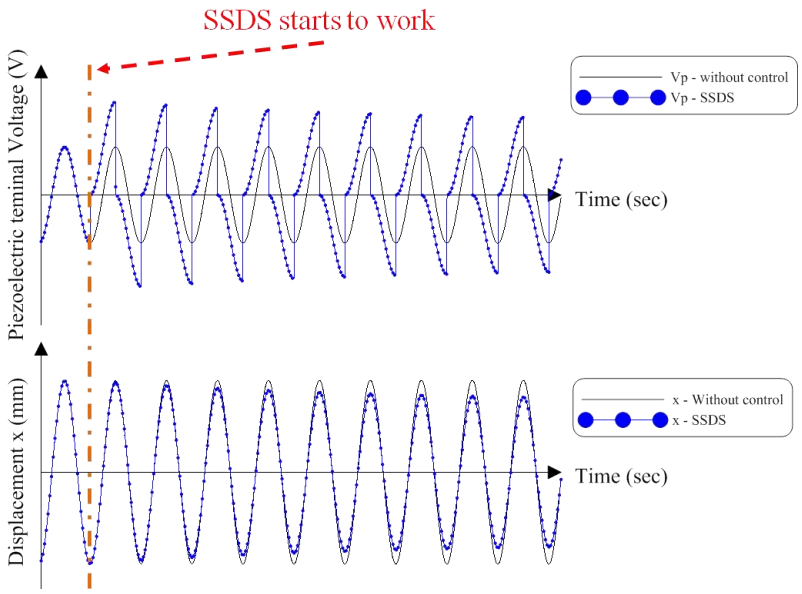

Figure 2-26. Waveforms of the SSDS technique.

According to the energy equation (2.7) and integrating over a period (T), the energy equation can be expressed as equation (2.43). The first and second terms in the right-hand side are kinetic and elastic energies. When integrating over a period, these two terms will vanish as they are periodic function and the energy equation will be simplified as equation (2.44). It means that the external energy will turn into viscous energy (mechanical losses) and electrical energy dissipated in the interfacing circuit. Thus the switching damping energy is shown in equation (2.45). The Vp waveform of SSDS can be decomposed of two waveforms $V_1(t)$ and $V_2(t)$ as Figure 2-27(b) and Figure 2-27(c). The piezoelectric patch is short-circuited during the LC resonance and

most time in one period is open-circuited ($I_P = 0$). So the magnitude of the $V_P(t)$ can be obtained from integrating the current flow out from piezoelectric patch (I_P) over half LC resonant period and is shown in equation (2.46).

$$\int_0^T F\dot{x}dt = \frac{1}{2}M\dot{x}\Big|_0^T + \frac{1}{2}K^E x^2\Big|_0^T + \int_0^T D\dot{x}^2 dt + \int_0^T \alpha V_P \dot{x}dt \tag{2.43}$$

$$\int_0^T F\dot{x}dt = \int_0^T D\dot{x}^2 dt + \int_0^T \alpha V_P \dot{x}dt \tag{2.44}$$

$$E_S = \int_0^T \alpha V_P \dot{x}dt \tag{2.45}$$

$$\begin{aligned} &\int_0^{\frac{T_{LC}}{2}} I_P dt = \int_0^{\frac{T_{LC}}{2}} \left(\alpha\dot{x} - C_0 V_P\right) dt = 0 \\ &\Rightarrow \hat{V}_{P-SSDS} = 2\frac{\alpha}{C_0}\hat{x} \end{aligned} \tag{2.46}$$

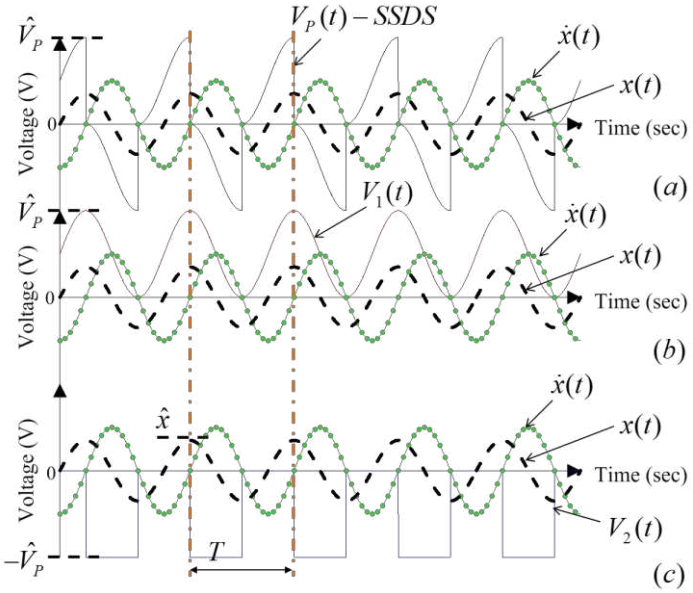

Figure 2-27. Waveforms of (a) SSDS can be decomposed of (b) $V_1(t)$ and (c) $V_2(t)$.

As the $V_P(t)$ can be decomposed of two waveforms, the switching damping energy can be rewritten as equation (2.47). The $V_1(t)$ integrate with the velocity ($\dot{x}$) will turn into zero because they are 90 degree phase lag. The $V_2(t)$ is a 50% duty cycle square wave so when integrating one period will equal to integrate only half period. Finally, the SSDS switching damping energy can be expressed as equation (2.48).

$$E_S = \alpha \int_0^T V_1(t)\dot{x}dt + \alpha \int_0^T V_2(t)\dot{x}dt \tag{2.47}$$

$$\begin{aligned} E_{S-SSDS} &= \alpha \int_0^T V_2(t)\dot{x}dt = \alpha \int_0^{\frac{T}{2}} \left(2\frac{\alpha}{C_0}\hat{x} \right)\dot{x}dt \\ \Rightarrow E_{S-SSDS} &= 4\frac{\alpha^2}{C_0}\hat{x}^2 \end{aligned} \tag{2.48}$$

2.6.2 Synchronized switching damping on an inductor (SSDI)

The synchronized switching damping on an inductor (SSDI) technique is proposed in this sub-section. The SSDI technique is further improved from the SSDS technique and presented by Richard et Al. in 2000 [68]. The damping ability of SSDI technique is more powerful than the SSDS technique. The schematic diagram of SSDI technique using piezoelectric patch is shown in Figure 2-28. The SSDI technique is composed of a

piezoelectric patch, two-way switches and an inductor. The two-way switches usually are composed of two MOSFET (metal oxide semiconductor field effect transistor) like traditional switching technique. The inductor used here is like in SSHI technique and through the resonance between the inductor and the clamped capacitor of piezoelectric, the more energy can be attracted from piezoelectric patch to damp the structural vibration. The equivalent circuit of SSDI technique is shown in Figure 2-29 and the waveforms of the SSDI technique is shown in Figure 2-30. The switches turn on when the displacement x or piezoelectric terminal voltage V_p reaches to the maxima and minima value. From the Figure 2-30, there is a transient period. In this transient period, the SSDI turns on and the terminal voltage of the piezoelectric patch will increase first and then decrease to the stable state. In the SSHI technique, the piezoelectric patch is low coupled to the structure, so the displacement is assumed to keep the same. When SSHI technique turns on, the displacement doesn't be changed and the terminal voltage will only increase to stable state. However, in SSDI technique, when SSDI turns on the displacement will start to decrease and make the terminal voltage decrease. Finally the system will reach to the stable state.

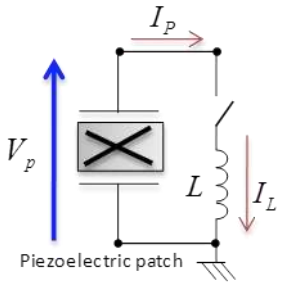

Figure 2-28. Schematic diagram of synchronized switching damping with and Inductor (SSDI).

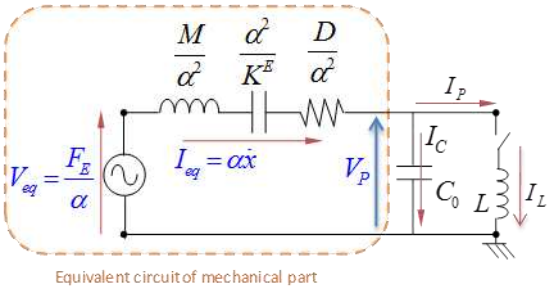

Figure 2-29. The equivalent circuit diagram of SSDI technique.

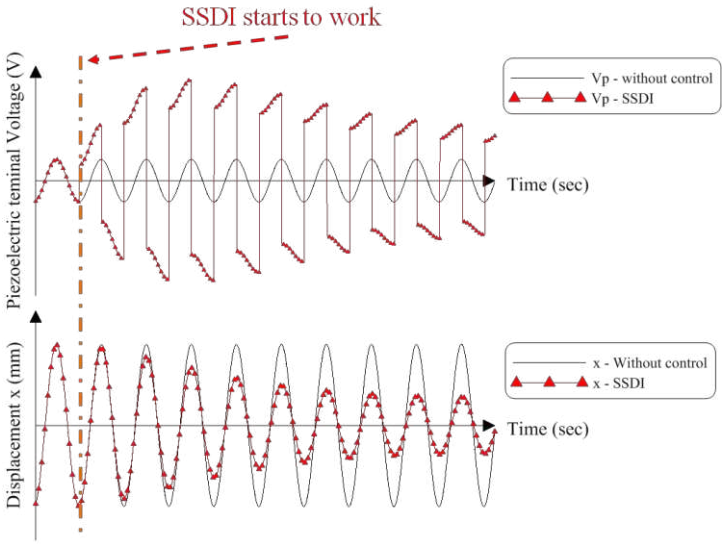

Figure 2-30. Waveforms of the SSDI technique.

The SSDI waveform of the steady state (Figure 2-31(a)) is also can be decomposed

of two waveforms as Figure 2-31(b) and Figure 2-31(c) like SSDS. As the equations derived from the SSDS sub-section, the SSDI switching damping energy can also expressed as (2.47). From the waveform, the behavior of SSDI technique is almost the same as the series-SSHI and the only difference is the voltage of regulated capacitor ($\hat{V}_C$) equals to zero. So according to the equation (8.29) and equation (8.26) and setting the $\hat{V}_C$ equals to zero, the voltage $\hat{V}_P$ and voltage $\hat{V}_P'$ can be obtained as equation (2.49) and equation (2.50). The $V_1(t)$ integrate with the velocity ($\dot{x}$) will turn into zero because they are 90 degree phase lag and the SSDI switching damping energy will only be composed of $V_2(t)$. Finally, the SSDI switching damping energy can be expressed as equation (2.51).

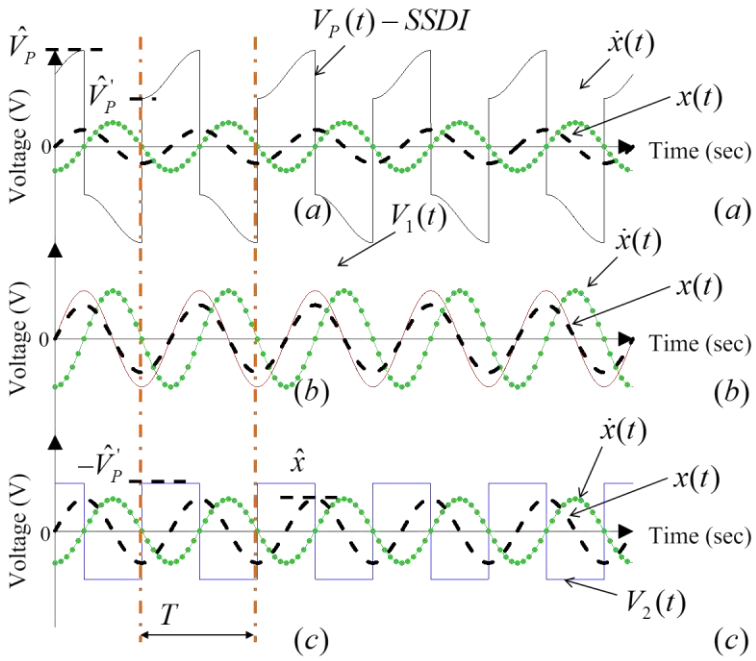

Figure 2-31. Waveforms of (a) SSDI can be decomposed of (b) $V_1(t)$ and (c) $V_2(t)$.

$$\hat{V}_{P-SSDI} = \frac{2\alpha}{C_0(1-q_{LC})}\hat{x} \tag{2.49}$$

$$\hat{V}'_{P-SSDI} = \hat{V}_{P-SSDI} \cdot q_{LC} = \frac{2\alpha}{C_0}\frac{q_{LC}}{(1-q_{LC})}\hat{x} \tag{2.50}$$

$$\begin{aligned} E_{S-SSDI} &= \alpha\int_0^T V_2(t)\dot{x}dt = \alpha\int_0^T \left(\frac{2\alpha}{C_0}\frac{q_{LC}}{(1-q_{LC})}\hat{x}\right)\dot{x}dt \\ \Rightarrow E_{S-SSDI} &= 8\frac{\alpha^2}{C_0}\frac{q_{LC}}{(1-q_{LC})}\hat{x}^2 \end{aligned} \tag{2.51}$$

2.6.3 Discussion of the structural damping circuits

Comparing the switching damping energy of the SSDI with the SSDS, the switching damping energy ratio ($E_{\Delta D}$) can be expressed as equation (2.52). Using different inverting factor, the switching damping energy ratio can be plotted as Figure 2-32. The higher inverting quality factor can make SSDI technique more efficient than SSDS technique but there is a limit of the SSDI. If the SSDI technique is efficient than SSDS, the inverting quality factor needs to be higher than $\frac{1}{3}$ as equation (2.53). In the normal system, the inverting quality factor will be higher than 0.6 and the efficiency of the SSDI can be usually higher than the SSDS around 4 times.

$$E_{\Delta D} = \frac{E_{S-SSDI}}{E_{S-SSDS}} = 2\frac{q_{LC}}{(1-q_{LC})} \tag{2.52}$$

$$E_{\Delta D} > 1 \Rightarrow q_{LC} > \frac{1}{3} \tag{2.53}$$

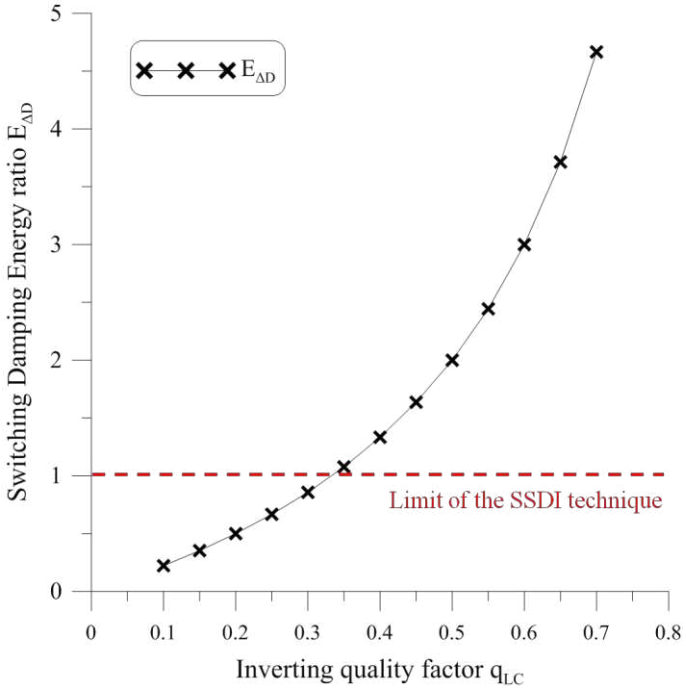

Figure 2-32. Switching damping ratio $E_{\Delta D}$ vs. Inverting quality factor q_{LC}.

2.7 Summary of the interface circuits

In this chapter, a review of several interface circuits in energy harvesting and damping applications is proposed. The basic governing equation, equivalent circuit

model, waveform, optimal load and maxima output power are analyzed and discussed. The output power and transferred energy are compared of each interface circuit. The synchronized switching circuits in energy harvesting are theoretically always better than the standard circuit composed of full-bridge rectifier. In the normal inverting quality factor, the parallel-SSHI and series-SSHI can theoretically increase around 400% power output at optimal load. From the discussion of the work-cycle, the transferred energy of parallel-SSHI and series-SSHI are theoretically increased around 4 times. When the synchronized switching technique is used in the structural damping, the performance of the SSDI is better than the SSDS but there is a limit of the inverting quality factor. In the normal inverting quality factor, the switching damping energy of SSDI is around 4 times than SSDS. Whatever in energy harvesting application or structural damping application, the higher inverting quality factor can lead better performance. But there is a trade-off between inverting quality factor and the cost. The interface circuits proposed will be used in the following chapters to further design and establish the more useful piezoelectric energy harvesting device and piezoelectric structural damping system.

Chapter 3 Tunable Resonant Frequency Power Harvesting Devices

Methodologies of using piezoelectricity to convert mechanical power to electrical power with a cantilever beam excited by external environmental vibration were widely discussed and examined. Operating in resonant mode of the cantilever beam was found to be the most efficient power harvesting method, but in most cases that the resonant frequencies of the cantilever beam is hardly matching with the frequency of external vibration sources, such as mounting on a real world bridge. A cantilever beam based tunable resonant frequency power harvesting device which will shift its resonant frequency to match the external vibrations was developed and verified and will be presented in this chapter. From the networks analysis results, the useful bandwidth can be successfully extended. This system utilizes a variable capacitive load to shift the gain curve of the cantilever beam and a low power microcontroller sampling the external frequency and adjust the capacitive load to match external vibration frequency in real-time. The underlying design thoughts, methods developed, and preliminary experimental results will be presented. Potential applications of this newly developed power harvesting to wireless sensor network will also be detailed.

3.1 Introduction

From the research activities mentioned [11, 15-17, 28-36], researchers are improving the power harvesting devices from all aspects, including mechanics design, electrical signals, best materials, magnetic fields and adaptive power circuit design. In comparison with these technologies, the newly developed technology presented in this chapter derives its innovation from the interaction with the external excitation sources. It is known that the mechanical behavior of the structure is hard to be controlled, and most control technique will consume lots of the energy. In the energy harvesting application, if the energy harvesting device needs to be used in the real application, it is meaningless to control the mechanical behavior by using the external instruments and external energy.

In the view of basic mechanics, when the external force excites one of the natural frequencies of the system, resonant condition are meet and leads to large structure vibrations. If the resonant frequencies of the power harvesting devices coincide with the natural frequencies of the structure it mounted, much higher power output could be expected due to higher gain on the resonant frequencies. However, the natural frequency of the structure which power harvesting devices mounted on, such as bridges, scaffolds etc., may change with time when the structure is under different loading conditions. For

a power harvesting device based on a cantilever-beam structure has onlyconstant resonant frequencies, it will not always be working at the best condition. A high mechanical quality factor cantilever beam can bring larger displacement at resonant frequency and generator more energy, but when the exciting frequency is away from the resonant frequency high mechanical quality factor will cause larger attenuation. Thus, the best solution for this trade-off problem is to design a high mechanical quality factor cantilever beam and the resonant bandwidth of this cantilever beam can be tuned. In a short region bandwidth, the voltage gain of the cantilever beam will not attenuate and the harvesting efficiency can be increased. An innovative real-time resonant frequency tuning system which can tune the resonant frequency to match the natural frequencies drifting of the mounting structure are proposed. The device can always work at best condition during a short frequency range by tuning its resonant frequency to match the external excitation frequency.

The technology proposed in this chapter utilized an ultra-low-power microcontroller on real-time sampling the external excitation frequency which can be combined with the wireless sensor on wireless sensor network(WSN) nodes, so as a more efficient self-powered wireless sensor could be built. Sensor network typically finds its applications in remote or difficulty to access areas, long-lasting batteries and

wireless technologies are the two subsystems mostly used. Power harvesting techniques provide the user with an opportunity to eliminate or at least reduce the frequency of battery replacement, which is particular attractive for long-term applications related to highly dangerous or remote areas. Adopting such techniques to improve the usage time of portable electronics without increasing the pack weight is another area worth noting considering the mobile computing trend in today's information application.

3.2 Theoretical Analysis

In this section, theoretical analysis of a piezoelectric cantilever beam will be conducted and through the simple analysis and the concept of the tunable frequency system would be derived. The piezoelectric cantilever beam bend at 1st mode can be shown as Figure 3-1, when boundary condition is one end fixed and the other end free.

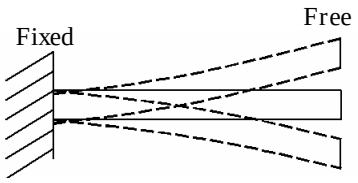

Figure 3-1. Cantilever beam bends at 1st Mode.

According to the theoretical analysis in the chapter 2, if the external electric load is a capacitive load C_L shunt with a resistive load R_L, the equivalent circuit model can further be simplified by reflecting the static capacitor C_0, capacitive load C_L and the load R_L to the primary side of the transformer by times the square of the transformer

turns ratio (force-voltage factor, α) and the simplified equivalent circuit model is shown in Figure 3-2. The C_0' equals to $\alpha^2 C_0$, C_L' equals to $\alpha^2 C_L$, and R_L' equals to $\alpha^2 R_L$ after reflection.

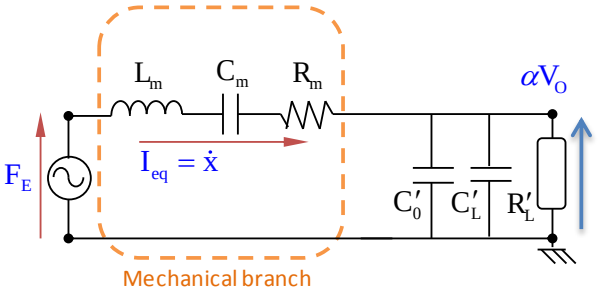

Figure 3-2. Simplified equivalent circuit model.

The equivalent circuit model in Figure 3-2 is a simple serial-parallel loaded resonant network (SPLR), the voltage gain $A_V\left(\left|\frac{\alpha V_0}{F_E}\right|\right)$ represents the force to voltage output gain, and it can be written as equation (3.1).

$$A_V = \left|\frac{\alpha V_o}{F_E}\right| = \left|\frac{R_L' \| 1/\, j\omega C_P}{(R_m + j\omega L_m + 1/\, j\omega C_m) + R_L' \| 1/\, j\omega C_P}\right| \tag{3.1}$$

,where $C_P = \left(C_0' + C_L'\right)$

Equation (3.1) can be further simplified and non-dimensionized with $k = C_P / C_m$,

$\omega_0 = 1/\sqrt{L_m C_m}$, $Q_L = \omega_0' L_m / R_L'$ and $Q_S = \omega_0' L_m / R_m$ as equation (3.2).

$$A_V = \frac{1}{\sqrt{\left[(1+k) - k\left(\frac{\omega}{\omega_0'}\right)^2 + \frac{Q_L}{Q_s}\right]^2 + \left[Q_L\left(\frac{\omega}{\omega_0'} - \frac{\omega_0'}{\omega}\right) + \frac{k}{Q_s}\left(\frac{\omega}{\omega_0'}\right)\right]^2}} \tag{3.2}$$

From equation (3.2), the two resonant frequencies of the RLC oscillator can be obtained. One is the series resonant frequency and the other is the shunting resonant frequency as shown in equation (3.3) and equation (3.4).

$$\omega_s = \frac{1}{\sqrt{L_m C_m}} = \omega_0' \tag{3.3}$$

$$\omega_P = \frac{1}{\sqrt{L_m\left(\frac{C_m C_P}{C_m + C_P}\right)}} = \omega_0'\sqrt{1+\frac{1}{k}} \tag{3.4}$$

For short circuit condition, $C_P = 0$ $(k = 0)$, the circuit becomes a serial loaded resonant network and ω_s is the resonant frequency. When C_P is much larger than C_m (large k), $\omega_P \cong \omega_s$ and the resonant would be closed to ω_s again. For other finite smaller capacitive loading values, the resonant frequency will be shifted between ω_s and ω_P with $C_P = C_0'$ (the open circuit condition). The value of capacitive load C_L'

can then be varied to tune the resonant frequency within this frequency range. The force to voltage output gain versus non-dimensionalized ω/ω_0' is plotted in Figure 3-3 by using $Q_L = 1$, $Q_s = 1000$ and $k = 0, 0.5, 1, 1.5$ and 2. It's obviously to see that the in different k value, the resonant frequency is successfully be shifted and when k value is larger, the voltage gain increases.

From the view of mechanics, the stiffness of the cantilever beam is varied when the electrical loading condition changed. The frequency tuning can be achieved by a simple analog circuit or by sampling the external excitation frequency with a microprocessor, and switch in an adequate capacitive value to tune the resonant frequency matching to the external excitation frequency in a small range. The circuit can be put on the sensor node and control the frequency tuning with the low power microprocessor on the sensor node.

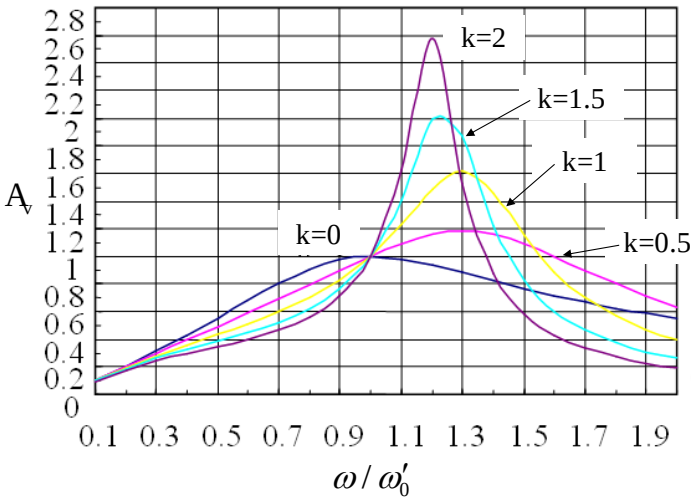

Figure 3-3. A_v versus ω/ω_0' plot.

3.3 Experimental validation and discussion

3.3.1 Real bridge frequency measurement

In this sub-section, we want to know the behavior of the real bridge when the time passes or the loading of the bridge changes. It is obviously that the amounts of the cars go through a bridge will not be the same all day long and the cars may have traffic jams on the bridge, so it means that the loading of the bridge is varying over time. From the structural dynamics perspective, when the loading of the bridge changes, the natural frequency of the bridge will be changed. When the time passes or the bridge encounters to the natural disaster, the bridge will be fatigued and be destroyed and these reason will also cause the natural frequency of the bridge be changed. If a cantilever-beam typed power harvesting device combined with wireless sensor networks is placed on a real bridge to monitor the bridge, the resonant frequency of the cantilever beam will be within narrow band width. When the natural frequency of the bridge changes, the cantilever-beam typed power harvesting device cannot work at the best condition. This result cause the power harvesting device cannot always work matching the resonant frequency of the bridge.

Figure 3-4(a) shows the experimental setup for measuring the vibration signal of the bridge. The accelerometer is placed on the middle of the two bridge piers, because

the middle point is the maximum displacement point and it is the best point to harvesting the vibration energy. Figure 3-4(b) shows how to record the accelerometer data. Through the conditioning, DAQ card and LabVIEW program of the notebook, the measuring data of the accelerometer can be recorded in the notebook and then be analyzed.

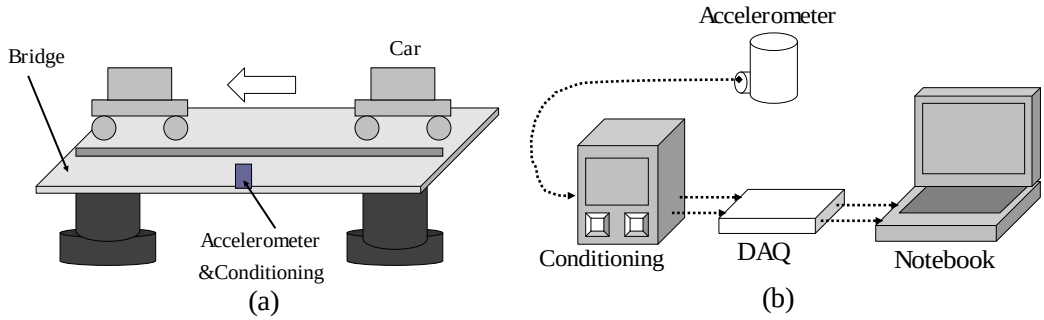

Figure 3-4. (a) Bridge Vibration Measurement (b) Measuring data record setup

Figure 3-5 shows the results of the real bridge vibration measurement. The bridge is Jhonghsing bridge (中興橋) located in Taipei, Taiwan. There are three data sets measured in different time in the Figure 3-5. Each measuring time interval here is 800 sec. During each measuring time interval, the loading of the bridge must be different as different amount of the cars pass the bridge. Because the natural frequency of the bridge must be very low and the frequency range we concern is under 100Hz, the measuring

sampling rate is set to be 5000Hz. From the measuring result, we can obviously see that the three vibration signal are different from each other when the loading is different.

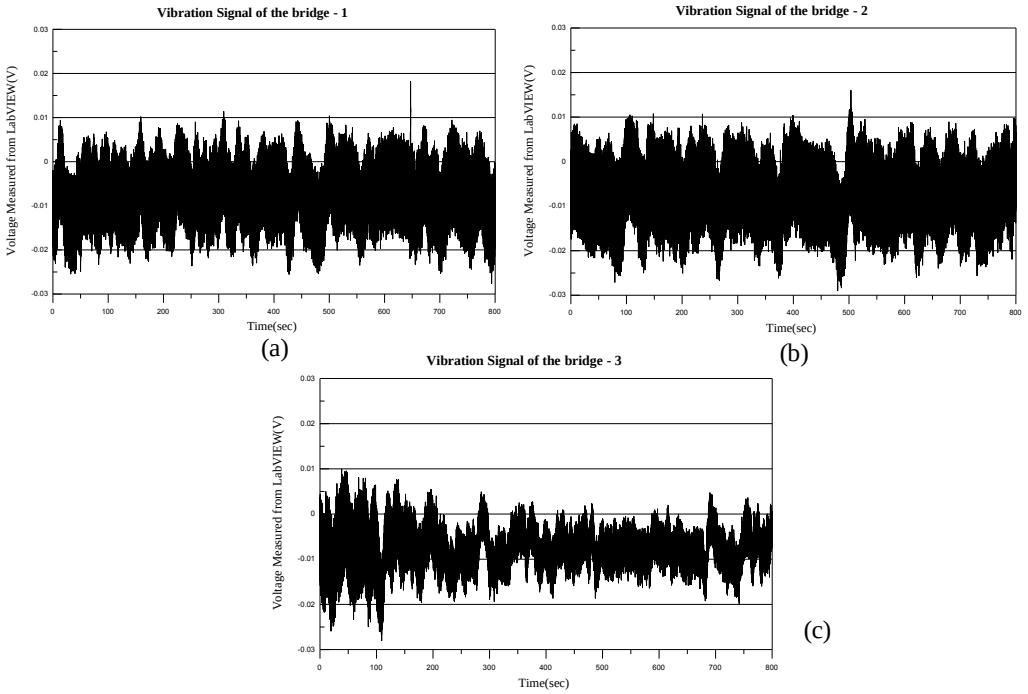

Figure 3-5. Three data sets of vibration measurement results of the bridge.

Then three measuring data sets are taken into Fast Fourier Transformation (FFT), and the FFT results are shown in Figure 3-6. The results are sorted from the frequency range from 65Hz to 85Hz and three FFT results show the resonant frequencies are a little shifting from each other under different loading. The resonant frequency range is around 2.5Hz. If the resonant frequency of the tunable energy harvesting device is designed to match in this 2.5Hz range, it can work better and harvest more energy.

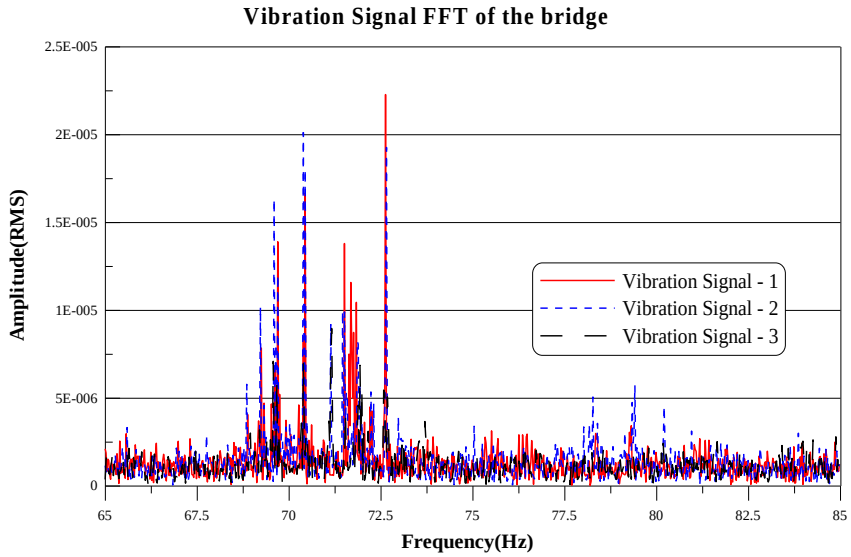

Figure 3-6. FFT of the vibration signals.

3.3.2 Piezoelectric energy harvesting cantilever beam testing

The experimental setup of the piezoelectric energy harvesting cantilever beam is shown in Figure 3-7. The experimental setup is composed of a bimorph piezoelectric clamped at fixed end, a function generator generating the vibration signal, a vibrating shaker generating exciting source and a photonic sensor measuring the displacement. The instruments and model are shown in Table 3-1. The piezoelectric patch used here is bimorph type made by Mide Corporation and the model is QP25W. The dimension and the parameters are shown in

Table 3-2. The bimorph piezoelectric cantilever beam is composed two piezoelectric patches as Figure 3-8 and the two patches can be used separately. This

QP25W bimorph piezoelectric is suitable for power harvesting as its good performance for charging the battery [79].

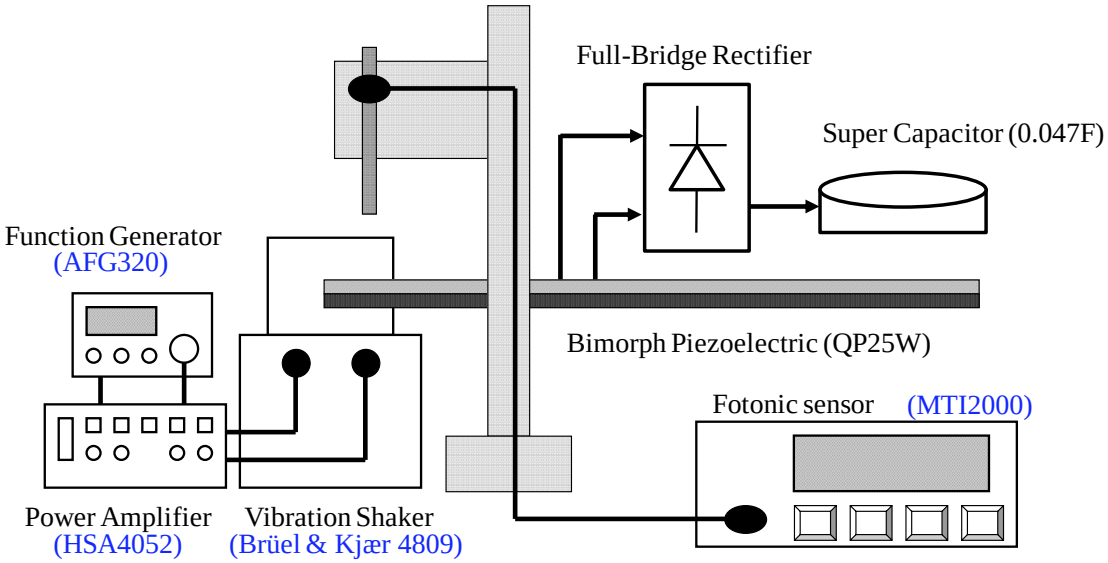

Figure 3-7. Experimental setup of the tunable energy harvesting device.

Table 3-1. Instrument list

Instrument	Company	Model
Function generator	Tektronix	AFG320
Power Amplifier	Brüel & Kjær	4809
Vibration Shaker	NF Corporation	HSA4052
Fotonic Sensor	MTI Instruments Inc.	MTI2000

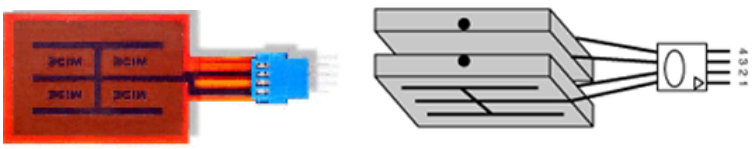

Figure 3-8. Bimorph piezoelectric cantilever (QP25W) from Mide corporation.

Table 3-2. Dimension and parameters of the piezoelectric cantilever beam.

Symbol	Description	Value (unit)
Size	Length×Width×Thickness	2×1.5×0.02 (in^3)
f_{op}	Open circuit resonant frequency	76 Hz
f_{sh}	Short circuit resonant frequency	73.55Hz
k^2	Electromechanical courpling coefficent	0.0677
ζ	Damping ratio	0.054
Q_M	Mechanical quality facotr	9.19
M	Mass	5.1 g
K^E	Equivalent stiffness when all piezoelectric element is in short circuit	1163.2 N/m
K^D	Equivalent stiffness when all piezoelectric element is in open circuit	1089.4 N/m
D	Damping coefficient	0.265 N/m/s
α	Force-voltage facotr	0.35 N/V
C_0	Clamped capacitance of	330nF

The piezoelectric energy harvesting device is tested under different excitations at short-circuit resonance and the results are shown in Figure 3-9. Figure 3-9(a) shows the capacitor's voltage versus charging time curves when the device charges to a 0.047F super capacitor under different excitations. When the exciting source increases, the charging time decreases. The total charging energy can be calculated by using $(1/2)CV^2$, whereC is the capacitance value and V is the terminal voltage of the capacitor. And the average harvesting power can be calculated by dividing the total charging

energy by the charging time when the voltage reaches the target value. The target voltage here is set at 4V for calculating the average power. Figure 3-9(b) shows the results of the power output of piezoelectric patches under different excitations. When the displacement is under 0.08mm, the relation between power output and displacement is almost a linear line. However, when excitation goes too large the power output won't increase linearly. This result shows that the excitation should be limited in the elastic region or the device may be broken. In order to keep the piezoelectric cantilever beam working in the linear region, the acceleration of the following testing is set to 0.5m/s^2 (displacement = 0.017mm).

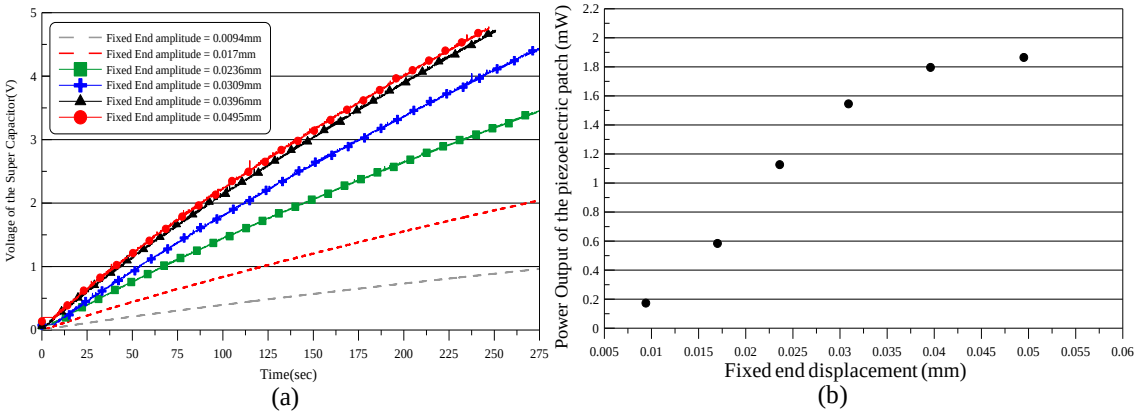

(a) (b)

Figure 3-9. Piezoelectric energy harvesting cantilever beam testing results. (a) Charging time curve (b) Output power under different excitation.

3.3.3 Network Analysis

In order to demonstrate the function of the tunable frequency system, the shifting resonant frequency effect will first be verified through SRS Network Signal Analyzer

SR780, and the experimental setup is shown in Figure 3-10. The microprocessor is used to choose different capacitor load according to the exciting frequency. The upper patch of the bimorph piezoelectric configuration is used for the frequency tuning purpose through the microprocessor to sample the exciting frequency and connected to different capacitors loadings. According to the theory when the capacitor loadings are changed, the resonant frequency of the piezoelectric cantilever beam can be tuned to match the exciting frequency. The lower piezoelectric patch is used to harvest energy and regulated to a DC voltage by a full-bridge rectifier to charge a 0.047F super capacitor. The super capacitor can then provide the extra energy for wireless sensor network nodes and extend the battery life time.

The testing results are shown in Figure 3-11. The short-circuit condition (star points) and the open-circuit condition (triangle points) are two extreme conditions and the resonant frequencies are 73.5Hz and 76Hz respectively. Around 2.5Hz frequency range is the tunable bandwidth on this system. The resonant frequency of the system can be changing within this 2.5Hz range by switching in different capacitive loads as Figure 3-11 shown. This tunable bandwidth and resonant frequency almost fit the measuring results from the real bridge and can be used in the real application. When the tuning patch of the bimorph piezoelectric is shunted to the 0.16uF and 0.078uF capacitor, the

gain curve can be tuned between the two extreme conditions and through proper switching control the gain curve of the tunable frequency system can be extended and smoothly changed between short-circuit and open-circuit condition as the experimental results (round points). Comparing the tunable system curve with short-circuit, open-circuit and other single capacitive loads, the resonant bandwidth is obviously wider and the harvesting efficiency can be effectively increased.

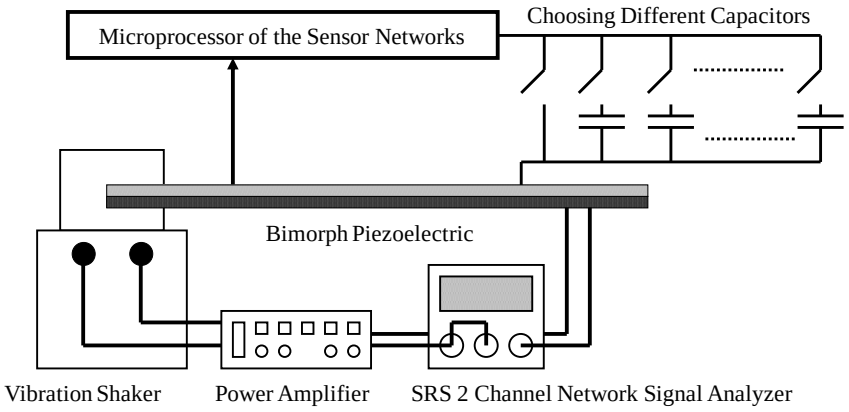

Figure 3-10. Network analysis of the tunable energy harvesting device.

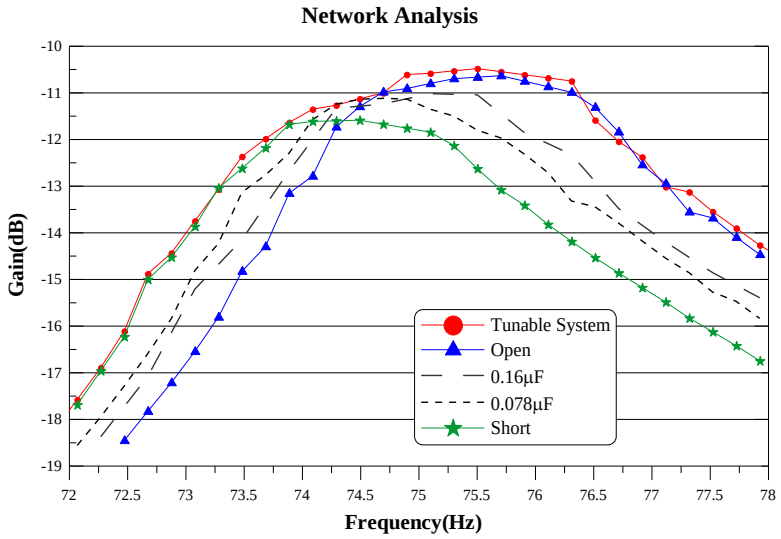

Figure 3-11. Experimental results of the network analysis.

3.3.4 Charging the Capacitor with Chirping and Random Frequency Excitations

3.3.4.1 Frequencies slightly away from the resonance test

In order to evaluate the difference of harvesting efficiency when the piezoelectric energy harvesting cantilever beam excited under slightly different frequencies around the resonance, a 0.047F super capacitor is charged by the power harvesting device under short-circuit condition (resonant frequency = 73.5Hz) at acceleration=0.5m/s^2. The testing results are shown in Figure 3-12.

We can see that the super capacitor reaches the target voltage 4V in shortest time when excited at the resonant frequency (73.5Hz). When the system is excited at 72.5Hz, 1Hz away from the resonance, the charging time spends more than 50 seconds to reach the target voltage. And when the system is excited at 71.5Hz, 2Hz away from the resonance, the charging time spent are longer than 200 seconds.

When piezoelectric energy harvesting cantilever beam is excited at resonant frequency (73.5Hz), its average harvesting power output is around 0.859mW. When the beam is excited 1Hz away from the resonant frequency (72.5Hz), its average harvesting power is around 0.778mW and 2Hz away from the resonant frequency (73.5Hz), its average harvesting power is around 0.578mW. From average power results, if the resonant frequency can be tuned for 1Hz, the average harvesting power will increase

10.4%, and if the system can be tuned for 2Hz , the average harvesting power will increases 48.6%. When 3Hz or more away from the resonant frequency, the voltage of the super capacitor is hardly to reach to 4V, even cannot reach the target voltage. This results show that in a quality factor system, to match excitation frequencies with the resonance is very important.

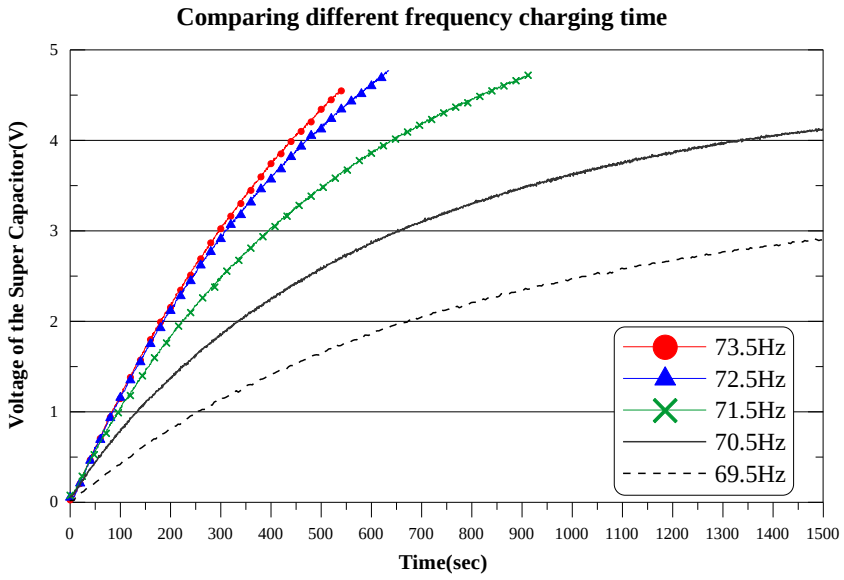

Figure 3-12. Charging time of external excitations at different frequency.

3.3.4.2 Chirping and random frequencies excitation testing

The testing of the above sub-section excites the energy harvesting system at the single frequency under short-circuit condition to show how the tunable technique use to increase the energy harvesting efficiency. The real-time frequency tuning energy

harvesting device is then tested in chirping frequency and random frequency excitation under different frequency range. The exciting signal source is provided by the LabVIEW program to generate the chirping frequency and random frequency with a DAQ card (USB 6259) and drive the vibration shaker through a power amplifier. The testing chirping and random frequency ranges are both from the wider frequency range to the narrower frequency range. There are four testing ranges: 1.Bandwidth=40Hz (55~95Hz), 2. Bandwidth=20Hz (65~85Hz), 3. Bandwidth=10Hz (70~80Hz) and 4. Bandwidth=4Hz (72~76Hz). The tunable energy harvesting device still charges to a 0.047F super capacitor and the charging voltage curve versus time of the four testing ranges are shown in Figure 3-13 to Figure 3-16, the testing curves (a) are all chirping testing and (b) are all random testing.

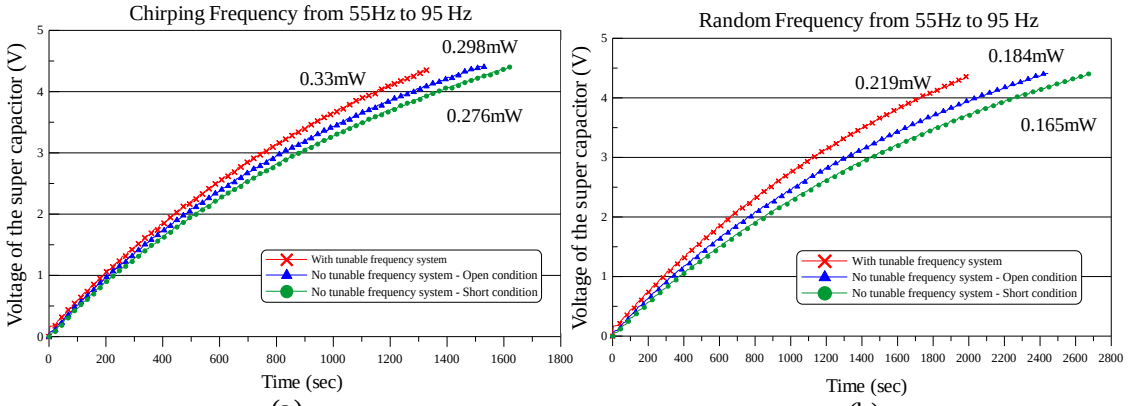

Figure 3-13. Chirping (a) & Random frequency (b) from 55Hz to 95Hz.

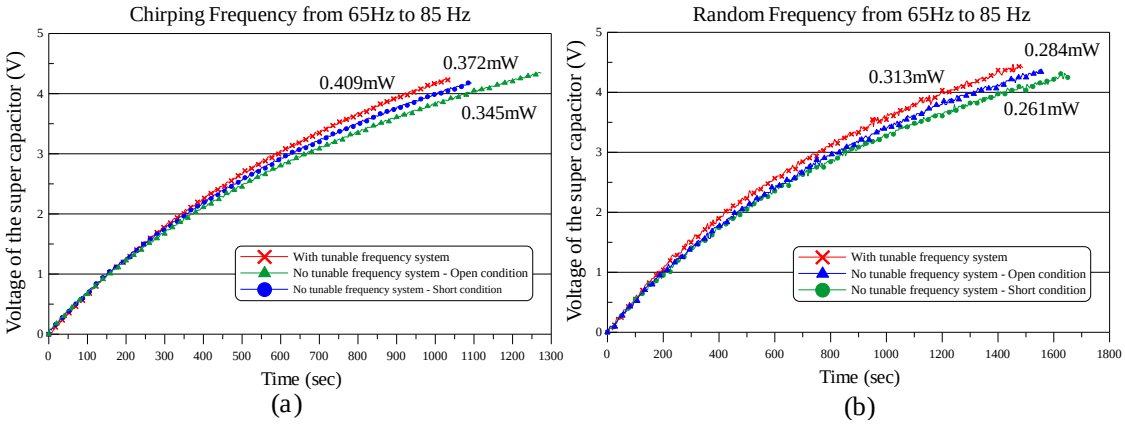

Figure 3-14. Chirping (a) & Random frequency (b) from 65Hz to 85Hz.

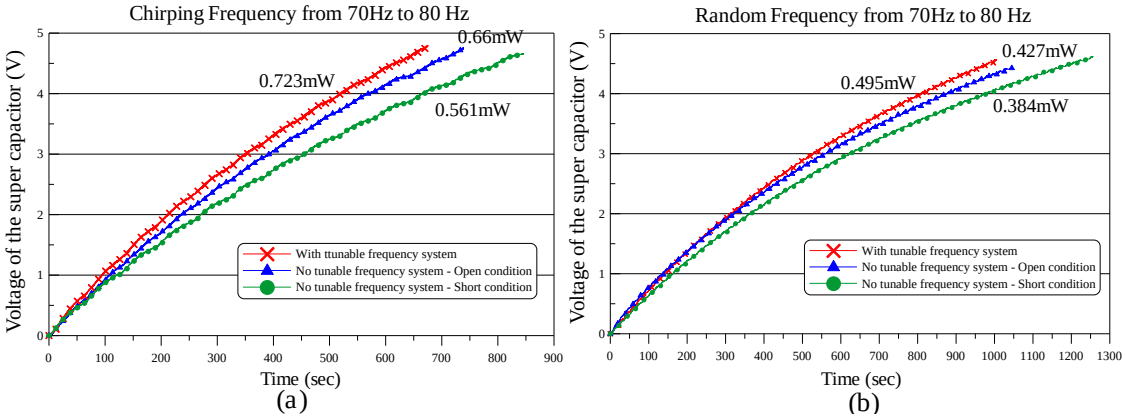

Figure 3-15. Chirping (a) & Random frequency (b) from 70Hz to 80Hz.

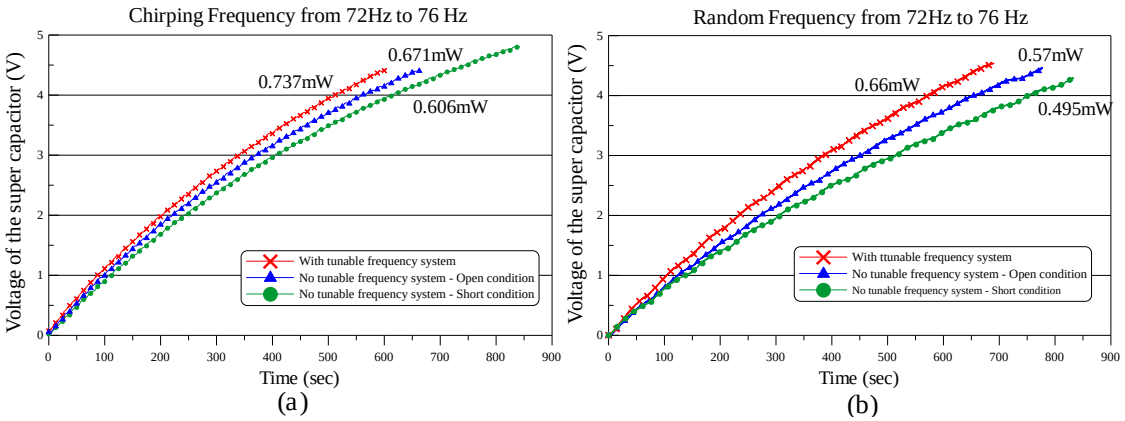

Figure 3-16. Chirping (a) & Random frequency (b) from 72Hz to 76Hz.

These experimental results can verify our tunable energy harvesting system. Table 3-3 and Table 3-4 summarize the power output of the chirping and random frequency testing results. The increased power is calculated by using the short-circuit condition to be the reference and the increased power is calculated using equation (3.5).

Table 3-3. Chirping frequency testing results.

	Average Power Output (mW)			
Frequency range	Short-Circuit	Open-circuit	Tunable System	Increased power (%)
55 to 95 Hz	0.276	0.298	0.33	19.57
65 to 85 Hz	0.345	0.372	0.409	18.55
70 to 80 Hz	0.561	0.66	0.723	28.88
72 to 76Hz	0.606	0.671	0.737	21.62

Table 3-4. Random frequency testing results.

	Average Power Output (mW)			
Frequency range	Short-Circuit	Open-circuit	Tunable System	Increased power (%)
55 to 95 Hz	0.165	0.184	0.219	32.73
65 to 85 Hz	0.261	0.284	0.313	19.92
70 to 80 Hz	0.384	0.427	0.495	28.91
72 to 76Hz	0.495	0.57	0.66	33.33

$$\text{Increased power} = \frac{\text{Tunable system power output}}{\text{Short-circuit power output}} \tag{3.5}$$

In the chirping frequency testing results, four testing frequency ranges can all reach

mW level power output and the average power output is around 0.3mW, 0.38mW, 0.65mW and 0.67mW for each range. The tunable resonant frequency energy harvesting device can increase the power output around 19.57%, 18.55%, 28.88% and 21.62% for each frequency range. The maxima increased power is 28.88% and occurs when the chirping testing frequency range is 70 to 80Hz. The charging time can be shorted around 170 seconds.

In the random frequency testing results, the average power is around 0.19mW, 0.29mW, 0.44mW and 0.58mW for each range. The tunable resonant frequency energy harvesting device can increase the power output around 32.73%, 19.92%, 28.91% and 33.33% for each frequency range. The maxima increased power is 33.33% and occurs when the chirping testing frequency range is 72 to 76Hz. The charging time can be shorted around 160 seconds.

In the two testing conditions, the both average power increases when the testing range narrows. Comparing the chirping frequency testing results with the random frequency testing results, the output power of the chirping testing is higher than random testing. However, the tunable energy harvesting system used in random frequency testing can increase power output more than in chirping testing case. That's because when exciting signal is random frequency and if the exciting frequency is changed

instantaneously from the resonance to non-resonance, the piezoelectric voltage will decrease immediately to induce the full-bridge rectifier turning into open-circuit condition and the charging current discontinued Because the charging current discontinued, the charge time will increase. The tunable frequency energy harvesting system is very suitable to be used in the random exciting source and the random exciting source is more closed to the vibration sources in real world. The tunable technique make the resonance of the system changed with the exciting frequency and this wide resonant bandwidth keeps the charging current continuous and effectively increase the output power. This real-time resonant frequency tuning system shows significant improvement on average harvesting power output.

3.3.5 Implement the tunable frequency power harvesting function on a Wireless sensor network transceiver module

The real-time frequency tuning capability can be achieved by integrating with a wireless sensor with the low-power microcontroller on a wireless sensor to sample the external excitation frequency and changing the loading capacitor to tune the resonant frequency of the cantilever beam. Figure 3-17 show a wireless sensor transceiver module which uses an integrated Chipcon CC1010 microcontroller with built-in wireless transceiver circuit and analog-to-digital converters for sensor signal interfacing.

The microcontroller was programmed to control the frequency tuning harvesting device. It has to be noted that general microcontroller will consume several tens mW power which is much higher than the energy harvesting devices can generate. However, modern low-power microprocessor can operate in μW level. It would be worthy to pay the price of μW power consumption in operating microcontroller to tune the frequency and gain much higher harvesting power generation in mW range.

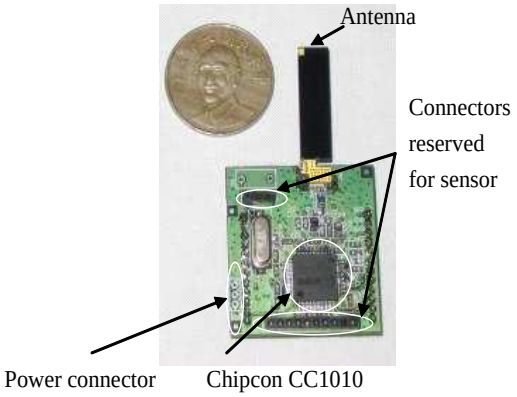

Figure 3-17. The wireless sensor transceiver module using Chipcon CC1010 integrated microprocessor.

Figure 3-18 shows the circuit schematic of the wireless sensor network (WSN) transceiver module implemented the tunable frequency function for piezoelectric energy harvester and Figure 3-19 shows the photos. The energy harvested from the piezoelectric cantilever beam is stored in the super capacitor C1 through a full-bridge rectifier. Here, we still use a battery to supply the energy to the WSN module and the

piezoelectric energy harvesting device provide the extra energy to extend the lifetime of the battery by proper switching control.

Figure 3-20 shows the schematic diagram of the switching control for supplying energy to the WSN transceiver module. The voltage of the capacitor C1 and the battery's voltage of the WSN transceiver module are compared by a Schmitt trigger circuit which is composed of a TLV3494 voltage comparator. When the C1's voltage is charged higher than the battery's voltage, the analog switch (TS5A4596) will switch the C1' terminal to connect to the WSN module and supply power to the WSN transceiver module. The switching signal will also be sent to the WSN transceiver module and the triggers the transmitting procedure. When the WSN transceiver module started transmission, the C1's voltage will drop immediately and the switching control will switch the power supply back to the battery. And then the C1 will be charged by piezoelectric energy harvesting device until the voltage is higher the target level. The regulator (TLV70230) regulates the voltage of the super capacitor to provide a stable voltage. In this circuit, Schmitt trigger plays an important role to generator the hysteresis. The hysteresis can make the system more stable, because when the voltage of the capacitor decreases, the power switching control will not switch the circuit to the battery supply mode immediately.

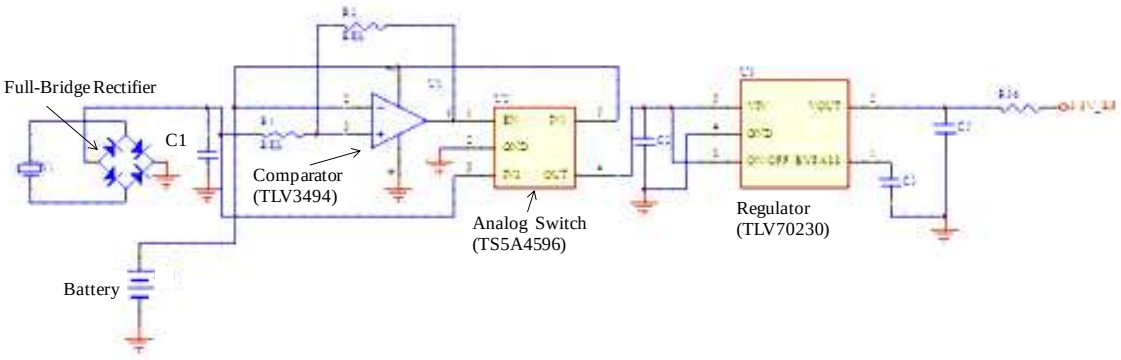

Figure 3-18. Electric circuit for the wireless sensor network combined with piezoelectric energy harvesting system.

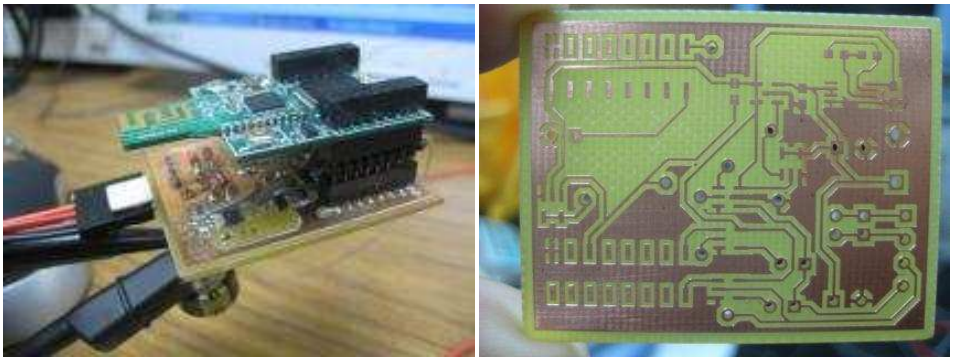

Figure 3-19. Electric circuit photos.

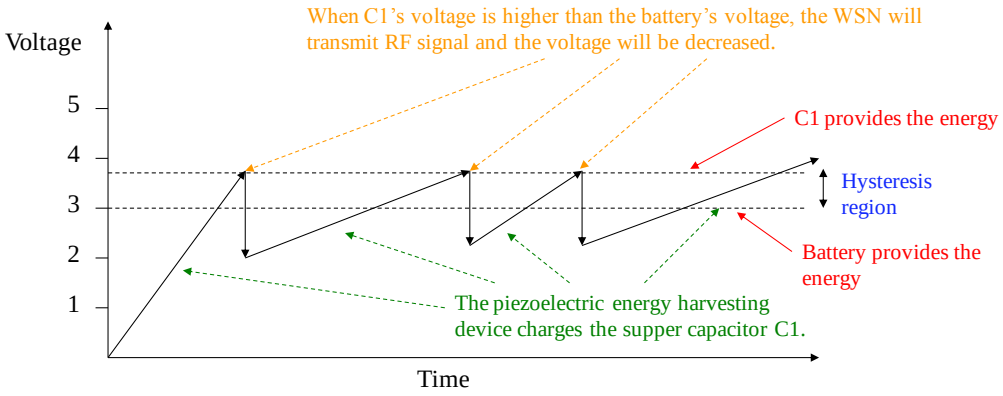

Figure 3-20. Schematic diagram of the switching control for supplying to the WSN node.

Figure 3-21 shows experimental result of the battery, energy harvester switching and the transceiver transmission scheme. In Figure 3-21, left half part shows the module tries to register itself in the registering interval and right half part shows the communication behaviors after it is successfully registered.. If in this registering time interval, switching control switches the system immediately to the piezoelectric energy harvester to supply power, the system will go back to the battery supply mode just as shown in left half part. That's because the piezoelectric energy harvester cannot provide the enough energy for the module working in the registering interval. The switching control will switch the power supply mode back and forth between battery supply and energy harvester. After all the sensor nodes have already registered, the sensor node can be arranged by the local control center to sleep in idle mode or to transmit the RF signal in active mode. When sensor node works in idle mode, the battery provides the system energy and in this time interval the piezoelectric energy harvester will harvest the ambient vibration energy. When the voltage is charged over around 2.3V (set by comparator), the switching control will switch the system to the piezoelectric supply mode to provide energy and sensor node will be in the active mode to transmits the RF signal. After sensor node transmitting the RF signal, the voltage drops down and the system will go back to the battery supply mode. Under this switching scheme, the

sensor network node can work longer through combining with piezoelectric energy harvesters and batteries.

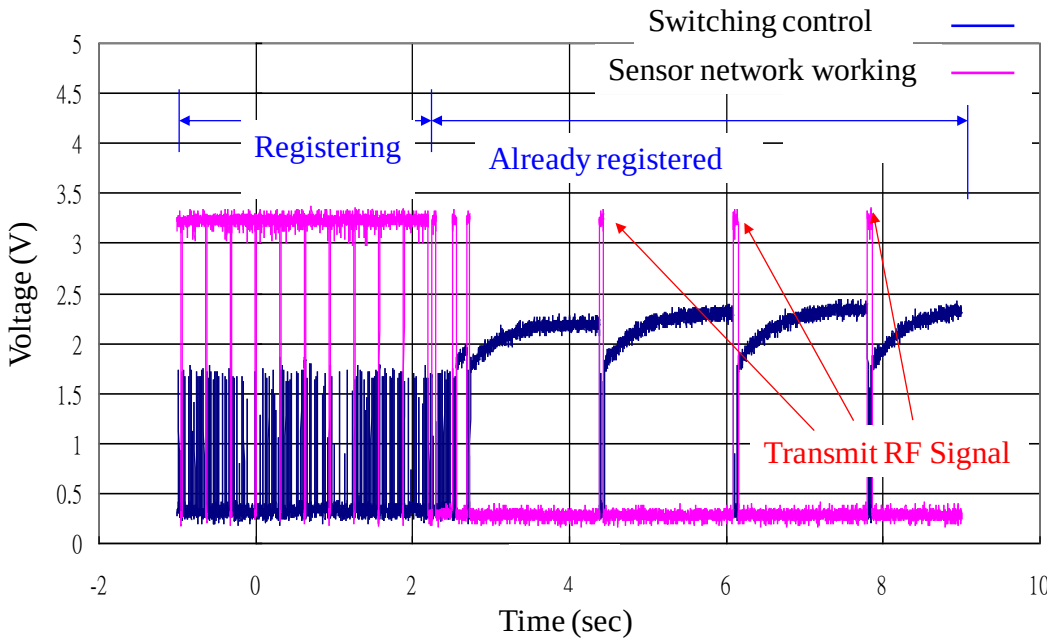

Figure 3-21. Experimental result of battery switching and the transceiver module transmission scheme.

3.4. Conclusion

In this chapter, we present the theoretical analysis and experimental results of the tunable resonant frequency system on a piezoelectric energy harvesting cantilever beam device. The real-time resonant frequency tuning system is further demonstrated by using a microcontroller on a wireless sensor in sensor networks. The tunable frequency technique can extend the resonant frequency range around 2.5Hz and increase the

average harvesting power output almost 30% when under chirping and random frequency excitation testing. This significant power improvement can be expected due to the nature of high mechanical quality factor. From the final experiments, this tunable frequency system can be successfully combined with the wireless sensor network to transmit the RF signal. By integrating the tunable resonant frequency harvesting device with wireless sensor network system, a more powerful self-powered wireless sensor could be built and the battery lifetime can be effectively extended.

Chapter 4 A self-powered switching circuit for piezoelectric energy harvesting with velocity control

In this chapter, a self-powered piezoelectric energy harvesting device is proposed based on the velocity control synchronized switching harvesting on inductor technique (V-SSHI). In chapter 3, in order to use the tunable technique in the real applications, a WSN module is necessary to be used to get the exciting frequency and change the electrical load. To further improve the power output, synchronized switching techniques is proved to be effective on enhance the overall power output. To simplify to overall system design the main focus in this chapter is to realize the synchronized switching technique to be a self-powered system.

Comparing to the standard full-bridge rectifier technique, the synchronized switching harvesting on inductor (SSHI) technique can highly improve harvesting efficiency. However, in real applications when the energy harvesting device is associated with wireless sensor network (WSN) nodes, the SSHI technique needs to be implemented and requires to be self-powered for a reasonable and neat design. The conventional technique to implement self-powered SSHI is to use bipolar transistors and diode as voltage peak detector. In this chapter, a new self-powered design is proposed, using velocity control to switch the MOSFETs more accurately than in the conventional

technique. The concept of the design and the theoretical analysis are presented in detail and experimental results are used to examine to concept of the design.

4.1 Introduction

Nowadays with improvement and rapid growth of low-power electronics, it is possible to supply portable devices such as mobile phone, MP3 player, wireless sensors and human or animal detecting devices, with harvest energy from ambient. Among these low-power devices, wire-less sensor network (WSN) is one of the most important and valuable applications which is highly investigated. Wireless sensor networks can be used to monitor the health of structures, environment, wild animals, tire pressure of running cars, etc. In most of WSN applications, the devices are far from the power line or the devices need to be embedded into the structure to monitor. So, it is hard to use power line to transmit energy to device; battery is the only conventional solution. However, there are lots of disadvantages with using batteries. The major problem is the lifetime: using a 3 V battery a WSN module can only be operated for 1 or 2 years. The batteries cannot be a permanent energy supply for a WSN module. A WSN module with self-powered system can be operated for a longer time without replacing the battery. Harvesting the ambient energy close to the sensor nodes of the WSN is the most likely

and suitable solution to extend the its lifetime [21-25, 80-84].

As mentioned in the chapter 1 and chapter 2, the Synchronized Switch Harvesting on Inductor (SSHI) technique is a very successful and efficient technique to boost the output power from piezoelectric [32, 33, 46, 85]. This approach is derived from a semi-passive damping technique: Synchronized Switch Damping on Inductor (SSDI) [67, 68]. The SSHI technique consists in adding up a nonlinear switching. This nonlinear process increases the output voltage of the piezoelectric elements that increase the output power. The switching device is triggered at the zero crossing of velocity. In order to realize the synchronized switching technique in real applications without external power source to supply the system, many researches present self-powered supply system for piezoelectric energy harvesting devices [23, 37, 53, 54]. The design concept of self-powered system proposed by Lallart and Guyomar [53] is shown in Figure 4-1. This conventional self-powered system works by using a peak voltage detector to control the switching time for SSHI technique. However, the energy supplying to the peak detector and the switching control is drawn from the piezoelectric device. The energy losses in the circuit can be accurately controlled by circuit design; the larger excitation levels leading to relatively smaller losses. As the conventional self-powered system uses peak detector, there is always a phase lag between the peak

voltage and the actual switching time. Moreover, the phase lag for large excitation level is less than for a small one [54].

In this chapter, we present a new self-powered piezoelectric energy harvesting system using velocity control SSHI technique, called "V-SSHI". The schematic design concept of self-powered velocity control SSHI is shown in Figure 4-2. The SSHI used herein is in series type (inductor and switch are in series with piezoelectric patch). Comparing to the conventional design concept, the piezoelectric material is separated into three parts. The main part is dedicated to harvest ambient vibration energy. The second small part is designed to supply energy for switching MOSFET and the last small part is designed for velocity control and for switching on the optimal time. There are two major advantages of this new technique: (1) theoretically, there is no phase lag by using velocity control signal to determine the switching time; (2) the supply energy for the switching driver can be designed and optimized by the size of the piezoelectric material.

The energy flow chart of the conventional self-powered technique and the self-powered V-SSHI technique is shown in Figure 4-3. There is a common path for the main stream of energy and for the supply of the self-switching system. In the V-SSHI technique, they are three energy paths. The energy supplying the self-switching system

and the velocity control patches can be designed optimally. The theoretical analysis and modeling of the self-powered V-SSHI is presented in detail in section 4.2. The experimental results comparing standard DC approach, conventional self-switched technique and V-SSHI technique are presented in section 4.3. The experimental results show higher output power of the V-SSHI technique over conventional technique.

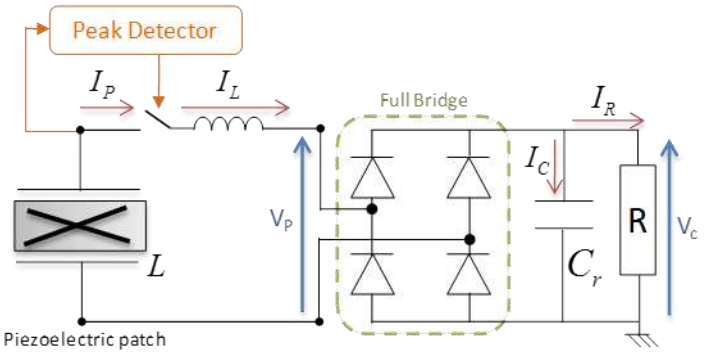

Figure 4-1. Schematic design concept of conventional self-switched system.

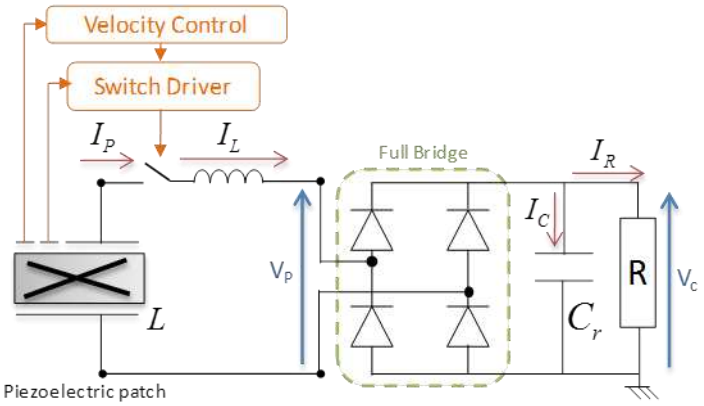

Figure 4-2. Schematic design concept of velocity control SSHI self-switched system.

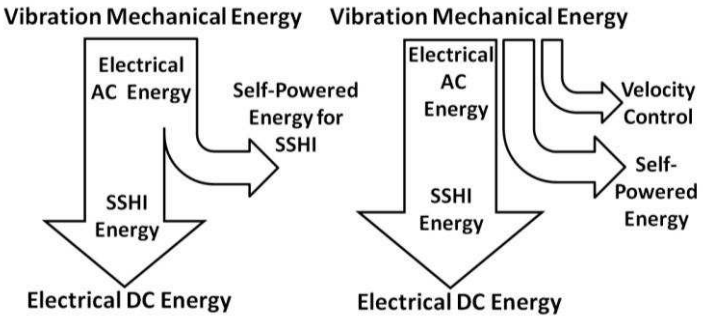

Figure 4-3. Energy flow chart (a) Conventional self-powered technique (b) Self-powered V-SSHI technique.

4.2 Theoretical Analysis of the self-powered V-SSHI technique

4.2.1 Standard DC technique

Before talking about the models of the V-SSHI technique, the standard DC technique is proposed to be a reference. The schematic diagram of piezoelectric energy harvesting transducer with full bridge rectifier connected to a resistor is shown in Figure 4-4(a). Figure 4-4(b) shows also the key waveforms of the standard DC approach. When the absolute voltage value of the piezoelectric patch V_P is less than voltage V_C, the diode bridge is in open-circuit. The diodes conduct and piezo-patches charge the load only when V_P reaches load voltage V_C. The detail theoretical analysis is already derived and discussed in the chapter 2. Because in the next sub-suction, the theoretical and experimental results of the standard DC approach will be shown to compared with V-SSHI, here the voltage crossing the resistor (V_C) and output power (P) can be

expressed as equation (4.1) and equation (4.2)

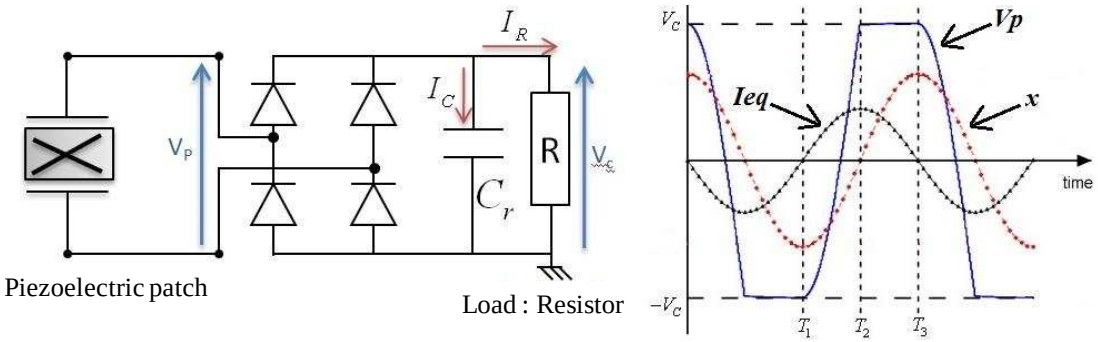

(a) (b)

Figure 4-4. (a) The schematic diagram of the Standard DC approach and (b) waveforms.

$$V_C = \frac{2\alpha R}{\left(2RC_0\omega_0 + \pi\right)} \frac{\hat{F}_E}{D} \tag{4.1}$$

$$P = \frac{V_C^2}{R} = \frac{4\alpha^2 R}{\left(2RC_0\omega_0 + \pi\right)^2} \frac{\hat{F}_E^2}{D^2} \tag{4.2}$$

4.2.2 Self-powered V-SSHI technique

According to the self-powered V-SSHI concept presented in Figure 4-2, the model can be easily separated into three parts. The details are presented hereunder.

4.2.2.1 Main patch for SSHI

The main patch concerned with our new concept is designed to act like a classic

SSHI technique. The schematic diagram of a SSHI technique is shown in Figure 4-5. The fundamental concept of SSHI is to use an inductor L and achieving a LC_0 resonance between piezo-patch and L. Through LC_0 resonance and switches to confine the current flow, more power can be harvested from the piezo-patch. Assuming the structure is excited at the mechanical resonance frequency, the excitation source can be modeled as a current source Ieq. Figure 4-6 shows the waveform of series-SSHI including voltage across piezoelectric V_P , current source Ieq and displacement x. The detail equations are already derived and discussed in the chapter 2. The voltage crossing the load resistor (V_C) and power output (P) can be expressed as equation (4.3) and equation (4.4). The theoretical results and experimental results will be shown, calculated and compared in the next sub-section.

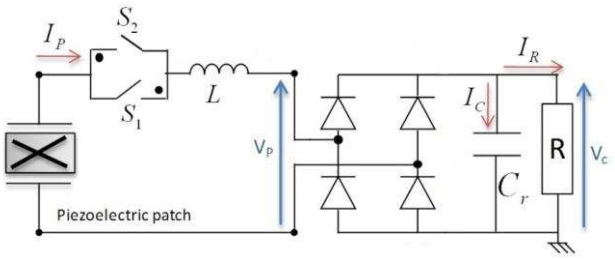

Figure 4-5. Schematic diagram of SSHI piezoelectric energy harvesting device with full bridge rectifier to a resistor load.

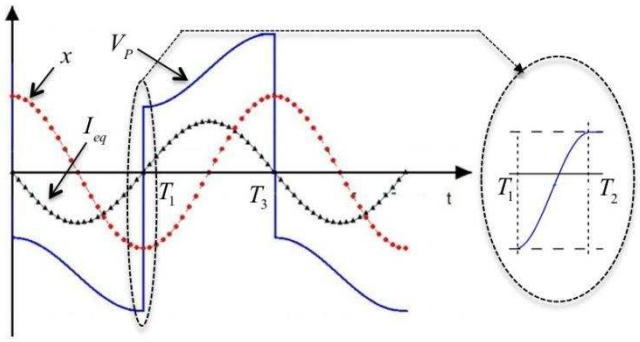

Figure 4-6. Waveform of the SSHI piezoelectric energy harvesting device.

$$\hat{V}_C = \frac{2\alpha R\left(1+e^{\frac{-\pi}{2Q_I}}\right)}{2R\omega_0 C_0\left(1+e^{\frac{-\pi}{2Q_I}}\right)+\pi\left(1-e^{\frac{-\pi}{2Q_I}}\right)}\omega_0\hat{x} \tag{4.3}$$

$$P = \frac{\hat{V}_C^2}{R} = \frac{4\alpha^2 R\left(1+e^{\frac{-\pi}{2Q_I}}\right)^2}{\left[2R\omega_0 C_0\left(1+e^{\frac{-\pi}{2Q_I}}\right)+\pi\left(1-e^{\frac{-\pi}{2Q_I}}\right)\right]^2}\omega_0^2\hat{x}^2 \tag{4.4}$$

4.2.2.2 Auxiliary patch for supplying comparator

The second piezoelectric patch is designed to create two stable supply voltages $+V_{CC}$ and $-V_{CC}$ to supply energy to a comparator and make V-SSHI self-powered and self-switched. The velocity control input signal of the comparator is discussed in next part and the output signal of the comparator drives the two switches (NMOS and PMOS

pair). The equivalent circuit of the supplying circuit is depicted Figure 4-7. The two diodes D_A and D_B rectify the positive and negative current flow, Cr regulates the voltage between $+V_{CC}$ and $-V_{CC}$, C_P regulates the voltage between $+V_{CC}$ to GND and C_N regulates the voltage between $-V_{CC}$ to GND. The voltage V_{CC} can be obtained by integrating from the interval T_1 to T_3 as equation (4.5) and the output power can be represented by V_{CC}^2 / R_{eq} as equation (4.6). Resistor R_{eq} is the equivalent load between $+V_{CC}$ and $-V_{CC}$.

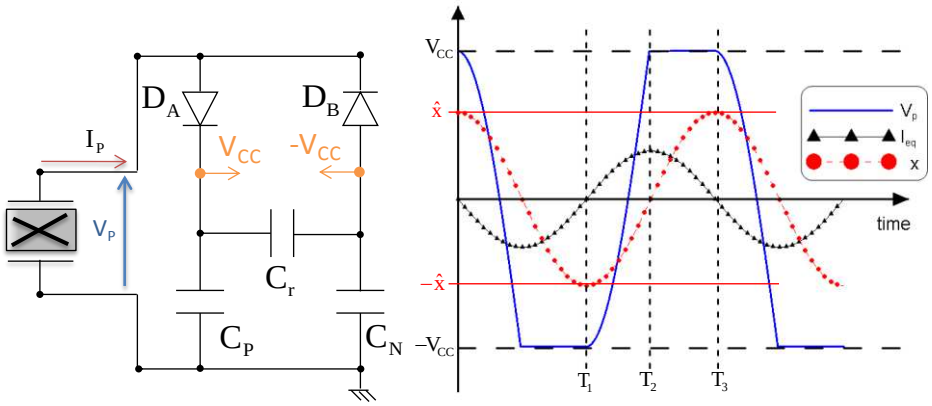

(a) (b)

Figure 4-7. (a) The equivalent circuit diagram of the supplying circuit. (b) Waveform of the supplying circuit.

$$V_{CC} = \frac{\alpha R_{eq}}{(C_0 R_{eq} \omega_0 + \pi)} \frac{\hat{F}_E}{D} \tag{4.5}$$

$$P = \frac{V_{CC}^2}{R_{eq}} = \frac{\alpha^2 R_{eq}^2}{\left(C_0 R_{eq}\omega_0 + \pi\right)^2} \frac{\hat{F}_E^{\,2}}{D^2} \tag{4.6}$$

4.2.2.3 Sensor patch for velocity control

The third patch is designed for generating the velocity control signal. The equivalent circuit is shown in Figure 4-8(a). A low value resistor R_C is connected in parallel with the patch to sense the mechanical current Ieq. A passive low-pass filter is used to reduce the high frequency noise. When SSHI works, the high frequency noise of the velocity signal is very large, so it is impossible to apply directly voltage V_P to comparator and the high frequency noise will make the comparator output unstable during the switching interval. The current sensing resistor used herein must be small enough to avoid the effect of the piezoelectric capacitance. The low-pass filter should be carefully designed to guarantee there is no phase lag for the considered frequency. The key waveforms are also shown in Figure 4-8(b). The blue line V_P is the open-circuit waveform of the piezoelectric patch and the red line V_S is the velocity control signal which is in phase with Ieq. There is 90 degree phase lag inherently between V_S and V_P . When the circuit switches by velocity control, the switching time can be accurate; the current is always in phase with voltage when SSHI works. The power output from

piezoelectric can be always positive.

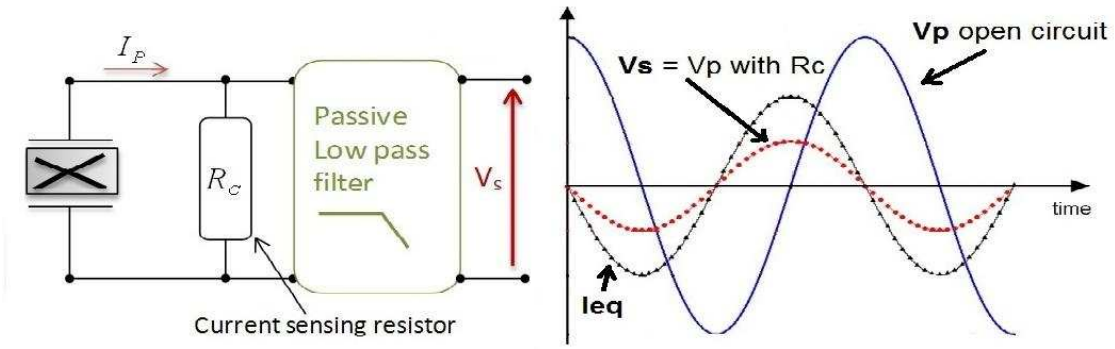

(a) (b)

Figure 4-8. (a) The equivalent circuit diagram of the sensor patch (b) Waveforms.

4.3. Experimental results and discussion

4.3.1 Experimental setup

The experimental structure under testing is a cantilever steel beam. Three 31-type PZT-QA piezoelectric ceramic patches provide by the company ELECERAM were bonded on the beam. Table 4-1 gives the dimensions of the beam and the patches. Figure 4-9 shows the experimental setup and the self-powered V-SSHI circuit diagram. Figure 4-10 shows a picture of the experimental setup. In the experimental setup, the SSHI circuit part is a little bit different from the one of Figure 4-6, but it works identically. The four diodes act like a full bridge rectifier to confine the current flow and the inductor is in series with P_1 pathch.

The cantilever beam is excited by a vibration shaker (LDS-V406). Three piezoelectric patches (P_1 to P_3) are bounded close to the fixed end. An accelerometer (PCB-353B03) is situated at the fixed end to measure acceleration; a laser vibrometer (LK-G32) measures the displacement at the free end. P_1 is the main patch for harvesting power. The circuit connected to P_1 for SSHI is composed of several parts: an inductor L for LC_0 resonance to enhance the power; four Schottky diodes (D_1 to D_4) for confining the current flow; the load composed of a resistor and a capacitor; NMOS (2N7002) and PMOS (NDS0610) pair for positive and negative switching. There are two stages for switching:

-when velocity crosses zero from negative to positive, voltage P_1 is at the maximal positive value, the NMOS is switched at this time and the SSHI process will occur through the path L-D_1 -LOAD-D_3 -NMOS.

-the negative stage works with the same logic through the path L-D_2-LOAD-D_4 -PMOS.

Patch P_2 is connected to circuit composed of two Schottky diodes and three capacitors to generate the positive voltages $+V_{CC}$ and $-V_{CC}$ for supplying comparator (TLV3701). Voltage V_{CC} should be larger than 2.5V to make sure that the comparator fully works to drive MOSFET. The comparator chosen here is a nano-power comparator from TI and the supplying current is only 560nA/per channel. This nano-power

comparator is very easy to drive and suitable for low power circuit design.

Patch P_3 is designed for velocity control. It is connected to a current sensing resistor followed by a passive low-pass filter. The resistor used herein is small enough to make sure there is no phase lag. The velocity signal noise (sine wave ideally) is attenuate by the low-pass filter. A comparator is used in order to generate the switching signal (square wave ideally) to drive NMOS and PMOS. The low-pass filter is designed to reduce high-frequency noise without phase lag. Figure 4-11 shows the experimental waveforms of the self-powered V-SSHI device.

Table 4-1. Dimension of the electromechanical transducer.

Steel beam	
LengthxWidthxThickness	168.5mm x 94.3mm x 15mm
First bending mode	41.4Hz
Piezoelectric pathes (PZT-QA)	
P1	38.1mm x 16.5mm x 0.5mm
P2	15mm x 5mm x 0.5mm
P3	15mm x 5mm x 0.5mm

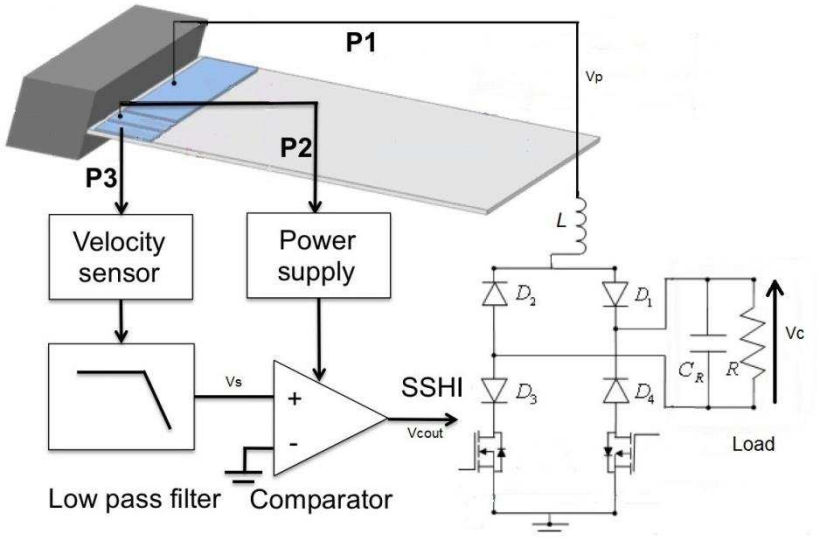

Figure 4-9. Experimental setup and circuit diagram of V-SSHI device.

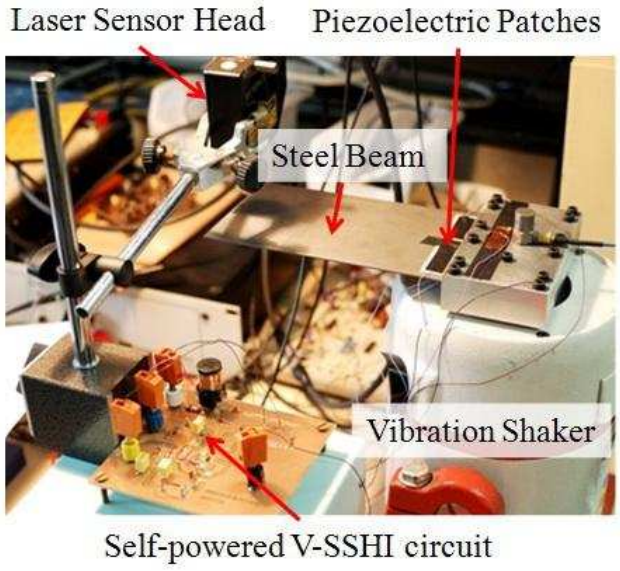

Figure 4-10. Picture of the experimental setup and circuit.

4.3.2 Experimental results

Figure 4-11 shows three waveforms:

- black line V_P is the waveform of the piezoelectric patch P_1,

- blue line V_{Cout} is the output waveform of the comparator,

- red line V_S is the velocity control signal after the low-pass filter.

Although there is still some high frequency noise in the velocity control signal V_S, the comparator work still well; it is a trade-off between reducing noise and phase lag. Observing waveform V_P , we can note that the switching time occurs almost at the peak value of the voltage. The model parameters, identified by measurements, are given in Table 4-2. The experimental and theoretical results of output power are shown in Figure 4-12. All experimental data are acquired for the same acceleration ($a = 2.5m/s^2$). The theoretical curves for standard DC and standard SSHI are drawn from equations (4.2), equation (4.4) and parameters are in Table 4-2. The standard DC experiment (measured using Figure 4-4(a) circuit) and ”SSHI-Experiment” (measured by power supply and function generator using Figure 4-5 circuit) are the reference lines compared to theoretical lines; results show good agreement with predictions. Piezoelectric patch P_3 can be replaced by a smaller one. So, in the experiments of this study, the effect of patch P_3 is neglected. The experimental results (blue point) called "SSHI-Experiment" are measured on the conventional SSHI technique powered by external switching signal. The self-powered V-SSHI technique (red point) is measured by only one patch P_1 . The

output power of V-SSHI circuit is lower than the one of ”SSHI-Experiment” circuit, because the energy is split to supply the auxiliary self-powered circuit. In order to establish the self-powered system, there has to spend parts of energy to supply the electrical circuit. The conventional self-powered technique proposed by [54] is the line with green points. Experimental results show that the maximum output power of self-powered V-SSHI is higher than the conventional technique, essentially due to the efficient phase control.

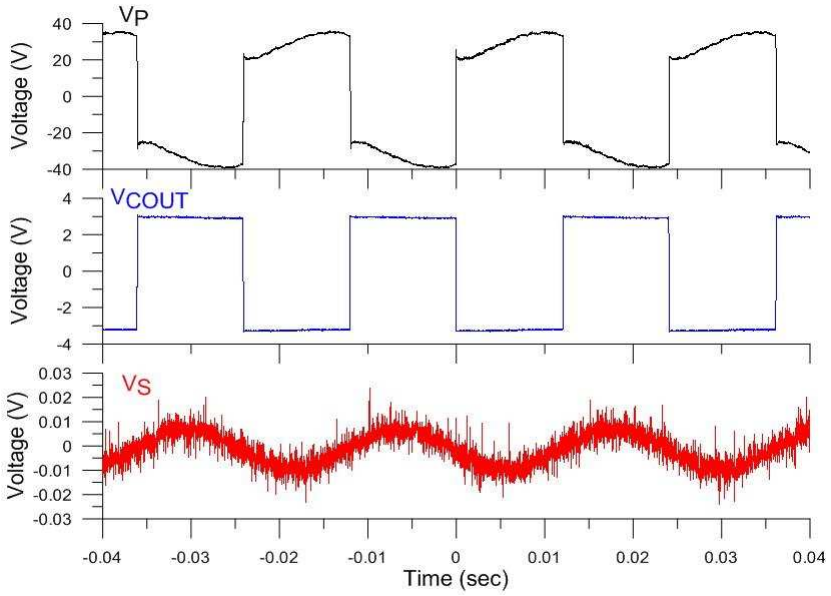

Figure 4-11. Experimental waveform of the self-powered V-SSHI.

Table 4-2. Measurements and model parameters.

f_0	Short circuit resonance frequency		41.41 Hz
f_1	Open circuit resonance frequency		41.45 Hz
ξ	Open circuit damping coefficient		0.00105
Q_I	Quality Factor		2.6
V_D	Diode drop voltage		0.3V
C_0	Clamped capacitance of the piezoelectric element	P_1	25nF
		P_2	3.5nF
		P_3	3.5nF
α	Force-voltage coupling factor		0.00069 N/V
k^2	Electromechanical coupling coefficient		0.00193
M	Mass		182g
K^E	Equivalent stiffness of the structure when piezoelectric is short-circuited		12320Nm^{-1}
D	Damping ratio of the structure		0.1 $Nm^{-1}s^{-1}$

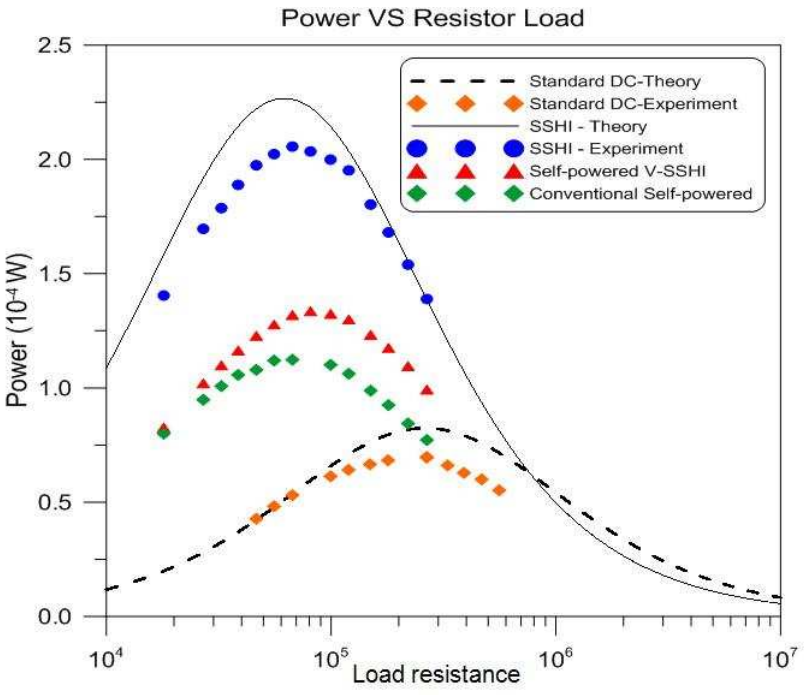

Figure 4-12. Experimental results.

4.4 Conclusion

In this chapter, a self-powered V-SSHI piezoelectric energy harvesting is proposed and this is a new design concept which is different from the traditional design. Based on the outstanding performance of SSHI technique, the self-powered V-SSHI circuit is fully self-powered, requiring no external power supply and though the velocity control, the switching time can be more accurate than with state-of-the-art techniques. The performance of the conventional self-powered circuit is close to the theoretical values of the SSHI; however, it requires an excitation level high enough to work properly [22]. In the self-powered V-SSHI technique, the excitation level doesn't influence the performance and when the supply voltage of the comparator is larger than 2.5V, the whole circuit fully works. The experimental results show better performance and lead to a gain of around 200% compared to the standard DC approach. Of course, the V-SSHI output power is lower than the theoretical SSHI, because the energy is split to supply the auxiliary self-powered circuit. The architecture proposed in this chapter is more beneficial and represents a new step of the design concept. This circuit is easily used in real applications and may be combined with wireless sensor networks.

Chapter 5 Study of a Piezoelectric Switching Circuit for Energy Harvesting with Bistable Broadband Technique by Work-cycle Analysis

In order to increase the output power of the piezoelectric energy harvesting in all aspect including mechanical part design and electrical part design, in this chapter, a piezoelectric energy harvesting device comprised of a bistable vibrating cantilever beam and a switching-type interface circuit (SSHI) are proposed, and the resulting performance are compared to the traditional linear technique. The main contribution focuses on combining two non-linear techniques to achieve an efficient broad band piezoelectric energy harvesting device. So in this chapter, the system is not combined with WSN module. It was known that the synchronized switching techniques increase efficiently the output power of the piezoelectric energy harvester for low-coupled structures. However, the traditional piezoelectric energy harvester based on a cantilever beam is only efficient at resonance. To broaden the available bandwidth, a bistable non-linear technique was proposed. In this paper, the bistable technique and SSHI interface are combined together to accomplish a more efficient broadband piezoelectric energy harvester. The power flow and work-cycles are adopted to simplify the analysis of the switching techniques and then summarize the increasing performance of the non-linear piezoelectric harvester. Finally, simulation results and experimental

validations show that the proposed integrated device owns larger bandwidth and collects more harvested energy

5.1 Introduction

Although the piezoelectric materials exhibit high power density, the linear piezoelectric energy harvester are efficient only when the mechanical system is excited at the resonance frequency; there is largest strain, largest vibration displacement and maximum output power compared to work at non-resonant frequency. However, in practice, the exciting frequency of the ambient vibration source is random and it varies within a frequency range [26]. It is impossible to excite the energy harvester at specific resonance frequency and to keep the system operating on the maximum power point. In the cantilever beam system, the mechanical quality factor is commonly very high. It causes that the device has high harvesting power only at single resonant frequency. In order to increase the power at non-resonant frequency, designing a mechanical system to work in a wide frequency range is necessary. This design concept to enlarge the frequency bandwidth is based on applying external forces. By applying an axial force, the resonant frequency of a piezoelectric cantilever beam can be successfully tuned [55, 56], but these methods are active techniques and the mechanical system is still operated within the linear regime. Another method consists to make a non-linear or bistable

vibration of a cantilever beam to enlarge the workable bandwidth [57-60]. By using simple fixed magnets, this passive technique makes the mechanical system improve the harvesting efficiency within non-resonant regime without any external power.

In this chapter, the performances, drawbacks and system requirements of magnetic non-linear piezoelectric generators combined with the SSHI technique, shown in Figure 5-1(c), will be discussed. According to comparisons with others linear standard generator (Figure 5-1(a)) and linear SSHI generator (Figure 5-1(b)), the voltage waveform across the piezoelectric element and displacement are used to show the efficiency of the bistable piezoelectric energy harvester trough the work-cycle representation. The simulation and experimental results show that the SSHI technique is advantageous over the standard interface for both linear and non-linear cases and non-linear case is advantageous over linear for both the standard interface and SSHI techniques. The theoretical analysis, equivalent circuit model, simulation and experimental results will be presented in following sections.

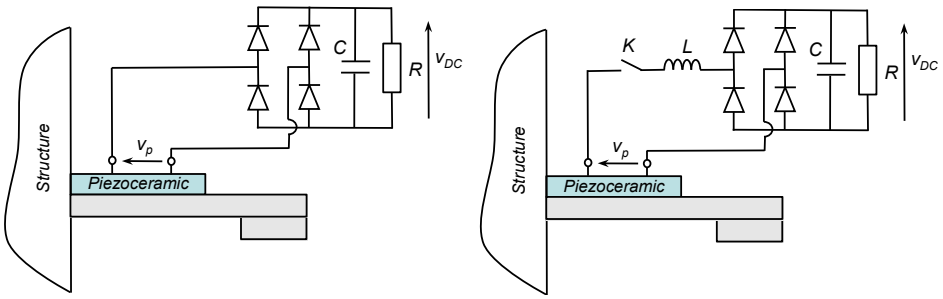

(a) (b)

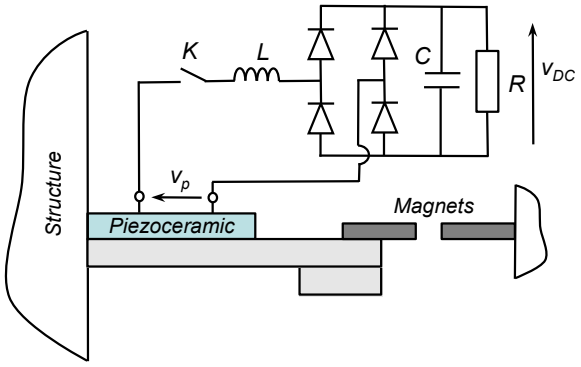

(c)

Figure 5-1. (a) Standard DC Technique (b) Series SSHI Technique (c) Series SSHI Technique with broadband vibration.

5.2 Electromechanical Linear Model

As detailed theoretical analysis in the chapter 2, a mechanical model based on a spring–mass system gives a good description of the vibration behavior near the resonance of the host structure. Therefore, for simplicity, this system can be modeled as a one degree-of-freedom system of a mass M, a spring K^E and a damper D. According to dynamics equation, the differential governing equation of this electromechanical system can be expressed as equations (5.1).

$$M\ddot{x} + D\dot{x} + K^E x + \alpha V_p = F_E \tag{5.1}$$

where F_E is external force and x is displacement exerted on the host structure. The

equation (5.1) is linear equations. However, the bistable energy harvesting technique is a non-linear method essentially, and it is not easy to analyze. To make the analysis more intuitive, the work-cycle (or energy cycle) is adopted here to analyze the non-linear circuit and vibration. The work-cycle is the trace in piezoelectric force-displacement plane. The observing point of interest is the power generated from the mechanical part. At this point, the average power converted into the electric part in a period can be expressed as equation (5.2).

$$P = \frac{1}{T}\int_0^T \alpha \dot{x} V_p dt \tag{5.2}$$

Where T represents the period of the vibration, i.e. $T = 2\pi/\omega$. Accordingly, the energy flowing out of the piezoelectric in one vibration cycle can be expressed as equation (5.3).

$$E = \alpha \int_0^{u(T)} V_p dt \tag{5.3}$$

The integration in equation (5.3) stands for the area in the force-displacement plane, representing the energy flowing out of the piezoelectric element. The real energy, which

flows out of the piezoelectric element, is the key issue in energy harvesting design. The energy that flows out of the piezoelectric element is larger when the vibrating energy harvested by the electronic circuit in each cycle is larger.

5.3 Switching Control Strategy

The equivalent circuit of the single-mode piezoelectric harvester including the switching circuit is represented in Figure 5-2. In this figure, $\dot{x}$ represents the velocity of the host structure at a particular location, which also can be viewed as the current in the equivalent circuit. The voltage V_P is the voltage across the piezoelectric element. In this following, V_P is directly named piezoelectric voltage for simplicity.

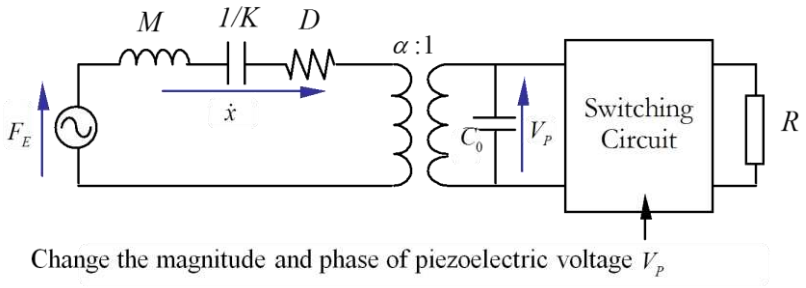

Figure 5-2. Equivalent electric circuit of the single-mode piezoelectric harvester.

Usually in energy harvesting applications, the piezoelectric patches and structure

are weakly coupled. This means that the energy extraction from piezoelectric patches doesn't disturb the vibration behavior of the structure and the magnitude of velocity $\dot{x}$ can be assumed unchanged. As we mentioned in the chapter 2, for weakly coupled structure k^2Q_m is lower than 2 [75]. When k^2Q_m is lower than 2, the SSHI technique can effectively increase the power than the standard interface circuit.

According to equation (5.2) for the weakly coupled structure, the purpose of the switching circuit is to change the waveforms of piezoelectric voltage V_P to enlarge the extracted energy and to keep similar magnitude of velocity. According to equation (5.3), in order to have the best performance, the piezoelectric voltage V_P should be in phase with velocity $\dot{x}$ and the voltage amplitude should be large to harvest the larger energy as well. The circuits studied here are the standard DC rectifier (Figure 5-1(a)) and the series-SSHI technique (Figure 5-1(b)) operated at resonance. Then these two initial techniques are applied to a non-linear bistable structure (Figure 5-1(c)). The key waveforms are given in Figure 5-3.

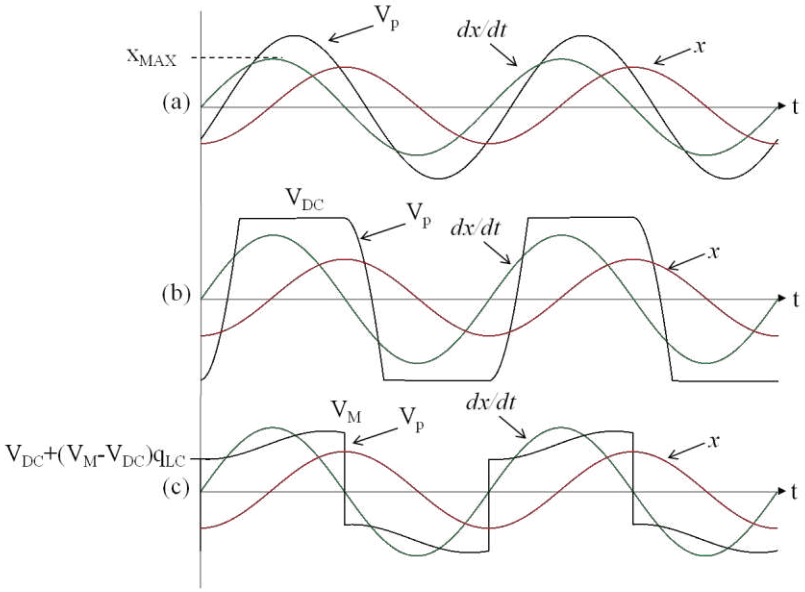

Figure 5-3. The ideal waveforms of voltage V_P, velocity $\dot{x}$ and displacement x: (a) Simple resistive load (b) Standard DC rectifier (c) Series SSHI technique.

5.4 Series-SSHI Technique

The SSHI technique used here is like the classical series-SSHI technique and the detailed theoretical analysis is studied and discussed in the chapter 2. In this sub-section, we just talk and show the significant equations, waveforms and behavior. Figure 5-3(c) shows the theoretical waveforms of series-SSHI. When the vibration velocity crosses zero, the switch is conducted, the inductor L and the piezoelectric capacitor C_0 begin to oscillate. This resonant circuit increases the magnitude and changes the polarity of the voltage across the piezoelectric capacitance sinusoidally, and thus put voltage V_P and

velocity $\dot{x}$ in phase, which indicates that more energy is extracted from the vibration source.

To quantify the performances of energy harvesting devices, the force-displacement diagram is employed to illustrate the energy conversion cycle. In the case of a purely capacitive load on the piezoelectric element, the displacement and voltage are in phase; the area of the cycle is null, so the harvesting energy is equal to zero. When a resistive load is added, a phase shift appears between displacement and voltage (Figure 5-3(a)).

Figure 5-4 shows the force-displacement locus under three conditions. The first condition corresponds to the simple resistive load. The area enclosed by the locus represents the vibratory energy converted into electrical energy. The second condition corresponds to the full-wave bridge rectifier. The extracted energy by the full-wave bridge is lower than in the case of simple resistance because the maximum piezoelectric voltage is lower, but the maximal value of the displacement remains the same. The third condition corresponds to the series-SSHI technique. The energy harvested by the series SSHI technique is much higher than the previous cases because the LC_0 resonance increases the magnitude of V_P in the low coupling condition and the magnitude of displacement does not change.

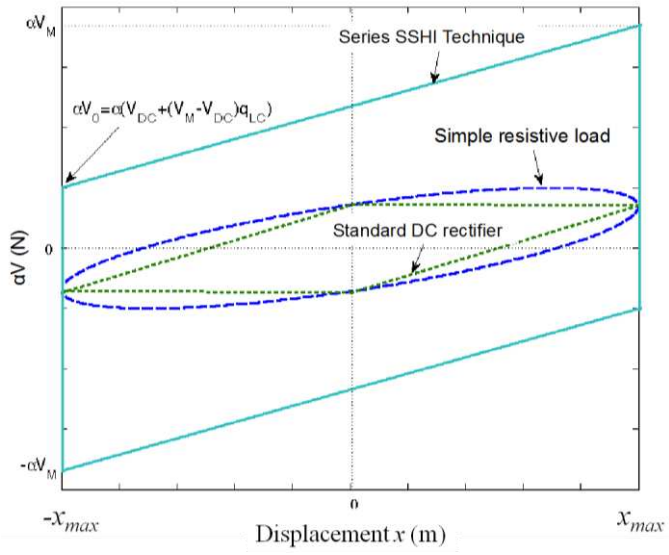

Figure 5-4. Force-displacement diagram: simple resistive load, standard DC rectifier and series SSHI technique.

From the energy conversion cycle shown in Figure 5-4, and based on the geometric relations among the area in different colors, we can calculate the extracted energy. For the series-SSHI, the transferred energy ESSHI can be expressed as follows:

$$E_{Series-SSHI} = 2\frac{\alpha^2}{C_0}\frac{(1+q_{LC})}{(1-q_{LC})}\hat{x}^2 \tag{5.4}$$

where $q_{LC} = e^{-\frac{\pi}{2Q_l}}$ is a function of the quality factor Q_{LC} of the resonant LC_0 circuit. The usual value of the q_{LC} is around 0.7 in the normal experiment because if the

system have very high quality factor it will lead bulky and expensive inductor [34]. For the standard DC rectifier, the transferred energy E_{DC} can be expressed as follows:

$$E_{DC} = 2\frac{\alpha^2}{C_0}\hat{x}^2 \tag{5.5}$$

The conclusion that we can get from the work-cycle observations is we can evaluate the performances of the energy harvesting circuits by the size of the area. This maximum corresponds actually to the rectangular shape in the force-displacement plane for the same external voltage and displacement.

5.5 Bistable Energy Harvester

The most piezoelectric energy harvesting system is a linear electromechanical device excited at resonance. Considering that most realistic vibration environments are more accurately described as multi-frequency and time varying, narrowband linear systems are inefficient under these conditions. Non-linear systems, on the other hand, are capable of responding over a broad frequency range. The solution is to use a bistable inertial oscillator comprised of permanent magnets and a piezoelectric cantilever beam (Figure 5-1(c)). The bistable behavior is obtained with two magnets. One is mounted on

the tip of the beam and the other one is fixed on a stage. Because the two magnets repulse to each other, the system will be a bistable system and there will be two possible stable positions as shown in Figure 5-5. When the distance between these two magnets is designed properly, the non-linear behavior can broaden the available bandwidth [57, 86].

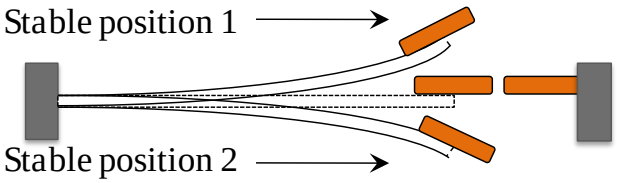

Figure 5-5. Principle of the broadband energy harvesting device with a destabilized zero equilibrium position.

The non-linear magnetic repulsion force F_M given by the interaction of the magnets can be simplified to one-dimensional model and it is acting only in vertical direction [86]. The magnetic force $F_M(x)$ is a variable value and depends on the displacement of the cantilever beam x and the distance between the moving and the fixed magnets. By using the curve fitting method, the magnetic force F_M for a specific distance can be expressed as equation (5.6) [57].

$$F_M(x) = \frac{ax}{1+bx^4} \tag{5.6}$$

where a and b are the fitted parameters.

In order to analyze the non-linear energy harvester with an electric interface, in this chapter we adopt an electric equivalent impedance representation. According to equations (5.1) and (5.6), the equivalent circuit model can be represented as shown in Figure 5-6. The host structure with piezoelectric elements mechanical is modeled by the classical equivalent circuit. The magnetic force F_M is taken into account by adding a non-linear magnetic feedback loop. The main advantage of this equivalent circuit is that it can be easily simulated and does not need to use numerical methods. This method has some limitations. First of all, it considers the equivalent spring as a linear one in which the stiffness is independent of the position of the mass. In the present case, this is true only when the displacement is small with respect to the distance between the moving and the fixed magnets. When this hypothesis is not verified, significant errors can take place.

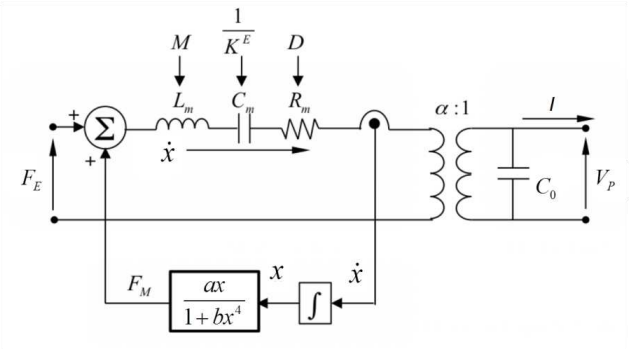

Figure 5-6. Electric equivalent circuit of the piezoelectric energy harvester coupled with non-linear magnetic force.

5.6 Simulation, experimental results and discussion

5.6.1 Experimental setup

In order to demonstrate the performances of the energy harvesting devices, a simple experimental test was performed on a clamped cantilever steel beam with 31-type PZT-QA elements provided by the Eleceram Technology Co., Ltd. There were two piezoelectric elements. The first one is the main element to harvest the energy, and it was connected to the series-SSHI interface. The second one is smaller size, and it was used only to sense the velocity and to generate the driving signal for the switches of the SSHI interface [36]. The electronic components in this experiment were supplied by an external DC source. A picture of the tested beam and SSHI circuit is shown in Figure 5-7 and the detailed experimental setup is presented in Figure 5-8. The distance between

the two magnets was 3.5 mm. The dimensions of the beam and the piezoelectric elements are shown in Table 5-1.

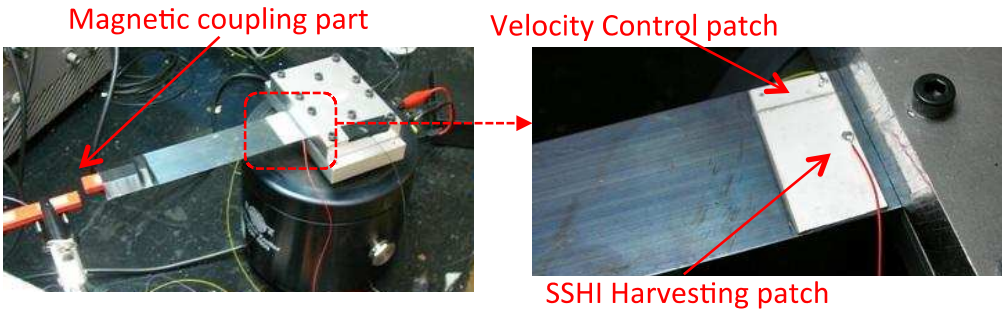

(a)

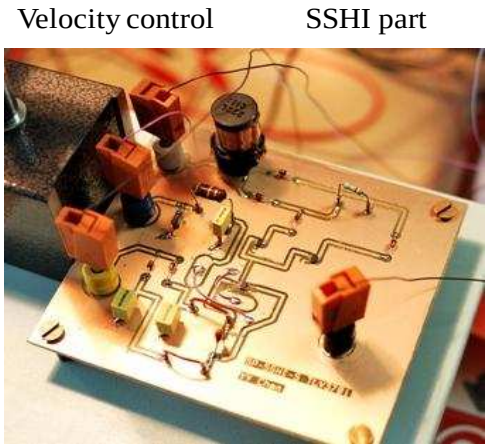

(b)

Figure 5-7. (a) Experimental beam structure (b) SSHI circuit.

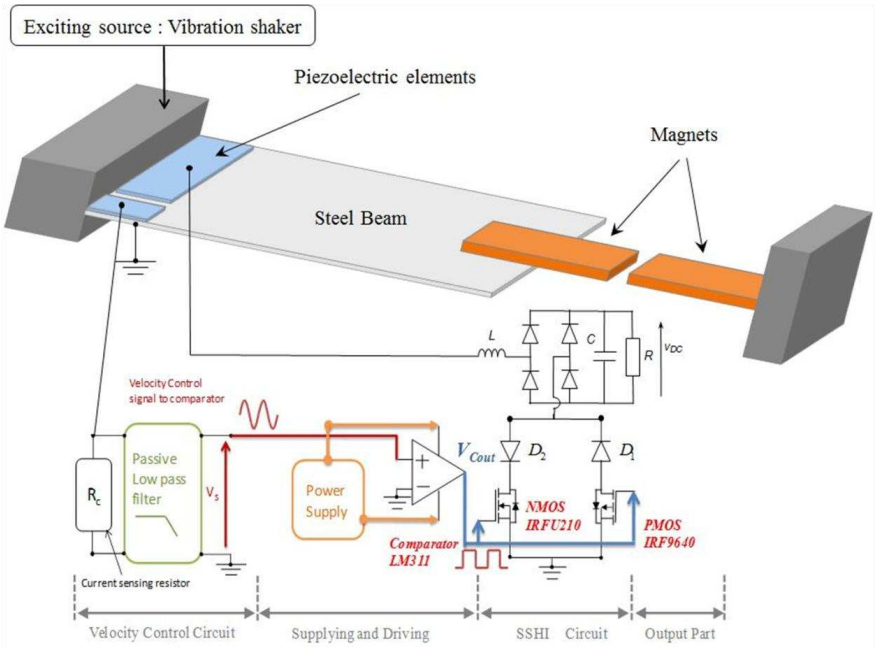

Figure 5-8. Experimental setup.

Table 5-1. Piezoelectric elements and Steel Beam.

	Steel beam	Piezoelectric element for SSHI	Piezoelectric element for velocity signal
Length (mm)	189	28	6
Width (mm)	34.8	16.5	16.5
Thickness (mm)	0.8	0.5	0.5
Location	None	1 mm from fixed end	1 mm from fixed end

The beam was excited at the fixed end by an electromagnetic shaker (Brüel & Kjær 4809). The shaker is driven by a data acquisition card (NI-DAQ USB-6259). To realize the SSHI circuit, two diodes and two MOSFET switches (Metal Oxide Semiconductor Field Effect Transistor) were used. When the velocity signal goes zero crossing from negative to positive, the NMOS switch (IRFU210) is switched-on and when the signal

goes zero crossing from positive to negative, the PMOS switch (IRF9640) is switched-on. The two diodes confine the current flow, and the inductor L resonates with the clamped capacitor C_0 of the piezoelectric-element. Parameters of the model were identified from the experimental measurements. The tip displacement of the beam x was measured when the piezoelectric element is in open circuit and in short circuit. D, M, K^E, α and C_P were calculated with Equations (5.7) to (5.10).

$$\alpha = \frac{V_{OP}}{x_{OP}} C_0 \tag{5.7}$$

$$K^E = \alpha \frac{V_{op}}{x_{op}} \frac{f_{sh}^2}{f_{op}^2 - f_{sh}^2} \tag{5.8}$$

$$M = \frac{K^E}{\omega_{op}^2} \tag{5.9}$$

$$D = 2\zeta M \omega^{op} \tag{5.10}$$

where V_{op} is the open-circuit measured piezoelectric voltage for a given tip displacement x_{op} of the beam. The parameter model values are given in Table 5-2.

The parameter b of the magnetic force, in equation (5.6), sets the static beam tip displacement and parameter a sets the maximum value of the magnetic force as shown in Figure 5-9. First, the parameter b was calculated according the experimental measure

of displacement x_{max}=1.2mm. Then the parameter a was obtained by fitting the experimental voltage curve in Figure 5-11 & Figure 5-12. According to the experiment results, the proper parameters could be chosen.

Table 5-2. Measured values and model parameters.

Symbol	Description	Value (unit)
f_{op}	Open-circuit resonant frequency when all piezoelectric elements are in open circuit	10.4 Hz
f_{sh}	Short-circuit resonant frequency when all piezoelectric elements are in short circuit	10.307 Hz
k^2	Electromechanical coupling coefficient	0.0018
ζ	Damping ratio	0.02
Q_m	Mechanical quality factor	2.09
M	Mass	49 g
K^E	Equivalent stiffness when all piezoelectric elements are in short circuit	209.22 N/m
K^D	Equivalent stiffness when all piezoelectric elements are in open circuit	211 N/m
D	Damping coefficient	0.15 N/m/s
α	Force–voltage factor	0.00007716 N/V
q_{LC}	Inversion factor	0.7
C_P	Clamped capacitance	15.57 nF
L	Resonance inductor in SSHI	10 mH
a	Fitting magnetic force parameter	280
b	Fitting magnetic force parameter	1.5×10^{11}

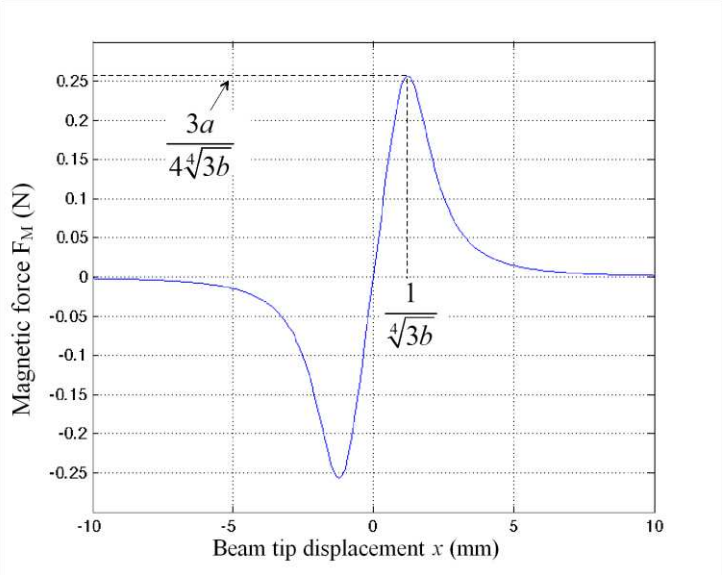

Figure 5-9. The magnetic force F_M as a function of the beam tip displacement x.

5.6.2 Frequency sweeping

The main interest of this work is broadening the frequency range from which energy can be extracted. To show the interest of bistable non-linear technique to broaden the available bandwidth the excitation frequency was linearly increasing. This was accomplished using an excitation of the form $\gamma = A_0 \cos\left(\left(\omega_0 + \omega_S t\right)t\right)$ where ω_0 is the initial pulsation and ω_S is the frequency sweep rate. A_0 is the amplitude of acceleration: $2m/s^2$.

The experimental testing was performed on the linear and non-linear clamped cantilever beam shown in Figure 5-8. The simulation was carried out with Matlab and PSIM software packages as shown in Figure 5-10. The module Simcoupler in PSIM software is used to make a link between Simulink in Matlab and PSIM. The driving chirp frequency of the input force is sent from Matlab to the electric circuit implemented in PSIM. The simulated results will be sent back to Matlab and organized. Figure 5-11 and Figure 5-12 show the experimental and simulation results of increasing frequency sweeping for the case of standard DC rectifier interface and SSHI interface, respectively. The experimental driving signal was chirping with frequency range from 5 Hz to 30Hz in 250 seconds. The simulation driving signal was ranging from 1Hz to 30 Hz in 300 seconds and its sweeping rate was the same as the experimental conditions

(ω_S=0.1 Hz/s). The sweeping rate was kept sufficiently small in order to reflect the non-linear response [87]. The output voltage for the linear system without magnetic force and the output voltage for the case with the magnetic force are plotted in Figure 5-11. The load resistance was chosen 2MΩ to show the piezoelectric terminal voltage. Comparing to the experimental results, the simulation shows good agreement with the experimental data. The results of Figure 5-11 & Figure 5-12 show that the piezoelectric voltage V_P at 10.4 Hz (resonant frequency in linear system) is almost the same for the both systems, but at non-resonance frequencies the bistable system can improve the output power obviously. The non-linear effect at the resonance is limited unlike in the non-resonant region. At the resonance, the driving force from resonant effect is larger than the magnetic force in our experiment, so the non-linear magnetic coupling technique cannot work effectively. The results also show considerable chaotic motion when f<5 Hz and between 10Hz and 17Hz. For other frequencies the motion is would be periodic response. This result is in agreement with study in Stanton et al. [86] and Thompson [88]. Over a wide frequency range, there is enough energy imparted into the bistable system to enable drive the beam from one stable position to the other.

In the non-linear system there is a critical frequency when the potential energy is not enough to drive the system from one stable position to another [60, 89]. In our

experimental results shown in Figure 5-11 & Figure 5-12, the critical frequency is around at 23Hz. When the driving frequency is higher than 23Hz, the piezoelectric terminal voltage in non-linear system is the same as in linear system.

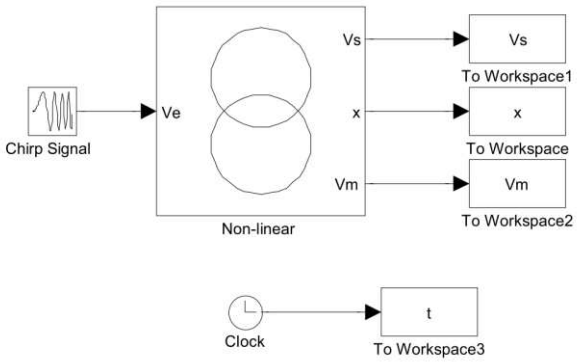

(a)

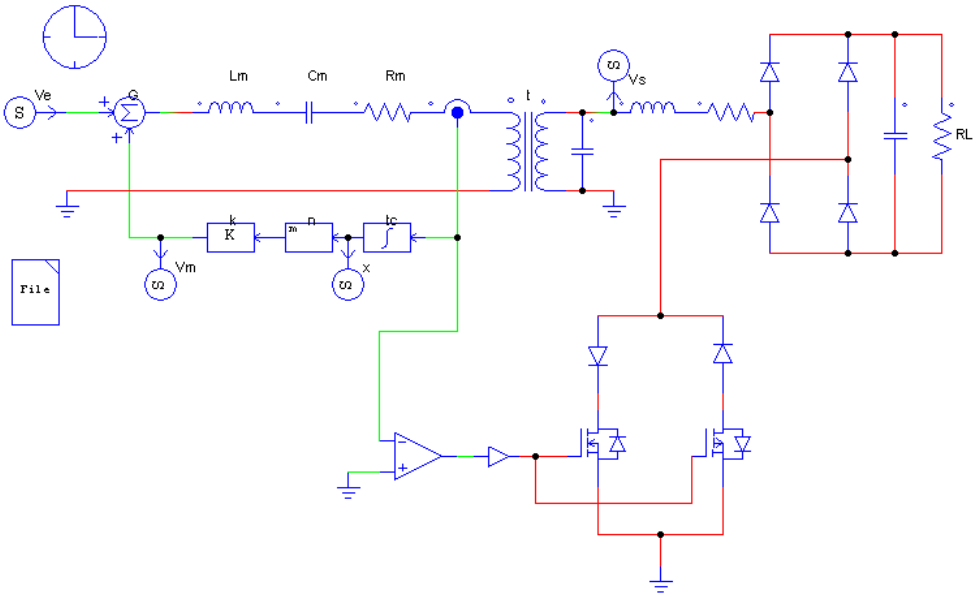

(b)

Figure 5-10. Non-linear simulation setup (a) Matlab Simulink and (b) PSIM

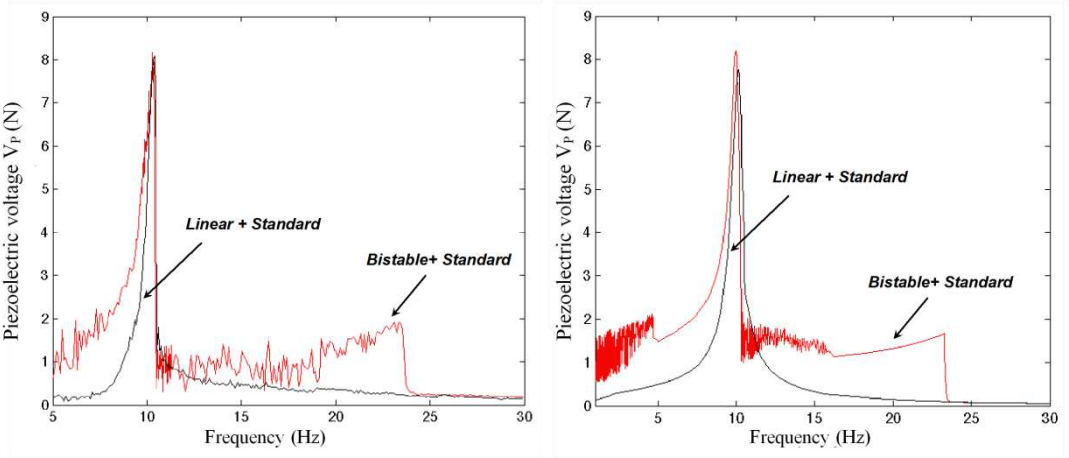

(a) (b)

Figure 5-11. (a) Experimental results (b) simulation results of nonlinear piezoelectric energy harvester combined with standard DC rectifier interface: increasing frequency sweeps.

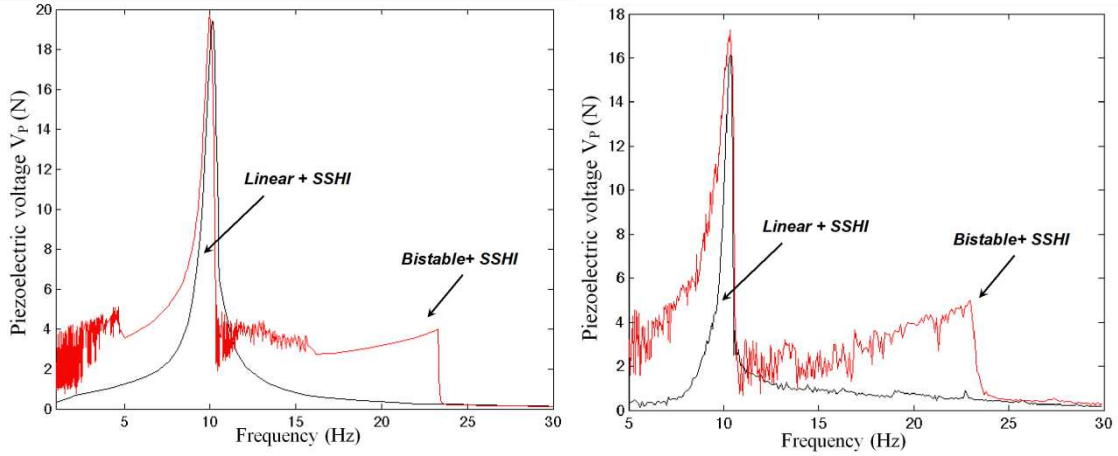

(a) (b)

Figure 5-12. (a) Experimental results (b) simulation results of nonlinear piezoelectric energy harvester combined with SSHI interface: increasing frequency sweeps.

5.6.3 Work cycles study

Two specific frequencies (at-resonance: f=10.4 Hz and off-resonance: f=5Hz) were chosen to be the examples to analyze the work cycles. Figure 5-13 and Figure 5-14 show simulation results of the voltage V_P across the piezoelectric element, the velocity and the voltage-displacement diagrams at resonance frequency of the structure (10.4 Hz) for standard DC rectifier and SSHI technique. The maximum displacement is x_{max} = 2.5 mm. According to the Equation (9), the energy by period for the SSHI technique is E_{SSHI}=13.5μJ and thus the power is P_{SSHI} = 140.4μW. According to the Equation (10), the E_{DC} =2.39μJ and power for standard DC rectifier is P_{DC} =24.86μW. Figure 5-15 and Figure 5-16 show voltage V_P across the piezoelectric element, the velocity and the voltage-displacement diagram at non-resonance frequency of the structure (5Hz) for standard DC rectifier and SSHI technique.

Figure 5-13 to Figure 5-16 clearly show that the SSHI interface enlarges the work-cycle area by increasing the piezoelectric voltage and non-linear bistable technique increase the work-cycle area by increasing beam displacement at non-resonance. Therefore, if we compare the energy harvested at the non-resonance frequency (Figure 5-15 and Figure 5-16) the work-cycle area of bistable device is much wider. That means that for both cases, standard DC rectifier and series SSHI, the

bistable device keeps good performances at the would-be resonance but increases them at the non-resonance.

Figure 5-17 shows the output power for the SSHI technique in the case of bistable and linear devices and for the two frequencies: at-resonance 10.4Hz and non-resonance frequency 5Hz. The maximum output power at resonance frequency (10.4 Hz) is 0.14 mW. This power at non-resonance frequency (5 Hz) with linear device is only 0.3µW, but with bistable vibration the output power is 8µW. Comparing bistable system to linear system results, the output power close to the resonance frequency is almost the same, but more energy can be harvested in bistable system at non-resonant frequency when the displacement is large enough to drive the beam from one stable position to the other stable position.

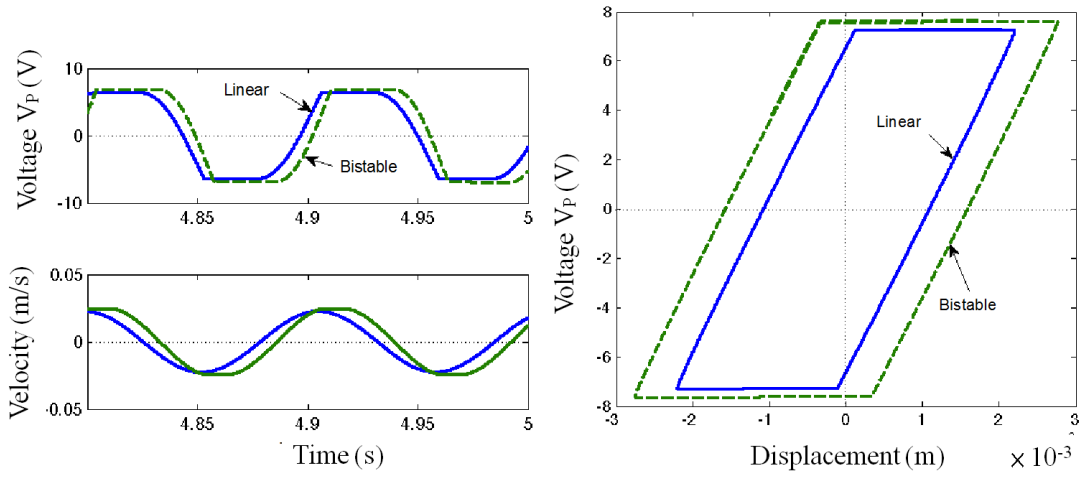

(a) (b)

Figure 5-13. Standard DC rectifier @ f = 10.4 Hz, (a) Piezoelectric voltage and velocity (b) Work cycle.

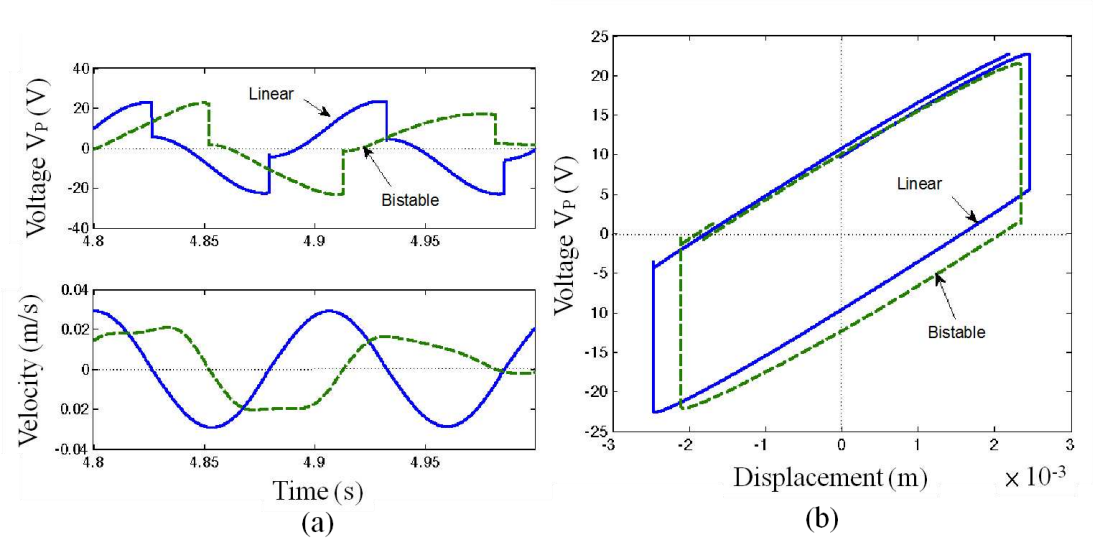

Figure 5-14. Series SSHI @ f = 10.4 Hz, (a) Piezoelectric voltage and velocity (b) Work cycle.

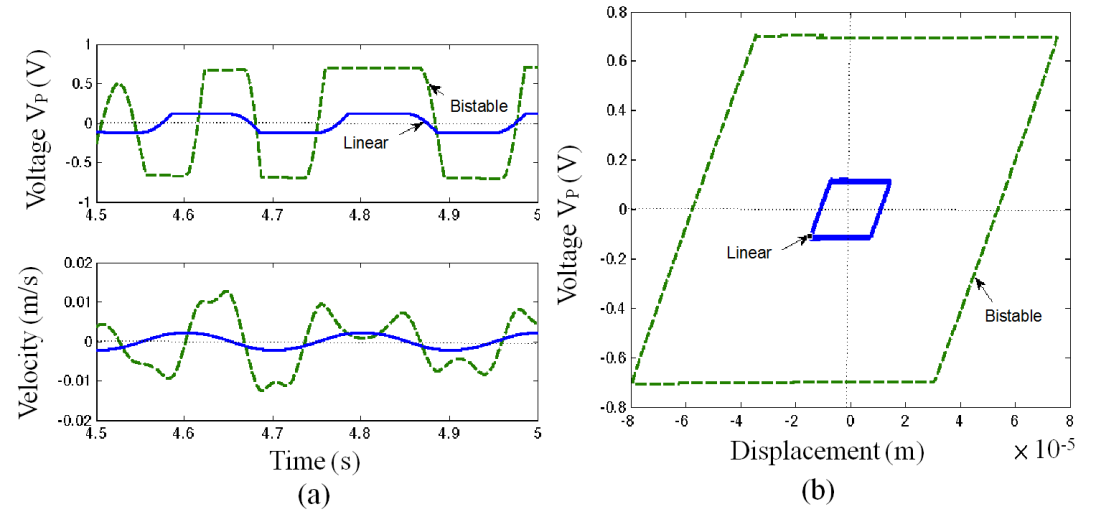

Figure 5-15. Standard DC rectifier @ f = 5 Hz, (a) Piezoelectric voltage and velocity (b) Work cycle.

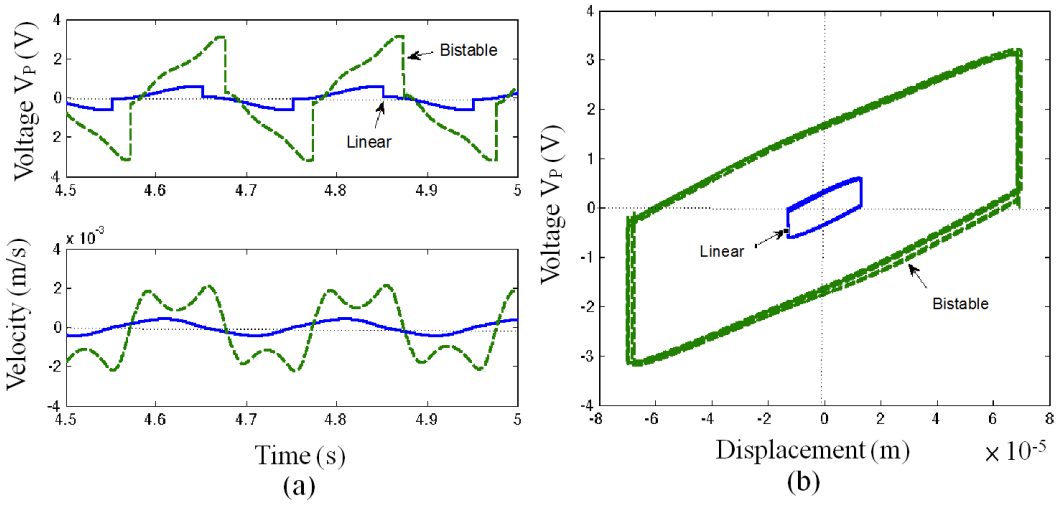

Figure 5-16. Series SSHI @ f = 5 Hz, (a) Piezoelectric voltage and velocity (b) Work cycle.

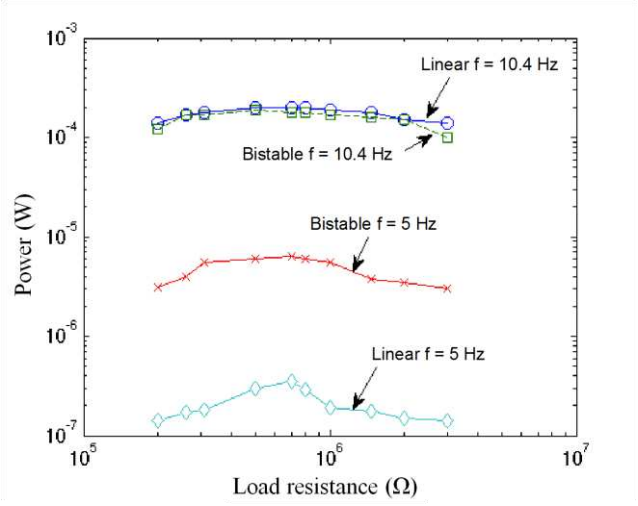

Figure 5-17. Experimental results of the output power for SSHI technique.

5.7 Conclusion

This chapter studies the performances of magnetic non-linear piezoelectric generator combined with a series-SSHI interface in the weak coupling case. The

equations of motion for a one-degree-of-freedom piezoelectric cantilever beam with magnetic non-linear force were derived and an equivalent electric circuit is proposed. Then, this equivalent electric circuit is used to simulate a bistable piezoelectric generator with the series-SSHI technique. Finally, the non-linear generator was tested experimentally and compared with work-cycle to standard interface and linear technique. The SSHI technique has proved that it is an effective technique to improve output power over the standard interface in both linear and bistable cases. Moreover, the non-linear coupling technique has proved that it is not only advantageous over linear technique for standard interface but also for SSHI interface. It is interesting to combine these two remarkable techniques and the results show that these two techniques can work well together. The SSHI interface enlarges the work-cycle area by increasing the piezoelectric voltage in the weak coupling case and non-linear bistable technique increase the work-cycle area by increasing beam displacement inducing voltage to increase. According to the analysis of work-cycles, the synchronized switching interface and non-linear bistable technique are two major factors for designing a broad bandwidth and efficient energy harvester. Through these two non-linear techniques, the piezoelectric harvester can work more efficiently and more output power at a broadened frequency range can be gained.

Chapter 6 Self-Powered Semi-Passive Piezoelectric Structural Damping Based on Zero-Velocity Crossing Detection.

In recent years, semi-passive vibration damping using non-linear synchronized switching methods has been intensively investigated and discussed. In this chapter, a self-powered synchronized switch damping on inductor (SSDI) technique based on zero-velocity crossing detection is proposed and investigated. The control signal used to drive the switches is obtained by sensing velocity as we used in the self-powered V-SSHI technique in energy harvesting. A totally self-powered damping system powered by harvested energy using SSDI technique with velocity sensing and without external power is established. Compared with the conventional technique based on voltage peak detector, this technique do not generate lag in detection of switching time. The theoretical model, the experimental evaluation and the drawback of the self-powered zero-velocity crossing detection switching technique are discussed in this study. The system performance is also compared with the externally powered system.

6.1 Introduction

Many successful applications of piezoelectric materials for structure vibration suppression have been developed in recent decades. In these applications, piezoelectric

materials convert the vibration energy of the host structure into electrical energy, and then the generated electrical energy is dissipated in a shunt circuit. The piezoelectric shunt techniques were widely used due to their simple configurations and compact size, but these techniques are better to be self-powered to reduce the system complexity. In some applications, like automotive and aeronautics, the external power is limited [90, 91], the self-powered design can eliminate the requirements of external power supply.

Several versions of self-powered SSDI technique have been proposed [92, 93]. The conventional method is based on peak voltage detection [93, 94] using a small energy storage capacitor. The peak detection is made using an envelope detector: a comparison between envelope and piezoelectric voltage is made with a bipolar transistor. The drawback of this method is the lag in detection of switching time due to the use of the transistor, which degrades the damping performance. The principle of the peak detector method is shown in Figure 6-1(a).

In this chapter, a self-powered SSDI technique based on zero-velocity crossing detection is proposed and investigated. Hereafter this technique in this chapter is called SP-SSDI. Based on the self-powered system used in piezoelectric energy-harvesting devices (V-SSHI) [36], SP-SSDI does not require external instruments. The control signal used to drive the switches is obtained by sensing velocity, and then compare to

zero. A totally self-powered damping system powered by harvested energy using SSDI technique with velocity sensing and without external power is established. The concept of the proposed system is shown in Figure 6-1(b).

The chapter is organized as follows: the second section 6.2 summarize the SSDI technique and present the theoretical analysis. The next section 6.3 presents the detailed analysis of the self powered SSDI based on zero-velocity crossing detection technique. Section 6.4 presents the experimental results that include the time domain evaluation for different excitation levels, the measurement of the efficiency and the system frequency response results. Finally, the last section 6.5 concludes this chapter.

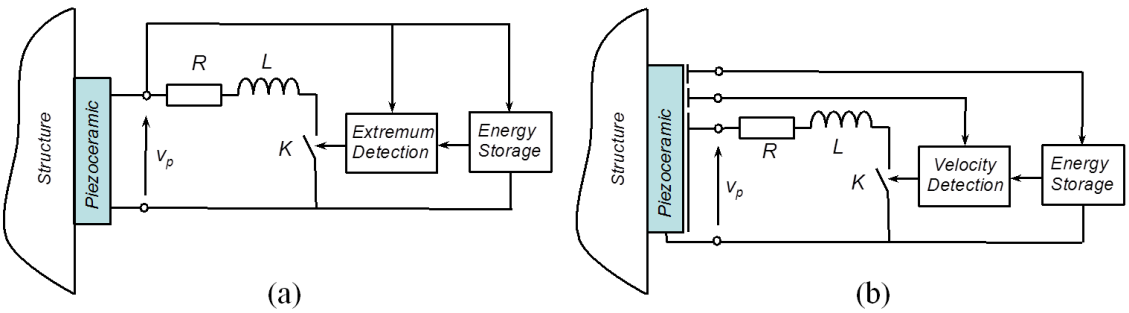

Figure 6-1. (a) Principle of voltage peak detector method (b) Principle of zero velocity crossing detector method.

6.2 SSDI Technique

The electrical circuit of the semi-passive damping technique called SSDI (Synchronized Switching Damping on an Inductance) is represented in Figure 6-2(a). An inductor L, a resistance R and a switch K are connected in series with the piezoelectric patch. The piezoelectric patch voltage V_P is switched across the LR shunt circuit. The dissipated energy of the structure depends on the voltage amplitude across the piezoelectric patches. The role of these additional patches is to increase the amplitude of voltage V_P and thus to increase the damping effect. The switch K is turned ON when a maximum of displacement x occurs and the voltage V_P starts to oscillate, until K is turned OFF. The switching ON period is equal to a half of the resonant period of the LC_0 circuit. Assuming that the electrical resonant period is very small compared to the mechanical vibration period, voltage V_P can make the inversion in this short period. The same function can be obtained by turning switch K ON at the minimum displacement. Theoretical waveforms of the displacement x, the velocity dx/dt and the voltage V_P of the SSDI technique are shown in Figure 6-2(b). The amplitude of voltage V_P is limited by the loss of energy during the inversion process.

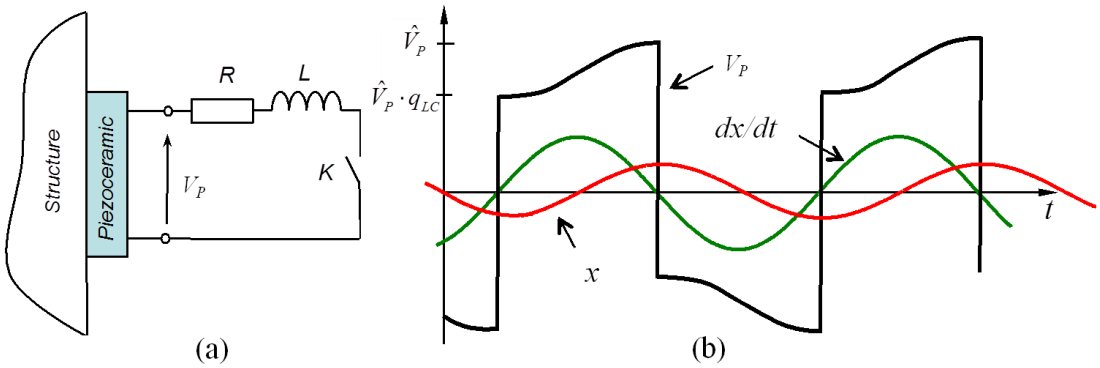

Figure 6-2. (a) Electric circuit of the SSDI technique (b) Key waveforms of the SSDI technique.

The absolute value of the voltage of the piezoelectric patch after inversion is less than the initial voltage. This difference occurs because of the energy losses that occur due to the energy flow between the capacitance and the inductor during the switching interval. The absolute value of the inverted voltage is $q_{LC}\hat{V}_P$, where $q_{LC} = e^{-\frac{\pi}{2Q_i}}$ is a function of the quality factor Q_{LC} of the resonant LC_0 circuit.

Analytic calculation of the displacement amplitude at resonance ω_0 can be made from previously expressed equations. The expression of the mechanical displacement $\hat{x}_{SSDI}$ as a function of external force amplitude F_E and the resonant circuit factor q_{LC} is given in equation (6.1) [73],

$$\hat{x}_{SSDI} = \frac{F_E}{D\omega_0 + \frac{4\alpha^2(1+q_{LC})}{\pi C_0(1-q_{LC})}} \tag{6.1}$$

6.3 Self-powered zero-velocity crossing detection for SSDI Technique

Due to the use of switches in the SSDI technique, the shunt circuit requires an external power source. To design a totally self-powered device, a part of extract energy for damping can be used to power the electronics. Moreover, because it is a synchronous technique, the displacement or the velocity must be measured accurately to obtain the driving signal for the switches. The technique proposed here is to divide the piezoelectric patches into three parts. The largest part, called P_1, behaves like the conventional piezoelectric patch used in the SSDI technique to dissipate the vibration energy. The second piezoelectric patch, called P_2, is a smaller patch that works like energy harvesting device to provide power supply to other electronic circuit. The third piezoelectric patch, called P_3, is a smaller patch designed to sense the velocity and to generate driving signal to control the switches at the optimal time. All three patches contribute to damp the structure.

A schematic of the complete electronic circuit is shown in Figure 6-3 with the functions of different sub-circuits labeled in the same figure. The system will be analyzed in detail in the following subsections. To obtain a precise velocity signal, P_3 is cut from the electrode of the lower piezoelectric patch, and the patch is positioned on the centerline of the cantilever, as shown in Figure 6-3.

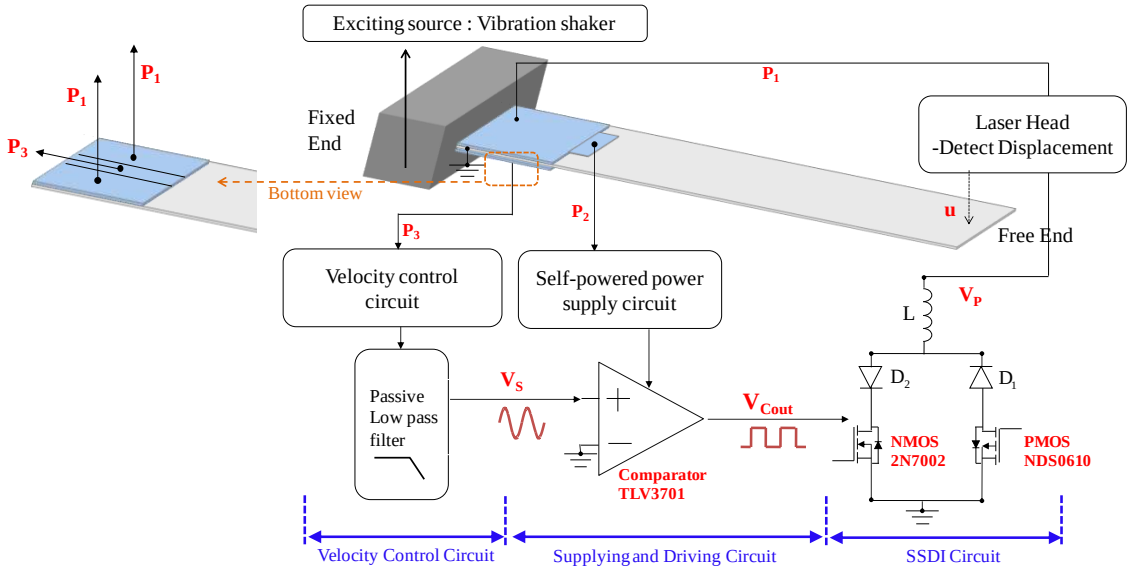

Figure 6-3. Schematic diagram of the zero velocity crossing detection self-powered SSDI technique.

6.3.1 Zero-velocity crossing detector (piezoelectric-patch P_3)

Figure 6-4 shows the electric circuit and the theoretical waveforms of the zero-velocity crossing detector. Since the mechanical current in the electric equivalent circuit of a piezoelectric patch can be assumed to be velocity; if the output terminal is short-circuited, the current through this short-circuit is proportional to velocity, i.e. $i_{sh} = \alpha \dot{x}$. To convert this current into voltage, this short-circuit can be made by a small resistance. Thus, voltage across the shunt resistance represents the velocity of the structure. The value of the current-sensing resistance must be much smaller than the output impedance of the piezoelectric patch. As shown in Figure 6-4(b), the velocity

signal V_S (black curve) is in phase with the output current dx/dt (green curve). To avoid the noise problems when SSDI is active, a low-pass filter is necessary, because the voltage inversion introduces high frequency vibrations into the system. A third-order low-pass filter is used; it is composed of two capacitors and an inductor. The design goal of the filter is to ensure that the high frequency noise is reduced sufficiently to generate an accurate control signal with minimum phase lag to keep the efficiency of the SSDI system. Finally, the filter output voltage V_S is connected to a comparator, and the output of the comparator V_{Cout} is used to drive the switches, as shown the red curve in Figure 6-4(b).

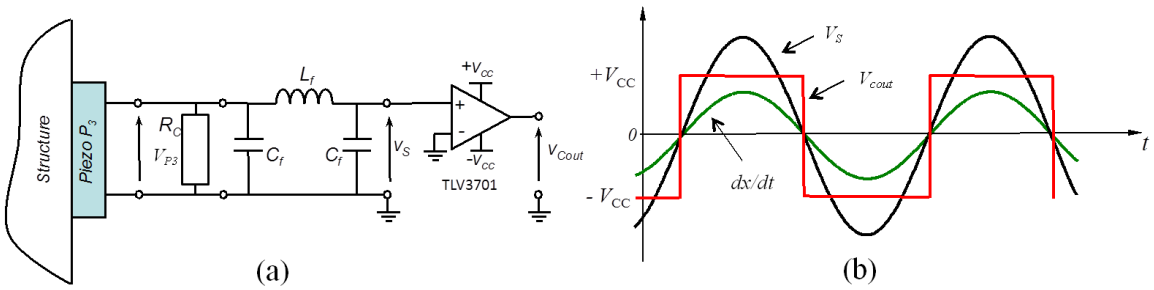

Figure 6-4. The velocity zero crossing detector: (a) electric circuit (b) theoretical waveforms.

Compared to the conventional switching method using a voltage peak detector, the velocity-synchronized signal should theoretically cause the switches to switch more precisely at the optimal time. Because the conventional peak detector uses the diode drop to detect the peak voltage, it produces a time lag between the peak time and the

switching time.

Figure 6-5 shows the Bode diagram of the filter of zero-velocity crossing detector, as measured by an SR780 dynamic signal analyzer. The Bode diagram shows that the corner frequency is approximately 340Hz. The first natural frequency of the cantilever beam is approximately 34Hz; approximately 10 times lower than the corner frequency of the low-pass filter. The low-pass filter design reduces the high frequency noise of the velocity signal effectively without altering the phase.

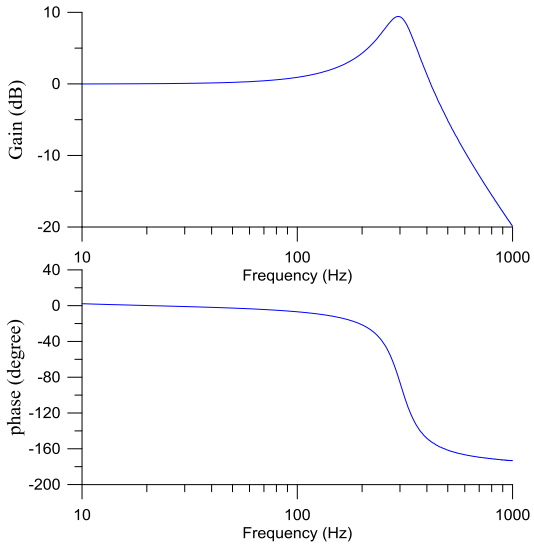

Figure 6-5. Bode diagram of the filter of the zero velocity crossing detector.

6.3.2 Power supply (piezoelectric-patch P_2)

Figure 6-6 shows the electric circuit and the theoretical waveforms of the power supply part. This circuit provides two DC voltages sources, V_{CC} and $-V_{CC}$, to supply power to the comparator and the switches of the SSDI circuit. The power supply circuit

is composed of two diodes (D_A and D_B) and three capacitors (C_P, C_N and C_r). The two diodes maintain the correct positive and negative current flows to charge the capacitors. C_P regulates the positive voltage between V_{CC} and ground, and C_N regulates the negative voltage between $-V_{CC}$ and ground. C_r regulates the voltage between V_{CC} and $-V_{CC}$ and acted as an energy storage buffer. Two Zener diodes D_Z are used to limit excursion and to regulate the DC voltage. The two regulated voltages, V_{CC} and $-V_{CC}$, are connected to the comparator, and the output of the comparator is used to drive the switches. The comparator used in this application is a Nano-power comparator TLV3701 from Texas Instrument (Dallas USA) that sinks a small and constant current (I_{Comp}=560nA) for a voltage V_{CC} higher than 2.5V. Assuming that the equivalent load of the comparator between the two regulated voltages is $R_{eq} = 2V_{CC} / I_{Comp}$, the voltage V_{CC} can be expressed as in equation(6.2) [77].

$$V_{CC} = \frac{1}{2} \frac{\alpha R_{eq} \omega_0}{C_0 R_{eq} \omega_0 + \pi} \hat{x} \tag{6.2}$$

Using equation(6.2) given the relation between α, C_0 and the parameters of the piezoelectric patches, the voltage V_{CC} can be rewritten as equation(6.4). The parameters

of the piezoelectric patches described in Table 6-1, C_0 and α are calculated as equation(6.3).

$$\alpha = e_{31} w,\ C_0 = \varepsilon_{33}^{S} \frac{wl}{t} \tag{6.3}$$

$$V_{CC} = \frac{1}{2} \frac{e_{31} \frac{2V_{CC}}{I_{Comp}} \omega_0}{\varepsilon_{33}^{S} \frac{wl}{t} \frac{2V_{CC}}{I_{Comp}} \omega_0 + \pi} \hat{x} \tag{6.4}$$

Table 6-1. piezoelectric physical parameters.

w	Width of the piezoelectric patches
t	Thickness of the piezoelectric patches
l	Length of the piezoelectric patches
c_{11}^{E}	Elastic rigidity of equivalent patches in short-circuit
e_{31}	Permittivity of piezoelectric patches
ε_{33}^{S}	Piezoelectric coefficient of equivalent patches

Since voltage V_{CC} must be higher than 2.5V, we can find a relation between the amplitude of displacement and the size of piezoelectric patch P_2, as shown in equation(6.5).

$$V_{CC} = \frac{e_{31} w \omega_0 \hat{x} - \pi I_{Comp}}{2\varepsilon_{33}^{S} \frac{wl}{t} \omega_0} \geq 2.5V \tag{6.5}$$

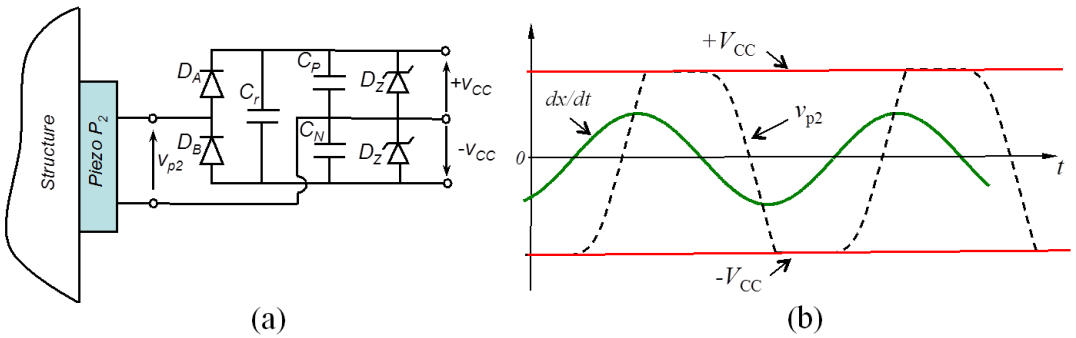

Figure 6-6. Power supply circuit: (a) electric circuit diagram and (b) Key waveforms.

6.4 Experimental results and discussion

6.4.1 Experimental setup

Figure 6-7 shows the experimental setup and pictures of the zero-velocity crossing based SSDI damping system. The experimental structure is a cantilever steel beam with three 31-type PZT-QA patches provided by the Eleceram Technology Co., Ltd.(Taoyuan Taiwan). The fixed end of the beam is excited by a shaker (Bruel & Kjaer 4809), and the shaker-driving signal is generated by a DAQ card (NI USB-6259 from National Instrument, Austin USA) on a notebook computer. A vibrometer (LK-G3001P+LK-G32

from Keyence, Osaka Japan) is used to measure the beam tip displacement, and an accelerometer (Brüel & Kjaer 4381 from Brüel & Kjær Sound & Vibration Measurement A/S, Nærum Denmark) is used to measure the acceleration at the fixed end. The piezoelectric voltage, the displacement and the acceleration are recorded by the DAQ card. The dimensions of the cantilever beam and the piezoelectric patches are shown in Table 6-2. The component measured values and model parameters are shown in Table 6-3. The first natural frequency of the cantilever beam is 34Hz. The dimension and the clamped capacitance of the main piezoelectric patch are much greater than those of the two small piezoelectric patches.

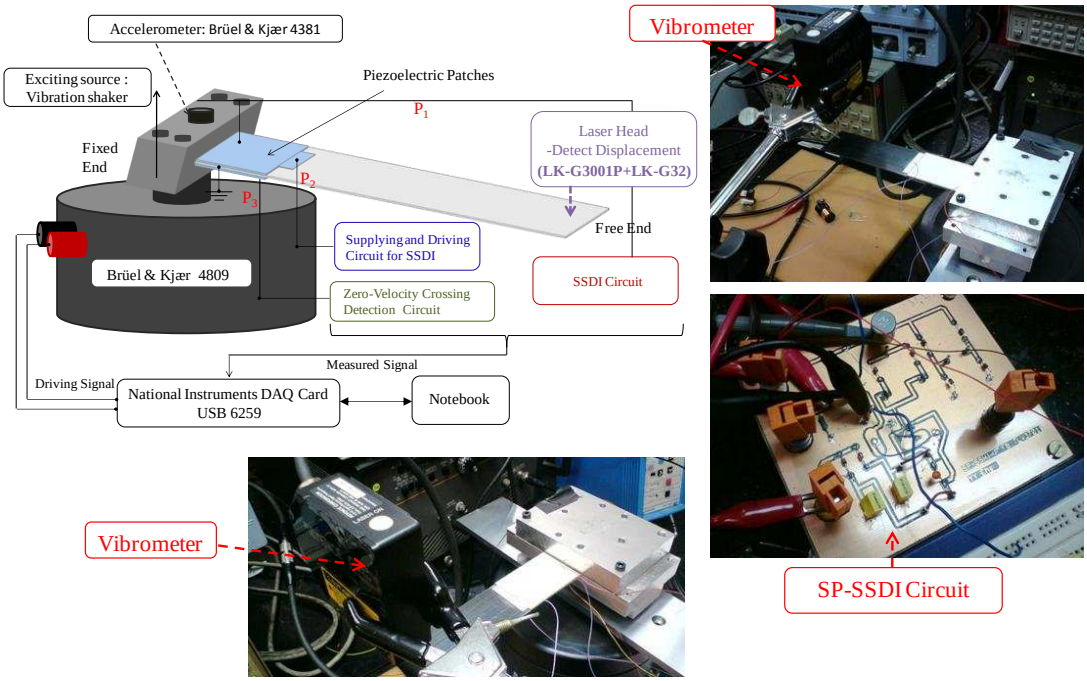

Figure 6-7. Experimental setup and pictures.

Table 6-2. Dimensions of the piezoelectric patches.

Steel Beam	Length×Width×Thickness	140mm×35mm×0.5mm
Piezoelectric Patchches	P_1	50mm×65.5mm×0.6mm
	P_2	30mm×5mm×0.5mm
	P_3	50mm×4.5mm×0.6mm

Table 6-3. Component values and model parameters.

Symbol	Description	Value (unit)
f_{op}	Open circuit resonant frequency when all piezoelectric patch is in open circuit	34 Hz
f_{sh}	Short circuit resonant frequency when all piezoelectric patch is in short circuit	33.97Hz
k^2	Electromechanical courpling coefficient	0.0018
ζ	Damping ratio	0.02
Q_M	Mechanical quality factor	2.09
M	Mass	28 g
K^E	Equivalent stiffness when all piezoelectric patch is in short circuit	1276 N/m
K^D	Equivalent stiffness when all piezoelectric patch is in open circuit	1278 N/m
D	Damping coefficient	0.24 N/m/s
α^{P1}	Force-voltage factor of P_1	0.000368 N/V
α^{P2}	Force-voltage factor of P_2	0.0000242 N/V
α^{P3}	Force-voltage factor of P_3	0.0000227 N/V
Q_{LC}	Quality factor of resonant L-CP_1	4.4
R	Equivalent resistor of resonant L-CP_1	0.48 Ω
q_{LC}	Inversion factor	0.7
C_{P1}	Clamped capacitance of P_1	67.6 nF

C_{P2}	Clamped capacitance of P_2	4.44 nF
C_{P3}	Clamped capacitance of P_3	4.16 nF
L	Resonant inductor in SSDI	10 mH
C_r	Regular capacitor in supply circuit	4.7 uF
C_P	Regular capacitor in supply circuit	2.2 uF
C_N	Regular capacitor in supply circuit	2.2 uF
D_Z	Zener diode in supply circuit	15 V
L_f	Low pass filter inductor in zero velocity crossing detector	700 mH
C_f	Low pass filter capacitor in zero velocity crossing detector	470 nF

6.4.2 Experimental results

Experimental data were taken to validate the self-powered velocity-synchronized semi-passive system presented in this sub-section and to demonstrate the operation of the circuit.

Figure 6-8 shows the displacement, the sensed velocity, the switching signal and the piezoelectric voltage of uncontrolled and self-powered SSDI systems for acceleration of 0.16m/s^2. Comparing the results with and without the SSDI system active, the tip displacement is reduced from approximately 1.12mm to 0.72mm by the SSDI damping effect. Because the current-sensing resistance of 1kΩ is much lower than

the output impedance of the piezoelectric patch (around 1.05MΩ), the signal is very small, with a peak value of approximately 0.01V. When SSDI is active, the high frequency noise is easily introduced into the velocity control signal, but it does not influence the power supply effectiveness because the capacitors in the rectifier regulate the supplied voltage.

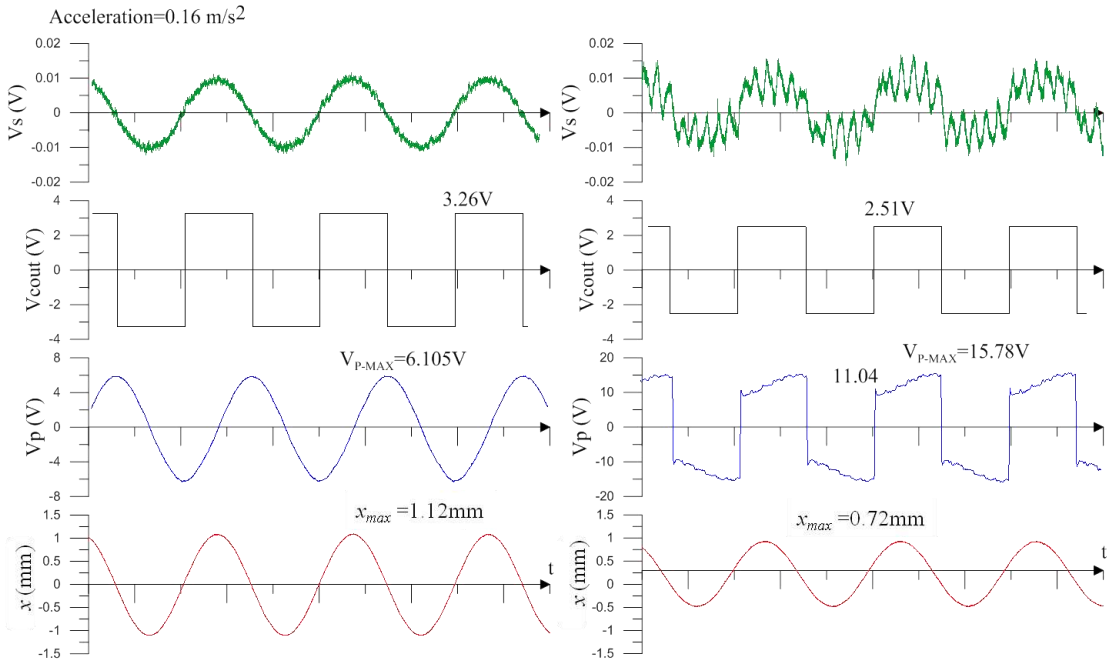

Figure 6-8. Experimental results of the zero-velocity crossing detection circuit (a) without SSDI active and (b) with SSDI active (green trace: velocity V_S, black trace: V_{Cout}, blue curve: piezoelectric voltage V_P, and red trace: beam tip displacement x).

The operating limit of the self-powered technique is obtained when the voltage V_{CC} is lower than 2.5V. Once the SSDI circuit works, the decrease of the vibration

magnitude leads to a decrease in terms of harvested power and thus leads to a decrease of voltage V_{CC}. Therefore there is a minimum value of the displacement magnitude. Figure 6-8 we can see that the DC voltage V_{CC} is equal to 3.26 V when the displacement magnitude is 1.12 mm, and 2.51 V for a displacement of 0.72 mm. The experimental limit of the system is 0.7 mm to have V_{CC} greater than 2.5V to power the comparator in the circuit. Figure 6-9 shows the theoretical and experimental value of V_{CC} as a function of displacement.

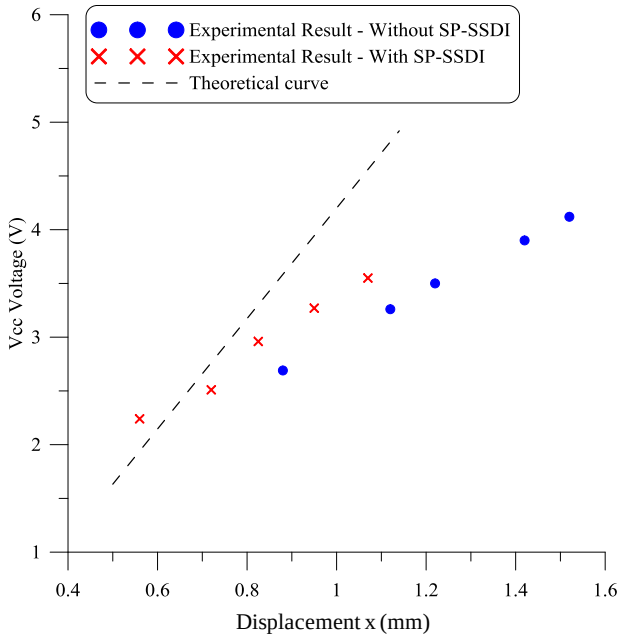

Figure 6-9. Voltage VCC as a function of displacement x.

This minimum value of the displacement magnitude can be set by the size of the

piezoelectric patch P_2. If we consider the thickness is fixed and vary the width, equation(6.5) can be used to predict the minimal displacement magnitude required for the corresponding width. The theoretical minimum value of magnitude of displacement as a function of the width is therefore plotted in Figure 6-10 for thickness, t=0.5mm, and length l=30mm. Figure 6-10 shows that for a width w=5 mm, the theoretical value of the displacement magnitude is 0.7 mm.

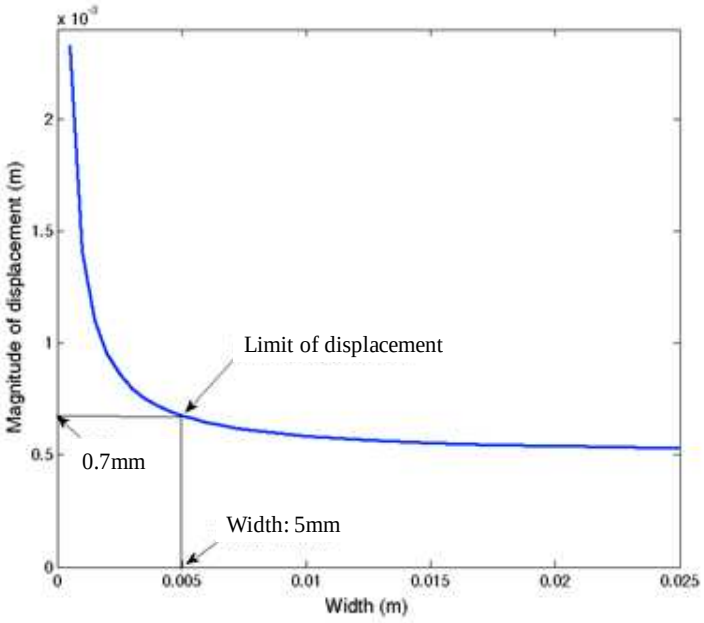

Figure 6-10. Minimum value of displacement magnitude as a function of width of piezoelectric-patch P_2.

6.4.3 Comparison

For comparison, experiments were carried out in four different cases; these cases

are listed in Table 6-4.

Table 6-4. Four experimental cases.

	Piezoelectric patches	Conditions
case 1	Uncontrolled	
case 2	$P_1+P_2+P_3$	External energy: Power supply Optimal switching point: Function generator
case 3	P_1	External energy: Power supply Optimal switching point: Function generator
case 4	P_1	No External energy. Using self-powered supplying circuit. Switching point: Velocity control cirucit.

- Case 1 is the reference case, used to show the undamped situation. The piezoelectric voltage is in phase with the tip displacement and has a phase lag of approximately 90 degrees with respect to the velocity signal.

- Case 2 is the maximal damping condition. All three piezoelectric patches ($P_1+P_2+P_3$) are controlled using the SSDI damping technique, and the SSDI is operated by external instruments. The power source is an external DC power supply, and the optimal switching signal is provided by a function generator.

- Case 3 provides an experimental control for comparison with case 4. In case 3, only one piezoelectric patch (P_1) is controlled using the SSDI damping technique. The power source is an external DC power supply, and a function generator provides the switching signal.

- Case 4 is the experimental condition and uses the self-powered technique (SP-SSDI) presented in this chapter without any external instruments.

The following two subsections will compare the damping performance of each of the cases when the beam is driven at different excitation levels. The results will be compared in both the time domain and the frequency domain.

6.4.3.1 Time domain comparison

The cantilever beam is driven at its first natural frequency (34Hz) at different accelerations. Figure 6-11 and Figure 6-12 show the experimental results of the displacement and the work cycles calculated for the 4 cases for acceleration of 0.13m/s^2 and 0.16m/s^2, respectively. To quantify the performances of damping technique, the force-displacement diagram (work-cycle) is employed to illustrate the energy conversion cycle. In the case of a purely capacitive load on the piezoelectric patch (case 1), the displacement and voltage are in phase; the area of the cycle is null, so the extracted energy is equal to zero. When the SSDI technique is active, the LC_0 resonance circuit increases the magnitude of voltage V_P and decreases the displacement x. The area of the cycle is the extracted energy. Case 2 is the most effective one because all piezoelectric patches are used for the damping control with SSDI technique. This is the

ideal experimental case because the SSDI circuit is powered by external power supply. If we compare case 3 (external drive) and case 4 (self-powered), we obtain a good evaluation of the zero velocity crossing detection technique (same area of piezoelectric patches with SSDI). For an acceleration of 0.13m/s^2; the self-powered SSDI circuit damps the structure only up to 0.7mm (0.5mm for the case with external supply) due to the limit of operation of the comparator For the acceleration of 0.16m/s^2 and higher, the results show that the amplitude of voltage and displacement are in phase, which means that with the proposed technique the switching occurs at nearly the optimal time. The little difference is due to the high frequency noise in the velocity sense signal.

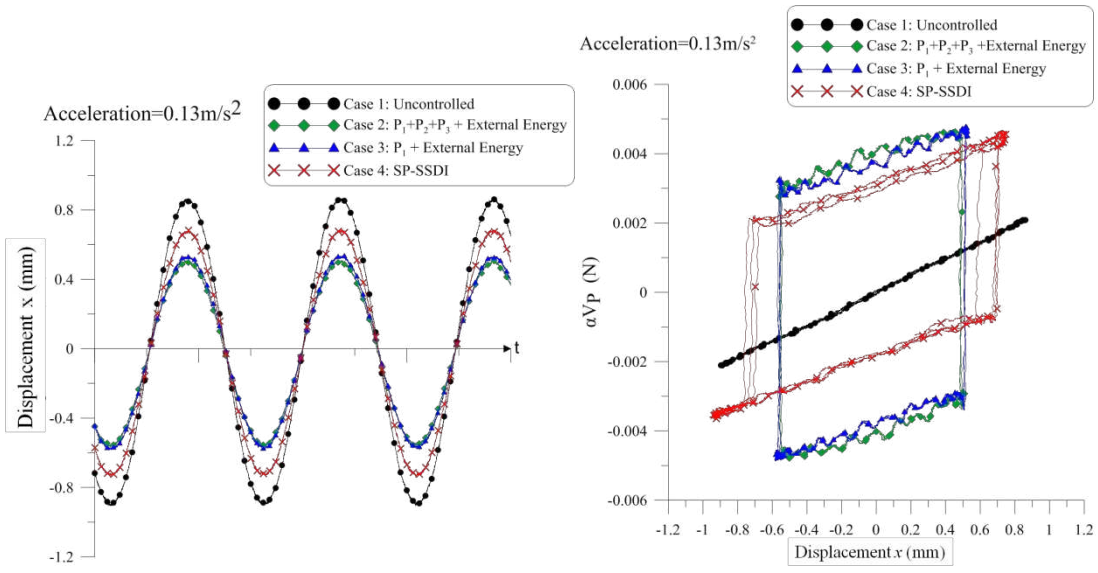

Figure 6-11. Experimental results (acceleration=0.13m/s^2) (a) displacement (b) work-cycle.

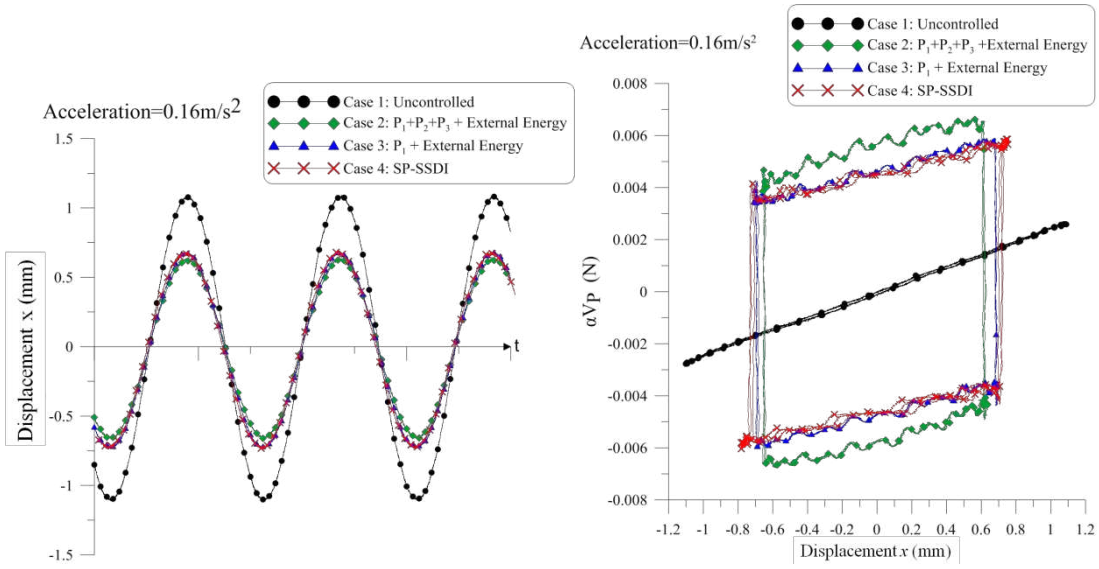

Figure 6-12. Experimental results (acceleration=0.16m/s^2) (a) displacement (b) work-cycle.

Figure 6-13 shows the experimental results and theoretical value of the displacement magnitude as a function of acceleration. The self-powered technique operates successfully for acceleration higher than 0.16m/s^2. For a lower acceleration, the damped displacement is kept at 0.7mm until the uncontrolled displacement is higher than 0.7mm. The system behaves like a feedback control loop; SSDI decrease displacement but when the displacement is lower than 0.7mm, the comparator stop to work and the displacement increases again.

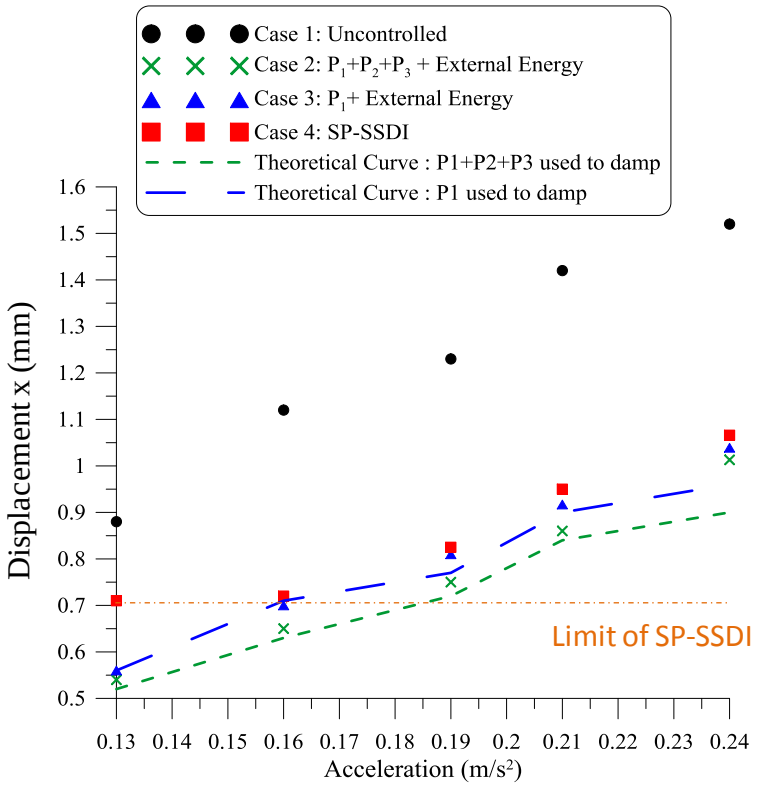

Figure 6-13. Displacement magnitude as a function of acceleration.

Table 6-5 summarizes the experimental results for 4 accelerations: 0.16m/s^2, 0.19m/s^2, 0.21m/s^2 and 0.24m/s^2. The tip displacement increases as the imposed acceleration increases. Two measures of efficiency are proposed and defined in equations(6.6) and equation(6.7); there are presented in Table 6-5. The first efficiency compares the self-powered technique with velocity control, called SP-SSDI here to the use of all of the piezoelectric patches (P_1+P_2+P_3) for SSDI damping. From Table 6-5, the average efficiency is approximately 86%. This result means that if the size of the

piezoelectric patches used in the system is not increased, the proposed SP-VSSDI technique provides approximately 14% less damping. The second efficiency compares the SP-VSSDI technique to the case in which only the P_1 patch is used for SSDI, and the patch is controlled with an external function generator with perfect timing and powered by external power sources. This measure provides a fairer comparison because the area of the piezoelectric patch used for the SSDI is the same as that used for the self-powered system. From Table 6-5, the average of this efficiency measure is approximately 95%. This means that the phase lag generated by the inherent structure and the passive low-pass filter degrades the damping performance by approximately 5%. Based on the two comparisons, the SP-SSDI technique demonstrates high efficiency and good damping ability while maintaining a fully self-powered system.

Table 6-5. Experimental results for different excitation levels.

Acceleration (m/s^2)	Tip Displacement(mm)				Efficiency[1](%)	Efficiency[2](%)
	Case 1: Uncontrolled	Case 2: P1+P2+P3	Case 3: P1	Case 4: SP-SSDI		
0.16	1.12	0.65	0.7	0.72	85.11	95.24
0.19	1.23	0.75	0.81	0.825	84.38	96.43
0.21	1.42	0.86	0.917	0.95	83.93	93.44
0.24	1.52	1.013	1.039	1.066	89.55	94.39
				Average	85.74	94.87

$$\text{Efficiency}\_1 = \frac{\text{Uncontrolled} - [\text{Self} - \text{powered}]}{\text{Uncontrolled} - [P_1 + P_2 + P_3]} \tag{6.6}$$

$$\text{Efficiency}\_1 = \frac{\text{Uncontrolled} - [\text{Self} - \text{powered}]}{\text{Uncontrolled} - [P_1]} \tag{6.7}$$

Figure 14 shows the experimental results in the time domain at acceleration of $0.19 m/s^2$. The results show that when the SP-SSDI system starts to take effect, the tip displacement decreases rapidly, and the piezoelectric terminal voltage increases rapidly. The results also demonstrate that the SP-SSDI system provides good, stable damping during the period when it is active. The SSDI damping effect is not influenced when the self-powered system is active.

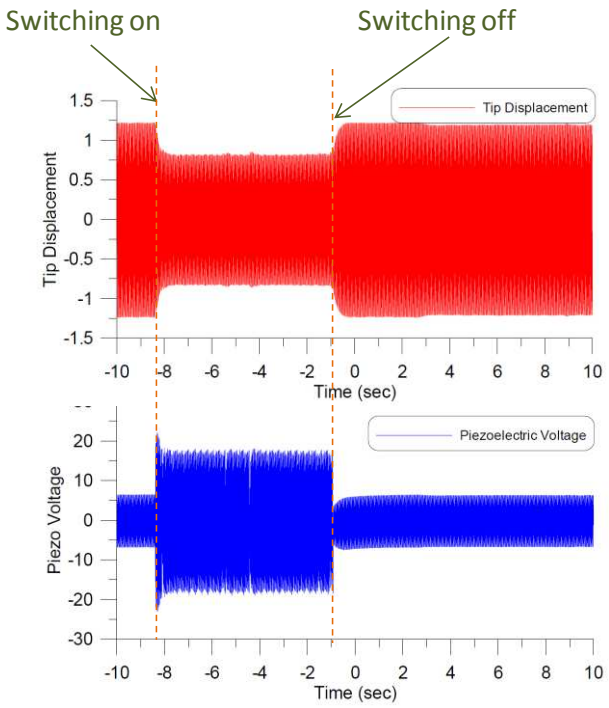

Figure 6-14. Experimental results in the time domain of the self-powered technique.

6.4.3.2 Frequency response

Figure 6-15 shows, the frequency responses of the system for the 4 cases and for acceleration of 0.13m/s^2, 0.16m/s^2, 0.21m/s^2, and 0.24m/s^2. The testing frequency ranges from 28Hz to 40Hz. For an acceleration of 0.13m/s^2, we can see clearly the limit of the system; the SSDI circuit dumps the structure only up to 0.7mm, it is not plenty effective. As we say, the system works like a feedback control loop and regulates displacement at 0.7mm. When the uncontrolled displacement is lower than 0.7 mm the SSDI is not active. The acceleration of 0.16m/s^2 is the limit case; the damped displacement is 0.7mm with self-power technique (case 4) and with external supply (case 3), but the bandwidth is smaller with self-powered technique (2Hz). For the acceleration of 0.21m/s2, and 0.24m/s2, the self-powered technique provides almost the same damping ability as the case in which the P_1 patch is controlled with external instruments. The working bandwidth of the self-powered system is approximately 3.5 Hz at 0.21m/s^2 acceleration, and 3.5Hz at 0.24m/s^2 acceleration. Compared to the cases in which the P_1+P_2+P_3 patches and the P_1 patch are driven by external instruments (with working bandwidths of approximately 5Hz and 6Hz, respectively), the self-powered technique does not provide as much damping. Consequently, when the exciting acceleration is low, the working bandwidth is small. However, when the

exciting acceleration is sufficiently high, the working bandwidth is almost the same as when external instruments are used.

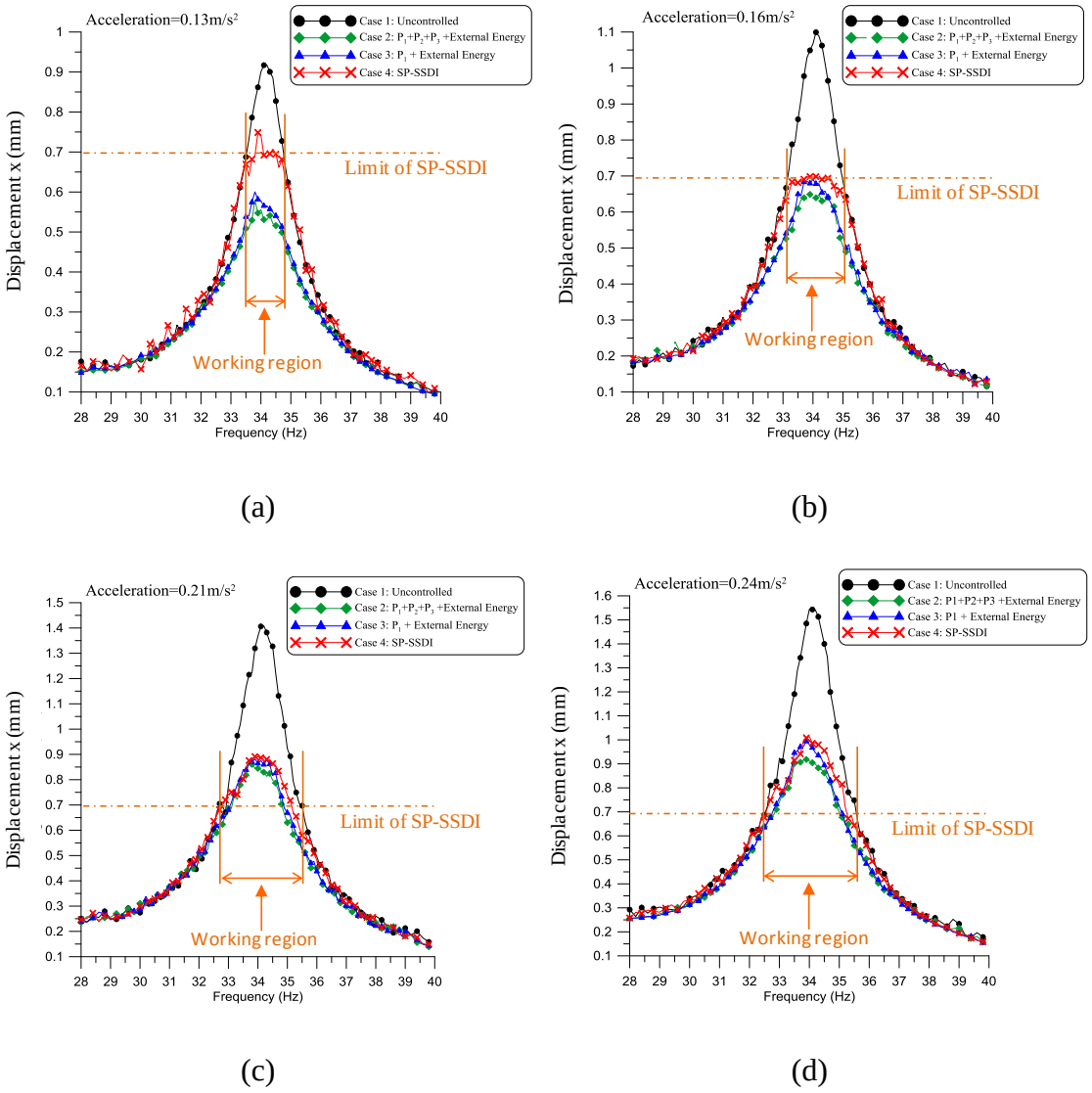

Figure 6-15. Experimental frequency response results: (a) acceleration=0.13 m/s^2, (b) acceleration=0.16 m/s^2, (c) acceleration=0.21 m/s^2, and (d) acceleration=0.24 m/s^2.

6.5 Conclusion

In this chapter, a self-powered SSDI technique based on zero-velocity crossing detection is proposed. The control signal used to drive the switches is obtained by sensing the velocity signal. This technique makes the semi-passive damping technique SSDI become the passive damping technique. The system concept is to divide the piezoelectric patch into three parts. The largest part behaves like the conventional piezoelectric patch used in the SSDI technique to dissipate the vibration energy. The second piezoelectric patch is a smaller patch that works like energy harvesting device to provide the power supply circuit. The third piezoelectric patch is a smaller patch designed to sense the velocity and to generate driving signal to control the switches. Because the three components are designed individually, each can be analyzed and optimized separately. Compared to the case in which all of the piezoelectric patches ($P_1+P_2+P_3$) are used for structural damping and driven by an external function generator and a power supply, the efficiency of the proposed self-powered system is approximately 86%. Compared to the ideal switching case in which only the main piezoelectric patch is used for SSDI damping and is driven by an external function generator and power supply, the efficiency of the proposed self-powered system is approximately 95%. The major advantage of the proposed technique is that it is only

necessary to sacrifice a small amount of damping performance to make the system fully self-powered. The circuit design and the implementation of the system are quite simple, and the study shows the effectiveness of this new design. The drawback of this technique is the narrow bandwidth in the frequency response for low excitation level due to the decrease of harvested energy when the SSDI circuit works. When the exciting acceleration is sufficiently high, the working bandwidth is nearly equal to the bandwidth of the system driven by external instruments. To improve the system performance, the high frequency noise generated by the inversion could be further processed; the damping performance and efficiency of the self-powered system could also be improved.

Chapter 7 Summary and Discussion

The main topic of this dissertation is about improving the output power of the piezoelectric energy harvesting device. The objective was to build a totally self-powered energy harvester and to broaden the bandwidth of the frequency response. Because the interfaces used in energy harvesting application are similar to ones used in damping applications, the self-powered technique was applied in the damping system. According to different techniques proposed in this dissertation, Figure 7-1 shows a schematic diagram of our contribution to enhance the performances of the piezoelectric energy harvester.

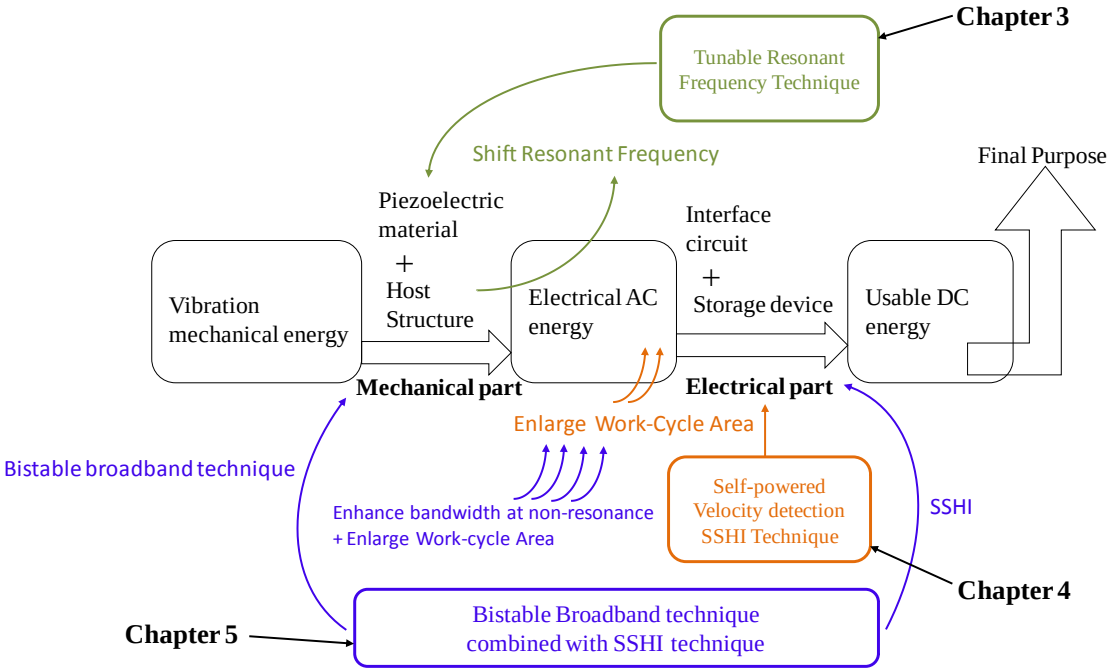

Figure 7-1. Schematic diagram of different techniques improving the power output of the piezoelectric energy harvesting device.

7.1 Summary and conclusion of the major results

The techniques proposed in this dissertation can be summarized as follows.

1. Tunable resonant frequency piezoelectric energy harvesting system

The tunable resonant frequency technique is based on the characteristic of the piezoelectric material and shifts the resonant frequency in a short region by connecting the piezo-patch to different capacitors in the electrical part and then influences the behavior in the mechanical part. Finally the resonant region can be broadened around 2.5 Hz in the experimental results.

Because this technique is performed through changing the loads in the electrical part to influence the mechanical behavior, the electromechanical parameter k^2Q_m must be at least close to the medium coupling region. When the electromechanical parameter k^2Q_m is much lower than 2 is in the weak-coupling region and in our experiment in chapter 3 the $k^2Q_m = 1.25$ is in the medium-coupling region, that is why the tunable resonant frequency technique can shift the resonant frequency.

In the results of the tunable resonant frequency energy harvesting device, the maximal output power can be increased around 30 % and the charging time can be shortened to around 200s. The tunable resonant frequency system is successfully combined with the a WSN node to transmit the RF signal. The tunable system can make

a WSN node transmit more RF data during the same time period.

2. Self-powered velocity detection SSHI energy harvesting system:

Due to the success of the SSHI technique improving the output power for the piezoelectric energy harvesting device, the main contribution in this dissertation is to make the SSHI technique into a fully self-powered system through the velocity detection to switch more accurately than classical peak detector technique. The energy flows are separated into three parts so it can be designed respectively. The velocity signal is detected from the characteristic of the piezoelectric patch and it can theoretically make switches work at the optimal time.

The SSHI techniques achieve good performance over standard techniques when the harvester is weakly coupled. In this case the electromechanical parameter k^2Q_m is much lower than 2. The self-powered V-SSHI increases the output power by enlarging the work-cycle area. From the results, the self-powered V-SSHI can lead to a gain of around 200% compared to the standard DC approach without any external energy and have better performance than using peak detector technique.

3. Bistable broadband technique combined synchronized switching technique:

In order to harvest the vibration energy over a broader frequency range than that of the traditional linear beam harvester we proposed a bistable harvester. This bistable

harvester was combined with synchronized switching technique. The bistable broadband technique enhances the bandwidth and makes mechanical behavior nonlinear through proper magnets design in the mechanical part. The classical SSHI technique enlarges the work-cycle area in the electrical part and is combined with bistable broadband technique to construct a complete system.

From the results of our example, at resonance (f = 10.4 Hz) the output power of the bistable broadband technique combined with SSHI is 140.4 μW and the output power of the bistable broadband combined with standard DC technique is 24.86 μW. The output power is increased around 5.64 times at resonance. At non-resonance (f = 5Hz) the output power of the bistable broadband technique combined with SSHI is 8μW and the output power of the bistable broadband combined with standard DC technique is 0.3 μW. The output power is increased around 26.67 times at non-resonance.

The greatest advantage of combining these two non-linear techniques is that they can be designed individually and will not influence each other. The performance of the bistable broadband technique and the SSHI technique are integrated together.

4. Self-Powered Semi-Passive Piezoelectric Structural Damping Based on Zero-Velocity Crossing Detection

When the piezoelectric patch is not weakly coupled to the host structure, the

piezoelectric energy harvester will produce damping effects. Based on this characteristic, the self-powered synchronized switching technique used in the energy harvesting application can be also used in the structural damping application. The advantage of the self-powered technique is that it can fully perform in damping application but the limit of the self-powered damping technique is that this method needs a minimum structure's displacement to harvest energy to supply electronic devices. As the structure's displacement is the key parameter for the self-powered technique, in the damping application the system behaves like a feedback loop when the displacement is over the limit level, the self-powered semi-passive damping system will start to damp the structural vibration effectively. Compared to the case when the electronics are supplied with an external source, the efficiency of the proposed self-powered semi-passive damping system is approximately 86 %. Compared to the ideal switching case in which only the main piezoelectric patch used for SSDI damping with external source, the efficiency of the proposed self-powered semi-passive damping system is approximately 95 %. The major advantage of the this technique is that it is only necessary to sacrifice a small amount of damping performance to make the system fully self-powered and also make the system also have good damping performance.

7.2 Future work

The most important points in the future are maintaining the increase of the output power of energy harvesting and these techniques must be really combined with WSN modules or other low power consumption portable devices. The following points are the possible ways to increase the output power, increase efficiency and combined with WSN system.

1. Piezoelectric material is the fundamental part to convert the energy. As the properties of the single crystal piezoelectric material is better than PZT, substituting the single crystal piezoelectric material for PZT is a potential method to increase energy directly.

2. Design the proper interface circuit for capacitive load. The interface circuit designed in this dissertation is suitable for the resistor load. However if in the application the electrical energy does not supply to the load directly, the capacitor is needed to be the buffer to store the energy temporarily.

3. Design a better and proper WSN communication framework for piezoelectric energy harvesting device. According to the different applications, the WSN communication framework should be designed and developed as an exclusive system to make piezoelectric energy harvesting device efficiently extend the battery lifetime.

Appendix A.

A.1 Equivalent circuit of the piezoelectric energy harvester

In order to analyze and discuss the piezoelectric energy harvesting device with the interfacing circuit, the equivalent circuit of the piezoelectric energy harvesting is presented. From the governing equation of piezoelectric (equation (2.6)), the equivalent circuit of mechanical part and electrical part can be modeled and separated by an ideal transformer and the ratio of the transformer is force-voltage coupling factor (α) as shown in Figure A-1. The equivalent inductor L_m is given by equivalent mass, the equivalent capacitor C_m is given by equivalent stiffness $1/K^E$ and the equivalent resistor R_m is given by damping ratio D.

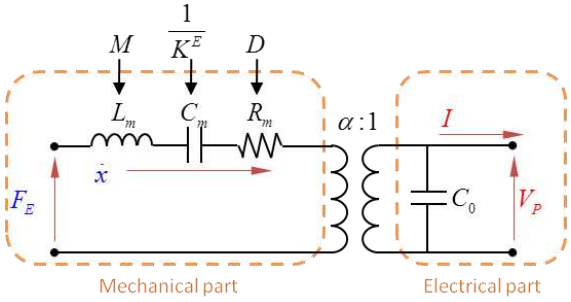

Figure A-1. Equivalent circuit model of piezoelectric and structure.

The mechanical part of the equivalent circuit can be transformed into electrical part as Figure A-2 shown. V_{eq} and I_{eq} is the equivalent voltage and current which transformed from the mechanical part. Figure A-2 is the equivalent circuit of the

piezoelectric energy harvesting device and can be used to analyze with the interfacing circuit. The impedance of the mechanical part is shown in equation (8.1).

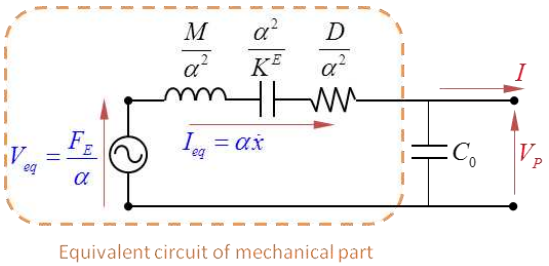

Figure A-2. Equivalent circuit model transformed into electrical part.

$$Z_{mech} = j\omega\frac{M}{\alpha^2} + \frac{K^E}{j\omega\alpha^2} + \frac{D}{\alpha^2} \tag{8.1}$$

A.2 Electromechanical coupling coefficient

Electromechanical coupling coefficient (EMCC) is another important parameter and it indicates the effectiveness of piezoelectric materials to convert the mechanical energy into electrical energy. EMCC can be presented as equation (8.2) [95]. This equation is general formula and suitable for both dynamic and static condition. In the real application, it's hard and complex to measure energy and put it into equation (8.2) to calculate the EMCC. So when the structure driving at the resonance, the equation (8.2) can be extended as equation (8.3) shown [95, 96] and this EMCC is called effective electromechanical coupling coefficient (k_{eff}^2). Effective electromechanical coupling

coefficient (k_{eff}^2) can be given by open-circuit resonant frequency and short-circuit resonant frequency as following equations (8.3) shows.

$$k_s = \frac{U_m}{\sqrt{U_d U_d}} \tag{8.2}$$

Where

Table A-1. Definitions of the EMCC energy terms.

Elastic energy	U_e
Electric energy	U_m
Mutual energy	U_e

$$k_{eff}^2 = \frac{\omega_D^2 - \omega_E^2}{\omega_D^2} \tag{8.3}$$

where

Open-circuit resonant frequency	ω_D
Short-circuit resonant frequency	ω_E

The effective electromechanical coefficient shown in equation (8.3) is dynamic definition. According to the static definition of open-circuit resonant frequency and short-circuit resonant as equation (8.4) shown, the static electromechanical coupling coefficient (k^2) can be represented in open-circuit stiffness and short-circuit stiffness as equation (8.5) shown and it's also called global electromechanical coupling coefficient

(k^2).

$$\omega_D = \sqrt{\frac{K_p^D}{M}}, \quad \omega_E = \sqrt{\frac{K_p^E}{M}} \tag{8.4}$$

$$k^2 = \frac{K_p^D - K_p^E}{K_p^D} \tag{8.5}$$

where

Effective mass	M
Effective open-circuit stiffness	K_p^D
Effective short-circuit stiffness	K_p^E

The effective open-circuit stiffness (K_p^E) can be calculated by the piezoelectric equation when the piezoelectric patch is in short-circuit condition as equation (8.6). When the piezoelectric patch is in short-circuit condition, there is no piezoelectric effect and the piezoelectric material like only a normal ceramic. In order to calculate the effective open-circuit stiffness (K_p^D), let the piezoelectric patch in open-circuit condition and it means there is no current flow out from piezoelectric patch. The output current (I) in piezoelectric equation is zero and substitute the relation between velocity and voltage into the governing equation (2.4). Open-circuit stiffness (K_p^D) can be obtained as equation (8.7). When the piezoelectric patch is driving under low-coupled condition and small displacement, the displacement can be assumed constant ($x = x'$). x represents the displacement when the system is driven under open-circuit condition and x' represents

the displacement when the system is driven under short-circuit condition. The relation between effective open-circuit stiffness (K_p^D) and effective open-circuit stiffness (K_p^E) can be expressed as equation (8.8).

$$F_P = K_p^E \cdot x \tag{8.6}$$

$$F_P = \left(K_p^D + \frac{\alpha^2}{C_0} \right) x' \tag{8.7}$$

$$K_p^D = K_p^E + \frac{\alpha^2}{C_0} \tag{8.8}$$

A.3 Time interval discussion of Standard DC approach

In this sub-section, the time interval behavior of the standard DC approach is discussed. It is assumed that the displacement is sinusoidal and the displacement x, velocity $\dot{x}$, equivalent current I_{eq} can be represented as equation (8.9), (8.10) and (8.11).

$$x(t) = -\hat{x}\cos(\omega_0 t) \tag{8.9}$$

$$\dot{x}(t) = \omega_0 \hat{x}\sin(\omega_0 t) = \hat{\dot{x}}\sin(\omega_0 t) \tag{8.10}$$

$$I_{eq}(t) = \alpha \dot{x} = \alpha\omega_0 \hat{x}\sin(\omega t) = \hat{I}_{eq}\sin(\omega_0 t) \tag{8.11}$$

where

$$\begin{cases} \dot{\hat{x}} = \omega_0 \hat{x} \\ \hat{I}_{eq} = \alpha\omega_0 \hat{x} \end{cases}$$

According to the Figure 2-11, the time when V_P equals $-\hat{V}_C$, x equals $-\hat{x}$ and I_{eq} equals zero is T_1, the time when V_P reaches to the $\hat{V}_C$ is T_2 and the time when x equals $\hat{x}$ is T_3. The behavior of these three time intervals is discussed in detail as following.

(i) $t = T_1 \sim T_2$

As $V_C < \left\|\hat{V}_C\right\|$, the full bridge rectifier is disconnected and I_R, I_P flow into R and C_0 respectively as equation (8.12) shown. Integrating the second equation in equation (8.12) from T_1 to T_2, the time T_2 can be obtained as equation (27) shown.

$$\begin{cases} I_R = -I_C \\ I_P = \alpha\dot{x} - C_0\dot{V}_C = 0 \end{cases} \tag{8.12}$$

$$\begin{aligned} &\int_{T_1}^{T_2} \dot{V}_C dt = \frac{\alpha}{C_o}\int_{T_1}^{T_2} \dot{x} dt \\ &\Rightarrow T_2 = \frac{1}{\omega_0}\cos^{-1}\left(\frac{2C_0}{\hat{x}\alpha}\hat{V}_C - 1\right) \end{aligned} \tag{8.13}$$

(ii) $t = T_2 \sim T_3$

The voltage V_P reaches to the $\hat{V}_C$, so the full bridge rectifier is connected. I_P

equals $I_C + I_R$ and flow through full bridge to into the rectifier capacitor C_r and load resistor R as equation (8.14) shown.

$$I_P = I_C + I_R \tag{8.14}$$

(iii) $t = T_1 \sim T_3$

Considering half cycle period (the time interval from T_1 to T_3) and assuming the rectified capacitor C_r of load is large enough, so the output voltage V_C during the time interval form T_1 to T_3 can be regarded as a constant value and the net current through C_r equals zero. As this assumption, the sum of the current output I_p from piezoelectric patch equals to the sum of the current I_R flow through the resistor load R as equation (8.15) shown. Integrating over the half cycle from time T_1 to T_3, the output voltage $\hat{V}_C$ can be obtain as the equation (8.16) shown.

$$\int_{T_1}^{T_3} I_R dt = \int_{T_1}^{T_3} I_P dt \tag{8.15}$$

$$\begin{aligned} &\int_{T_1}^{T_3} \frac{\hat{V}_C}{R} dt = \int_{T_1}^{T_3} \left(\alpha \dot{x} - C_0 \dot{V}_C \right) dt \\ &\Rightarrow \hat{V}_C = \frac{2\alpha R\omega_0}{2C_0 R\omega_0 + \pi} \hat{x} \end{aligned} \tag{8.16}$$

A.4 Time interval discussion of Parallel-SSHI

In this sub-section, the time interval behavior of the parallel-SSHI is presented.

According to the Figure 2-15, the time when V_P equals $-\hat{V}_C$, x equals $-\hat{x}$ and I_{eq} equals zero is T_1. Let T_1 is initial time and equals zero. The time when the clamped capacitor C_0 and inductor L is resonant during half resonant cycle and V_P reaches to the $\hat{V}_C \cdot q_{LC}$ is T_2 . T_2 equals $\frac{1}{2}T_{LC}$. $q_{LC} = e^{-\frac{\pi}{2Q_I}}$ is the inverting quality factor of the LC resonance and the Q_I is quality factor of whole energy harvesting device and equals $\omega_{LC} L / R_{LC}$. The R_{LC} in the Q_I can be regarded as whole electrical losses in the system. The time when V_P reaches to $\hat{V}_C$ is T_3 and the time when x equals $\hat{x}$ is T_4. The behavior of the these time interval is discussed in detail as following.

(i) $t \in [T_1, T_2]$

The time interval from T_1 to T_2 equals to the half LC resonant period ($\frac{1}{2}T_{LC}$). In this interval the inductor will resonate with the clamped capacitor of the piezoelectric patch and the terminal voltage of piezoelectric patch reverses from the negative voltage to positive voltage. The terminal voltage of the piezoelectric patch can be expressed as equation (8.17) shown during oscillating period. Substitute the $t = \frac{T_{LC}}{2}$ into the equation (8.17) and the terminal voltage at time T_2 can be obtained as equation (8.18).

$$V_P(t) = \hat{V}_P \cdot e^{-\frac{\omega_{LC}}{2Q_I}t}\left[\frac{1}{2Q_I}\sin(\omega_{LC}t) + \cos(\omega_{LC}t)\right] \qquad (8.17)$$

$$V_P(T_2) = -\hat{V}_C \cdot e^{-\frac{\omega_{LC}}{2Q_I}\cdot\frac{\pi}{\omega_{LC}}}\left[\frac{1}{2Q_I}\sin\left(\omega_{LC}\cdot\frac{\pi}{\omega_{LC}}\right)+\cos\left(\omega_{LC}\cdot\frac{\pi}{\omega_{LC}}\right)\right] \quad (8.18)$$
$$= \hat{V}_C \cdot e^{-\frac{\pi}{2Q_I}} = \hat{V}_C \cdot q_{LC}$$

(ii) $t \in [T_1, T_3]$

As $V_C < \|\hat{V}_C\|$, the full-bridge rectifier is disconnected and I_R and I_T can be represented as equation (8.19) shown. Integrating the piezoelectric equation from T_1 to T_3, the time T_3 can be obtained as equation (8.20) shown.

$$\begin{cases} I_R = -I_C \\ I_T = I_P + I_L = \alpha\dot{x} - C_0\dot{V}_C + I_L = 0 \end{cases} \quad (8.19)$$

$$\int_{T_1}^{T_3}\left(\alpha\dot{x} - C_0\dot{V}_P + I_L\right)dt$$
$$\Rightarrow T_3 = \frac{1}{\omega_0}\cos^{-1}\left[\frac{C_0}{\hat{x}\alpha}\left(1-q_{LC}\right)\hat{V}_C - 1\right] \quad (8.20)$$

(iii) $t \in [T_3, T_4]$

The voltage V_P reaches to the $\hat{V}_C$, so the full-bridge rectifier is connected. I_T equals $I_C + I_R$ and flow through full-bridge to into the rectifier capacitor C_r and load resistor R as equation (39) shown.

$$I_R = I_T - I_C = I_P + I_L - I_C \tag{8.21}$$

(iv) $t \in [T_1, T_4]$

Assuming the rectified capacitor C_r of the load is large enough, so the output voltage V_C during the time interval form T_1 to T_3 can be regarded as a constant value and the net current through C_r equals zero. As this assumption, the sum of the current output I_p from piezoelectric patch equals to the sum of the current I_R flow through the resistor load R as equation (8.22) shown. When integrate the current I_R from the time T_1 to T_4, the $\hat{V}_C$ can be obtained and the result is shown in equation (8.23).

$$I_R = I_P + I_L \tag{8.22}$$

$$\begin{aligned} &\int_{T_1}^{T_4} \frac{\hat{V}_C}{R} dt = \int_{T_1}^{T_4} \left(\alpha \dot{x} - C_0 \dot{V}_C + I_L \right) dt \\ &\Rightarrow \hat{V}_C = \frac{2\alpha R \omega_0}{\pi + (1 - q_{LC}) C_0 R \omega_0} \hat{x} \end{aligned} \tag{8.23}$$

A.5 Time interval discussion of Series-SSHI

In this sub-section, the time interval behavior of the series-SSHI is presented. According to Figure 2-19, the time when V_P equals $-\hat{V}_P$, x equals $-\hat{x}$ and I_{eq} equals zero is T_1. Let T_1 is initial time and equals zero. The time when the clamped capacitor C_0 and inductor L is resonant during half resonant cycle and V_P reaches

to the $-\hat{V}_C + \left(\hat{V}_P - \hat{V}_C\right) \cdot q_{LC}$ is T_2 . T_2 equals $\frac{T_{LC}}{2}$ and $x(T_2) \approx x(T_1) = -\hat{x}$. $q_{LC} = e^{-\frac{\pi}{2Q_I}}$ is also the inverting quality factor of the LC resonance. The time when V_P reaches to $\hat{V}_P$, x equals $\hat{x}$ is T_3. The behavior of these time interval is discussed in detail as following.

(i) $t \in [T_1, T_2]$

During this time interval, the inductor resonate with the clamped capacitor of the piezoelectric patch and comparing with the one oscillating period of the SSHI, the interval of LC resonance is much shorter. As LC resonance, the full-bridge rectifier is connected and I_R and I_L can be represented as equation (8.24) shown. During the oscillating period, the relation between voltage V_p and voltage V_C can be expressed as equation (8.25). Substitute the initial condition into equation (8.25), and the voltage V_P at time T_1 and T_2 can be obtained as equation (50) shown.

$$\begin{cases} I_R = I_L - I_C \\ I_L = -C_0 \dfrac{dV_P}{dt} \end{cases} \tag{8.24}$$

$$(V_P - V_C)(\frac{T_{LC}}{2}) = \left(-\hat{V}_P + \hat{V}_C\right) \cdot e^{\frac{-\omega_{LC}}{2Q_I} \cdot \frac{\pi}{\omega_{LC}}} \left[\frac{1}{2Q_I} \sin\left(\omega_{LC} \cdot \frac{\pi}{\omega_{LC}} \right) + \cos\left(\omega_{LC} \cdot \frac{\pi}{\omega_{LC}} \right) \right]$$

$$\Rightarrow (V_P - V_C)(\frac{T_{LC}}{2}) = \left(\hat{V}_P - \hat{V}_C\right) \cdot e^{-\frac{\pi}{2Q_I}} = \left(\hat{V}_P - \hat{V}_C\right) \cdot q_{LC} \tag{8.25}$$

$$\begin{cases}(V_P - V_C)(0) = -\hat{V}_C \\ V_P(\frac{T_{LC}}{2}) = -\hat{V}_C + \left(\hat{V}_P - \hat{V}_C\right)\cdot q_{LC}\end{cases} \tag{8.26}$$

Considering integrating I_L during half resonant period, the result is shown in equation (8.27).

$$\begin{aligned}&\int_{T_1}^{T_2} I_L \cdot dt = \int_0^{\frac{T_{LC}}{2}} -C_0 \frac{dV_P}{dt}\cdot dt \\ &\Rightarrow \int_0^{\frac{T_{LC}}{2}} I_L \cdot dt = C_0\hat{V}_P\left(1+q_{LC}\right)\end{aligned} \tag{8.27}$$

(ii) $t \in [T_2, T_3]$

During this period LC resonance is off, so the full bridge rectifier is disconnected. The I_R and I_P can be represented as equation (8.28). By integrating I_P from T_2 to T_3, the relation between $\hat{V}_P$ and $\hat{V}_C$ can be obtained as equation (8.29) shown.

$$\begin{cases}I_R = -I_C \\ I_P = I_L = 0\end{cases} \tag{8.28}$$

$$\begin{aligned}&\int_{T_2}^{T_3} I_P \cdot dt = \int_{T_2}^{T_3}\left(\alpha\dot{x} - C_0V_P\right)dt = 0 \\ &\Rightarrow \hat{V}_P = \frac{2\alpha\hat{x}}{C_0\left(1-q_{LC}\right)} - \frac{\left(1+q_{LC}\right)}{\left(1-q_{LC}\right)}\hat{V}_C\end{aligned} \tag{8.29}$$

(iii) $t \in [T_1, T_3]$

Considering the time period from T_1 to T_3 and integrating I_R, the result is shown in equation (8.30). The result shows that the current flow through I_R from T_1 to T_3 equals to the current during resonant period.

$$\begin{aligned}&\int_{T_1}^{T_3} I_R = \int_{T_1}^{T_2} I_R + \int_{T_2}^{T_3} I_R = \int_{T_1}^{T_2} \left(I_L - I_C\right) + \int_{T_2}^{T_3} \left(-I_C\right)\\ &\Rightarrow \int_{T_1}^{T_3} I_R = \int_{T_1}^{T_2} I_L\end{aligned} \tag{8.30}$$

According to the equation (8.30) and substituting the equation (8.27) into equation (8.30), the $\hat{V}_C$ can be obtained as equation (8.31) shown.

$$\begin{aligned}&\frac{\hat{V}_C}{R}\frac{\pi}{\omega_0} = C_0\left(\hat{V}_P - \hat{V}_C\right)\left(1+q_{LC}\right)\\ &\frac{\hat{V}_C}{R}\frac{\pi}{\omega_0} = C_0\left[\frac{2\alpha\hat{x}}{C_0\left(1-q_{LC}\right)} - \frac{\left(1+q_{LC}\right)}{\left(1-q_{LC}\right)}\hat{V}_C - \hat{V}_C\right]\left(1+q_{LC}\right)\\ &\Rightarrow \hat{V}_C = \frac{2\alpha R\left(1+q_{LC}\right)}{2R\omega_0 C_0\left(1+q_{LC}\right) + \pi\left(1-q_{LC}\right)}\omega_0\hat{x}\end{aligned} \tag{8.31}$$

[Reference]

1. Pogacian, S., A. Bot, and D. Zotoiu, "Acoustic Noise And Pneumatic Wave Vortices Energy Harvesting On Highways," in Processes in Isotopes and Molecules, Melville, Amer Inst Physics, pp. 77-80, 2012.
2. Sebald, G., D. Guyomar, and A. Agbossou, "On thermoelectric and pyroelectric energy harvesting," Smart Materials & Structures, vol. 18, no. 12, 2009.
3. A. Chandrakasan, et al., "Trends in low power digital signal processing," in Proceedings of the 1998 IEEE International Symposium on, vol.4, pp. 604-607, 1998.
4. Davis, W.R., et al., "A design environment for high-throughput low-power dedicated signal processing systems," IEEE J. Solid-State Circuits, vol. 37, pp. 420-431, Mar 2002.
5. Watkins, C., et al., "Low-grade-heat energy harvesting using superlattice thermoelectrics for applications in implantable medical devices and sensors," in ICT: 2005 24th International Conference on Thermoelectrics, New York, IEEE, 2005, pp. 250-252.
6. Sodano, H.A., et al., "Recharging batteries using energy harvested from thermal gradients," Journal of Intelligent Material Systems and Structures, vol. 18, pp. 3-10, Jan 2007.
7. W. Kuhlbrandt and D. N. Wang, "Three-dimensional structure of plant light-harvesting complex determined by electron crystallography," Nature, vol. 350, pp. 130-134, Mar 1991.
8. B. Oregan and M. Gratzel, "A low-cost, high-efficiency solar cell based on dye-sensitized colloidal TiO2 films," Nature, vol. 353, pp. 737-740, Oct 1991.
9. S. Priya, et al, "Piezoelectric Windmill: A Novel Solution to Remote Sensing," Japanese Journal of Applied Physics, vol. 44, pp. L104-L107, 2005.
10. T. Starner, "Human-powered wearable computing," IBM Systems Journal, vol. 35, pp. 618-629, 1996.
11. L. Mateu and F. Moll, "Optimum Piezoelectric Bending Beam Structures for Energy Harvesting using Shoe Inserts," Journal of Intelligent Material Systems and

Structures, vol. 16, pp. 835-845, Oct 2005.

12. P. D. Mitcheson, et al., "Energy harvesting from human and machine motion for wireless electronic devices," in Proceedings of the IEEE, vol. 96, pp. 1457-1486, Sep 2008.
13. G. W. Taylor, et al., "The Energy Harvesting Eel: a small subsurface ocean/river power generator," IEEE J. Ocean. Eng, vol. 26, pp. 539-547, Apr 2001.
14. M. Gratzel, "Solar energy conversion by dye-sensitized photovoltaic cells," Inorganic Chemistry, vol. 44, pp. 6841-6851, Oct 2005.
15. N. M. White, P. Glynne-Jones, and S. P. Beeby, "A novel thick-film piezoelectric micro-generator," Smart Materials & Structures, vol. 10, pp. 850-852, Aug 2001.
16. H.-S. Yoon, G. Washington, and A. Danak, "Modeling, Optimization, and Design of Efficient Initially Curved Piezoceramic Unimorphs for Energy Harvesting Applications," Journal of Intelligent Material Systems and Structures, vol. 16, pp. 877-888, Oct 2005.
17. K. Mossi, et al., "Harvesting Energy Using a Thin Unimorph Prestressed Bender: Geometrical Effects," Journal of Intelligent Material Systems and Structures, vol. 16, pp. 249-261, Mar 2005.
18. M. Duffy, D. Carroll, and ieee, "Electromagnetic generators for power harvesting," in Pesc 04: 2004 Ieee 35th Annual Power Electronics Specialists Conference, vols 1-6, New York, pp. 2075-2081, 2004.
19. P. Glynne-Jones, et al., "An electromagnetic, vibration-powered generator for intelligent sensor systems," Sensors and Actuators a-Physical, vol. 110, pp. 344-349, Feb 2004.
20. E. Sardini and M. Serpelloni, "An efficient electromagnetic power harvesting device for low-frequency applications," Sensors and Actuators a-Physical, vol. 172, pp. 475-482, Dec 2011.
21. G. K. Ottman, et al., "Adaptive piezoelectric energy harvesting circuit for wireless remote power supply," Power Electronics, IEEE Transactions on, vol. 17, pp. 669-676, 2002.
22. S. Roundy and P. K. Wright, "A piezoelectric vibration based generator for wireless electronics," Smart Materials & Structures, vol. 13, pp. 1131-1142, Oct 2004.

23. D. Guyomar, et al., "Synchronized switch harvesting applied to selfpowered smart systems: Piezoactive microgenerators for autonomous wireless transmitters," Sensors and Actuators a-Physical, vol. 138, pp. 151-160, 2007.
24. K. Yuse, et al, "Self-powered wireless health monitoring supplied by synchronized switch harvesting (SSH) method," Journal of Intelligent Material Systems and Structures, vol. 19, pp. 387-394, 2008.
25. M. Ferrari, et al., "An autonomous battery-less sensor module powered by piezoelectric energy harvesting with RF transmission of multiple measurement signals," Smart Materials & Structures, vol. 18, Aug 2009.
26. S. Roundy, P. K. Wright, and J. Rabaey, "A study of low level vibrations as a power source for wireless sensor nodes," Computer Communications, vol. 26, pp. 1131-1144, 2003.
27. J. Paradiso and M. Feldmeier, "A Compact, Wireless, Self-Powered Pushbutton Controller Ubicomp 2001: Ubiquitous Computing." Springer Berlin/Heidelberg, 2001, pp. 299-304.
28. M. Umeda, K. Nakamura, and S. Ueha, "Energy storage characteristics of a piezo-generator using impact induced vibration," Japanese Journal of Applied Physics Part 1-Regular Papers Short Notes & Review Papers, vol. 36, pp. 3146-3151, 1997.
29. G. K. Ottman, H. F. Hofmann, and G. A. Lesieutre, "Optimized piezoelectric energy harvesting circuit using step-down converter in discontinuous conduction mode," IEEE Trans. Power Electron, vol. 18, pp. 696-703, 2003.
30. SODANO, et al., "A review of power harvesting from vibration using piezoelectric materials" vol. 36. Thousands Oaks, CA, ETATS-UNIS: Sage, 2004.
31. S. Roundy, "On the effectiveness of vibration-based energy harvesting," Journal of Intelligent Material Systems and Structures, vol. 16, pp. 809-823, Oct 2005.
32. E. Lefeuvre, et al., "Piezoelectric energy harvesting device optimization by synchronous electric charge extraction," Journal of Intelligent Material Systems and Structures, vol. 16, pp. 865-876, Oct 2005.
33. D. Guyomar, et al., "Toward energy harvesting using active materials and conversion improvement by nonlinear processing," IEEE Trans. Ultrason.

Ferroelectr. Freq. Control, vol. 52, pp. 584-595, 2005.

34. E. Lefeuvre, et al., "A comparison between several approaches of piezoelectric energy harvesting," Journal De Physique Iv, vol. 128, pp. 177-186, 2005.
35. M. Lallart, et al, "Double synchronized switch harvesting (DSSH): A new energy harvesting scheme for efficient energy extraction," IEEE Trans. Ultrason. Ferroelectr. Freq. Control, vol. 55, pp. 2119-2130, 2008.
36. Y. Y. Chen, et al., "A self-powered switching circuit for piezoelectric energy harvesting with velocity control," European Physical Journal-Applied Physics, vol. 57, Feb 2012.
37. T. H. Ng and W. H. Liao, "Sensitivity analysis and energy harvesting for a self-powered piezoelectric sensor," Journal of Intelligent Material Systems and Structures, vol. 16, pp. 785-797, Oct 2005.
38. S. Kim, W. W. Clark, and Q.-M. Wang, "Piezoelectric Energy Harvesting with a Clamped Circular Plate: Analysis," Journal of Intelligent Material Systems and Structures, vol. 16, pp. 847-854, Oct 2005.
39. S. Kim, W. W. Clark, and Q.-M. Wang, "Piezoelectric Energy Harvesting with a Clamped Circular Plate: Experimental Study," Journal of Intelligent Material Systems and Structures, vol. 16, pp. 855-863, Oct 2005.
40. M. Ericka, et al., "Energy harvesting from vibration using a piezoelectric membrane," Journal De Physique Iv, vol. 128, pp. 187-193, Sep 2005.
41. M. Goldfarb and L. D. Jones, "On the efficiency of electric power generation with piezoelectric ceramic," Journal of Dynamic Systems Measurement and Control-Transactions of the Asme, vol. 121, pp. 566-571, Sep 1999.
42. M. Umeda, K. Nakamura, and S. Ueha, "Analysis of the transformation of mechanical impact energy to electric energy using piezoelectric vibrator," Japanese Journal of Applied Physics Part 1-Regular Papers Short Notes & Review Papers, vol. 35, pp. 3267-3273, 1996.
43. C. D. Richards, et al., "Efficiency of energy conversion for devices containing a piezoelectric component," Journal of Micromechanics and Microengineering, vol. 14, pp. 717-721, May 2004.
44. G. A. Lesieutre, G. K. Ottman, and H. F. Hofmann, "Damping as a result of

piezoelectric energy harvesting," Journal of Sound and Vibration, vol. 269, pp. 991-1001, 2004.

45. E. Lefeuvre, A. Badel, C. Richard, and D. Guyomar, "High performance piezoelectric vibration energy reclamation," Smart Structures and Materials 2004: Smart Structures and Integrated Systems, vol. 5390, pp. 379-387, 2004.
46. A. Badel, et al., "Piezoelectric energy harvesting using a synchronized switch technique," Journal of Intelligent Material Systems and Structures, vol. 17, pp. 831-839, 2006.
47. E. Minazara, et al., "Piezoelectric diaphragm for vibration energy harvesting," Ultrasonics, vol. 44, pp. E699-E703, Dec 2006.
48. Y. W. Yang and L. H. Tang, "Equivalent Circuit Modeling of Piezoelectric Energy Harvesters," Journal of Intelligent Material Systems and Structures, vol. 20, pp. 2223-2235, Dec 2009.
49. Y. C. Shu, I. C. Lien, and W. J. Wu, "An improved analysis of the SSHI interface in piezoelectric energy harvesting," Smart Materials & Structures, vol. 16, pp. 2253-2264, Dec 2007.
50. N. S. Shenck and J. A. Paradiso, "Energy scavenging with shoe-mounted piezoelectrics," Micro, IEEE, vol. 21, pp. 30-42, 2001.
51. N. G. Elvin, A. A. Elvin, and M. Spector, "A self-powered mechanical strain energy sensor," Smart Materials and Structures, vol. 10, p. 293, 2001.
52. N. Elvin, A. Elvin, and D. H. Choi, "A self-powered damage detection sensor," Journal of Strain Analysis for Engineering Design, vol. 38, pp. 115-124, Mar 2003.
53. M. Lallart and D. Guyomar, "An optimized self-powered switching circuit for non-linear energy harvesting with low voltage output," Smart Materials & Structures, vol. 17, 2008.
54. L. Junrui and L. Wei-Hsin, "Improved Design and Analysis of Self-Powered Synchronized Switch Interface Circuit for Piezoelectric Energy Harvesting Systems," IEEE Trans. Ind.l Electron, on, vol. 59, pp. 1950-1960, 2012.
55. E. S. Leland and P. K. Wright, "Resonance tuning of piezoelectric vibration energy scavenging generators using compressive axial preload," Smart Materials & Structures, vol. 15, pp. 1413-1420, Oct 2006.

56. D. Zhu, et al., "Closed loop frequency tuning of a vibration-based micro-generator," in PowerMEMS 2008+ microEMS2008, 2008.
57. J.-T. Lin and et al., "The magnetic coupling of a piezoelectric cantilever for enhanced energy harvesting efficiency," Smart Materials and Structures, vol. 19, p. 045012, Apr 2010.
58. A. Erturk, J. Hoffmann, and D. J. Inman, "A piezomagnetoelastic structure for broadband vibration energy harvesting," Applied Physics Letters, vol. 94, Jun 2009.
59. B. Ando, et al., "Nonlinear mechanism in MEMS devices for energy harvesting applications," Journal of Micromechanics and Microengineering, vol. 20, Dec 2010.
60. B. P. Mann and N. D. Sims, "Energy harvesting from the nonlinear oscillations of magnetic levitation," Journal of Sound and Vibration, vol. 319, pp. 515-530, 2009.
61. J. Kymissis, et al., "Parasitic power harvesting in shoes," in Wearable Computers, 1998. Digest of Papers. Second International Symposium on, pp. 132-139, 1998.
62. N. W. Hagood and A. von Flotow, "Damping of structural vibrations with piezoelectric materials and passive electrical networks," Journal of Sound and Vibration, vol. 146, pp. 243-268, 1991.
63. C. D. Johnson, "Design of Passive Damping Systems," Journal of Mechanical Design, vol. 117, pp. 171-176, 1995.
64. S. O. R. Moheimani, "A survey of recent innovations in vibration damping and control using shunted piezoelectric transducers," IEEE Trans. Control Syst. Technol. vol. 11, pp. 482-494, 2003.
65. S. Elliott, I. Stothers, and P. Nelson, "A multiple error LMS algorithm and its application to the active control of sound and vibration," IEEE Trans. Acoust., Speech, Signal Process, vol. 35, pp. 1423-1434, 1987.
66. C. R. Fuller, "Active control of sound transmission/radiation from elastic plates by vibration inputs: I. Analysis," Journal of Sound and Vibration, vol. 136, pp. 1-15, Jan 1990.
67. C. Richard, et al., "Semi-passive damping using continuous switching of a piezoelectric device," Proc. SPIE:Smart Structures and Materials 1999: Passive Damping and Isolation vol. 3672, pp. 104-111, 1999.

68. C. Richard, et al., "Enhanced semi-passive damping using continuous switching of a piezoelectric device on an inductor," Proc. SPIE:Smart Structures and Materials 2000: Damping and Isolation, vol. 3989, pp. 288-299, 2000.
69. W. W. Clark, "Vibration Control with State-Switched Piezoelectric Materials," Journal of Intelligent Material Systems and Structures, vol. 11, pp. 263-271, Apr, 2000.
70. H. Ji, et al., "Multi-modal vibration control using a synchronized switch based on a displacement switching threshold," Smart Materials and Structures, vol. 18, p. 035016, 2009.
71. E. Lefeuvre, et al., "Semi-passive piezoelectric structural damping by synchronized switching on voltage sources," Journal of Intelligent Material Systems and Structures, vol. 17, pp. 653-660, 2006.
72. L. Hong, et al., "Semi-active Vibration Control of a Composite Beam using an Adaptive SSDV Approach," Journal of Intelligent Material Systems and Structures, Sep 2008.
73. A. Badel, et al., "Piezoelectric vibration control by synchronized switching on adaptive voltage sources: Towards wideband semi-active damping," Journal of the Acoustical Society of America, vol. 119, pp. 2815-2825, 2006.
74. "IEEE Standard on Piezoelectricity," ANSI/IEEE Std 176-1987, 1988.
75. D. Guyomar and M. Lallart, "Energy conversion improvement in ferroelectrics: application to energy harvesting and self-powered systems," in Ultrasonics Symposium (IUS), 2009 IEEE International, pp. 1-10, 2009.
76. E. Lefeuvre, et al., "High performance piezoelectric vibration energy reclamation," Smart Structures and Materials 2004: Smart Structures and Integrated Systems, vol. 5390, pp. 379-387, 2004.
77. E. Lefeuvre, et al., "A comparison between several vibration-powered piezoelectric generators for standalone systems," Sensors and Actuators a-Physical, vol. 126, pp. 405-416, 2006.
78. J. Liang and W.-H. Liao, "Energy flow in piezoelectric energy harvesting systems," Smart Materials and Structures, vol. 20, p. 015005, 2011.
79. H. A. Sodano, D. J. Inman, and G. Park, "Comparison of piezoelectric energy

harvesting devices for recharging batteries," Journal of Intelligent Material Systems and Structures, vol. 16, pp. 799-807, Oct 2005.

80. C. O. Mathuna, et al., "Energy scavenging for long-term deployable wireless sensor networks," Talanta, vol. 75, pp. 613-623, May 2008.
81. M. Lallart, et al., "Synchronized switch harvesting applied to self-powered smart systems: Piezoactive microgenerators for autonomous wireless receivers," Sensors and Actuators a-Physical, vol. 147, pp. 263-272, 2008.
82. J. A. Paradiso and T. Starner, "Energy scavenging for mobile and wireless electronics," Pervasive Computing, IEEE, vol. 4, pp. 18-27, 2005.
83. S. Meninger, et al., "Vibration-to-electric energy conversion," IEEE Trans. Very Large Scale Integr. (VLSI) Syst., vol. 9, pp. 64-76, 2001.
84. R. Amirtharajah and A. P. Chandrakasan, "Self-powered signal processing using vibration-based power generation," Solid-State Circuits, IEEE Journal of, vol. 33, pp. 687-695, 1998.
85. A. Badel, et al., "Efficiency enhancement of a piezoelectric energy harvesting device in pulsed operation by synchronous charge inversion," Journal of Intelligent Material Systems and Structures, vol. 16, pp. 889-901, Oct 2005.
86. S. C. Stanton, C. C. McGehee, and B. P. Mann, "Nonlinear dynamics for broadband energy harvesting: Investigation of a bistable piezoelectric inertial generator," Physica D: Nonlinear Phenomena, vol. 239, pp. 640-653, 2010.
87. A. Nayfeh, Mook, D., "Nonlinear Oscillations." New York: Wiley, 1979.
88. J. M. T. Thompson, "Chaotic Phenomena Triggering the Escape from a Potential Well," Proceedings of the Royal Society of London Series a-Mathematical Physical and Engineering Sciences, vol. 421, pp. 195-225, Feb, 1989.
89. H. B. Stewart, et al., "Optimal escape from potential wells-patterns of regular and chaotic bifurcation," Physica D, vol. 85, pp. 259-295, Jul, 1995.
90. E. Garcia, J. Dosch, and D. J. Inman, "The Application of Smart Structures to the Vibration Suppression Problem," Journal of Intelligent Material Systems and Structures, vol. 3, pp. 659-667, Oct, 1992.
91. V. Giurgiutiu, "Review of smart-materials actuation solutions for aeroelastic and vibration control," Journal of Intelligent Material Systems and Structures, vol. 11,

pp. 525-544, Jul 2000.

92. M. J. Konak, et al., "Self-powered discrete time piezoelectric vibration damper," in Proc. SPIE ,Smart Materials, Structures, and Integrated Systems, vol. 3241, pp. 270-279, 1997.
93. M. Lallart, et al., "Self-powered circuit for broadband, multimodal piezoelectric vibration control," Sensors and Actuators a-Physical, vol. 143, pp. 377-382, Feb 2008.
94. H. Shen, et al., "A low-power circuit for piezoelectric vibration control by synchronized switching on voltage sources," Sensors and Actuators a-Physical, vol. 161, pp. 245-255, Jun 2010.
95. D. R. C. D. A. Berlincourt, and H. Jaffe, “Piezoelectric and piezomagnetic materials and their function in transducers,” in Physical Acoustics, W. P. Mason, Ed. New York: , Academic Press: Physical Acoustics, 1964.
96. W. P. Mason, "Piezoelectric Crystals and Their Application to Ultrason" New York, Van Nostrand, 1950.